BNL 47055
Informal Report

GAS PROPORTIONAL DETECTORS WITH INTERPOLATING CATHODE PAD READOUT FOR HIGH TRACK MULTIPLICITIES

Bo Yu

December 1991

Instrumentation Division
Brookhaven National Laboratory
Associated Universities, Inc.
Upton, New York 11973

Under Contract No. DE-AC02-76CH00016 with the
UNITED STATES DEPARTMENT OF ENERGY

DISCLAIMER

BNL--47055

DE92 007189

GAS PROPORTIONAL DETECTORS WITH INTERPOLATING CATHODE PAD READOUT FOR HIGH TRACK MULTIPLICITIES

by

Bo Yu

B.S., Beijing University, 1985

M.S., University of Pittsburgh, 1986

Submitted to the Graduate Faculty of
Arts and Sciences in partial fulfillment
of the requirements for the degree of
Doctor of Philosophy

University of Pittsburgh

1991

Dissertation Advisor:

Wilfred E. Cleland

Committee Members:

Veljko Radeka

Joel Falk

Jürg X. Saladin

Philip Stehle

Julia A. Thompson

Acknowledgements

It is a great pleasure to thank the people who have made this work possible and enjoyable.

Most of all, I'd like to express my gratitude to my advisors, Dr. W.E. Cleland and Dr. V. Radeka, for their efforts in arranging my working at Brookhaven National Laboratory. This opportunity has provided me sources of inspiration and experience. I'd like to thank them for their advice and critism during the completion of this thesis. Dr. Radeka has always given invaluable theoretical guidance throughout this work.

Special thanks to Dr. G.C. Smith, who, with his knowledge and expertise, has provided valuable training and guidance. He is always available for discussions which are invariably productive and fascinating.

Numerous discussions with Dr. D. Stephani, Dr. J. Fischer, Dr. D. Lissauer, Dr. T.W. Ludlam, Dr. D. Mackowiecki, Dr. R. Debbe and Dr. E. O'Brien are greatly appreciated.

Thanks to many staff members of BNL Instrumentation Division, especially E.Von Achen, for their assistance during the course of this work.

Thanks to members of my thesis committee, especially Dr. J.A. Thompson, for their suggestions on this thesis.

Thanks to my wife Siyu Liu for her love and support.

Financial support was provided by University of Pittsburgh and Brookhaven National Laboratory.

This manuscript is typeset in TEX, primarily using the TEXsis macros developed by Dr. E. Myers and Dr. F.E Paige.

Abstract

New techniques for position encoding in very high rate particle and photon detectors will be required in experiments planned for future particle accelerators such as the Superconducting Super Collider and new, high intensity, synchrotron sources.

Studies of two interpolating cathode 'pad' readout systems are described in this thesis. They are well suited for high multiplicity, two dimensional unambiguous position sensitive detection of minimum ionizing particles and heavy ions as well as detection of x-rays at high counting rates. One of the readout systems uses subdivided rows of pads interconnected by resistive strips as the cathode of a multiwire proportional chamber (MWPC). A position resolution of less than 100 μm rms, for 5.4 keV x-rays, and differential non-linearity of 12% have been achieved. Low mass ($\sim$0.6% of a radiation length) detector construction techniques have been developed. The second readout system uses rows of chevron shaped cathode pads to perform geometrical charge division. Position resolution (FWHM) of about 1% of the readout spacing and differential non-linearity of 10% for 5.4 keV x-rays have been achieved.

A review of other interpolating methods is included. Low mass cathode construction techniques are described. In conclusion, applications and future developments are discussed.

Table of Contents

List of Tables

List of Figures

Chapter 1.
Introduction

1.1. Background

Since the introduction of the Multiwire Proportional Chamber (MWPC) in 1968, it has been widely used in the detection of energetic charged particles as well as energetic photons. A typical structure of an MWPC is illustrated in Fig. 1.1.1. Because of the simplicity of such devices, the ease of construction, the capability to realize a large active area, and good position resolution, it soon became one of the most popular tracking devices in the field of experimental high energy physics.

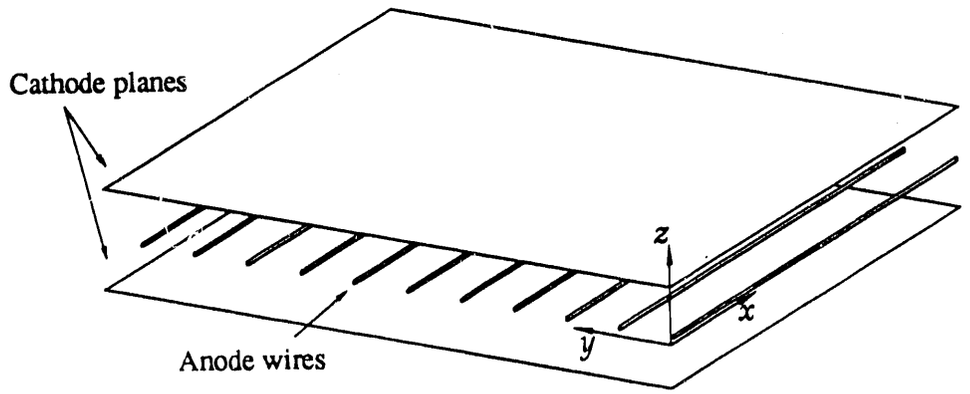

Figure 1.1.1: Structure of a typical MWPC

A single plane of MWPC as shown in Fig. 1.1.1 can give position information of an incident particle only in one direction (perpendicular to the anode wires). A second plane of MWPC (with anode wires running in the direction orthogonal to that of the first one) is needed to give a coordinate in the second direction. However, for events with more than one simultaneous incident particle, it cannot provide unambiguous coordinates for all tracks. As illustrated in Fig. 1.1.2, "ghosts"—false particle positions, are created along with the real particle positions. The only solution to this problem is to add additional planes of MWPCs with different anode wire orientations

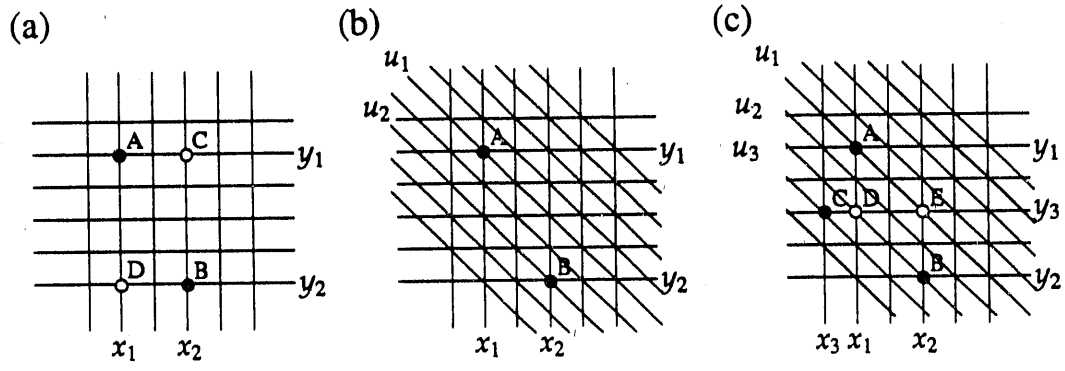

Figure 1.1.2: Ambiguity in a projective geometry. Solid circles represent real hits, hollow circles represent "ghosts." (a) Two layers of MWPC cannot resolve two hits; (b) with a third layer, two hits can be resolved; (c) three layers of MWPC cannot resolve three hits.

to resolve the ambiguities of the system. According to a study on spark chambers (which is equally applicable to MWPCs) [1], for a detector with only two orthogonal anode wire planes, a quality factor Q, which quantifies the ambiguities, is defined:

$$\begin{aligned} Q &= \frac{\text{number of candidate points}}{\text{number of incident particles}} \\ &= \left(N^2/n\right)\left(1-e^{-n/N}\right)^2 \\ &\approx n \qquad \text{for} \quad n/N \ll 1, \end{aligned} \tag{1.1.1}$$

where N is the number of wires in an MWPC plane; n is the number of incident particles. Adding two more MWPC planes to the system improves the quality factor Q to:

$$Q = 1 + \frac{\left[N\left(1-e^{-n/N}\right)^2 - n/N\right]^2}{n}. \tag{1.1.2}$$

This expression is plotted in Fig. 1.1.3.

For higher multiplicities and particle densities, more planes are needed and each plane needs to have a large number of wires. The pattern recognition quickly becomes prohibitively complicated. For a given chamber, the pattern recognition fails rapidly with the increase of track multiplicity.

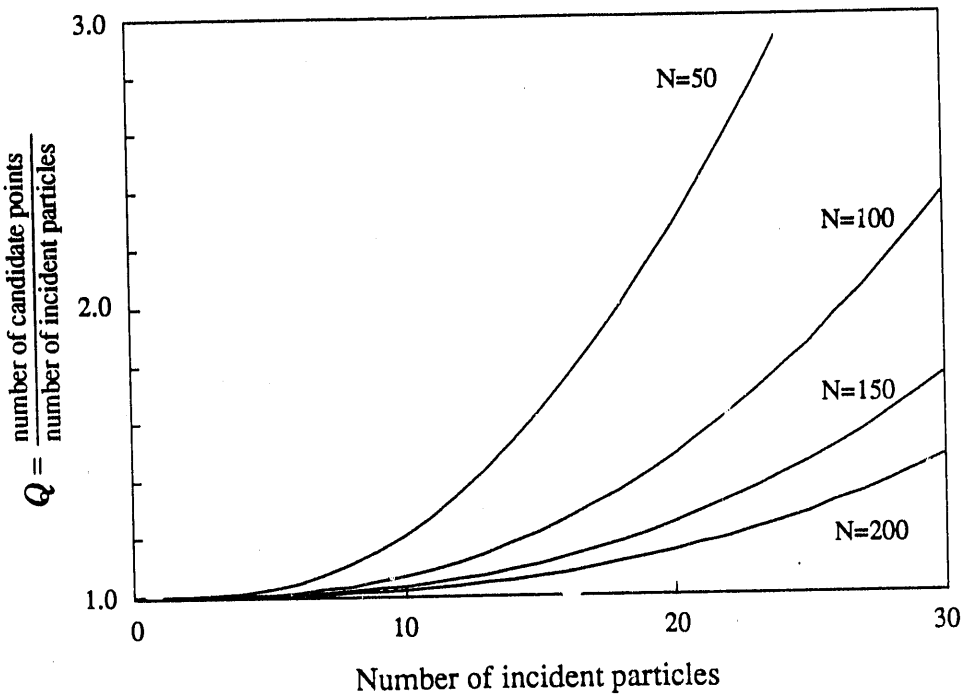

Figure 1.1.3: Quality factor of a multiwire spark chamber system consisting of 4 planes of wires. N is the number of sense wires in each plane.

In high energy physics, for example, experiments at heavy ion colliders, such as the Relativistic Heavy Ion Collider (RHIC) and hadron colliders, such as the Superconducting Super Collider (SSC) will require accurate tracking detectors capable of resolving track multiplicities in the range of 10^3/steradian.

Another important requirement which is common to position sensitive detector applications in many fields, is a high counting rate capability. In synchrotron radiation experiments, the next generation of synchrotron sources will increase the maximum photon flux beyond the capabilities of many present position encoding methods.

It is obvious that a new type of detector is needed to resolve high multiplicity events in today's large high energy experiments, one that provides unambiguous two-dimensional information with good efficiency. This thesis will focus on two types of detector developed at Brookhaven National Laboratory.

1.2. Scope of This Thesis

This thesis describes the R&D work on two types of interpolating cathode pad readout system used in MWPCs. One of the readout systems uses subdivided rows of resistively coupled cathode pads underneath each anode wire to perform charge division. A position resolution of less than 100 μm rms, for 5.4 keV x-rays, and differential non-linearity of 12% have been achieved. The second readout system uses rows of chevron shaped cathode pads to perform geometrical charge division. Position resolution (FWHM) of about 1% of the readout spacing and differential non-linearity of 10% for 5.4 keV x-rays have been achieved. All the work described was performed at Brookhaven National Laboratory between 1986 and 1991.

The thesis is divided into seven chapters. A review of the principles of operation of the MWPC detector, and previous pioneering works related to the present research are given in Chapters 2 and 3. Experimental results for both detector systems are described in Chapters 4 and 5. Construction procedures are given in Chapter 6. Conclusions and future developments of these systems are discussed in Chapter 7.

Some of the results in Chapter 4 were published in Refs. [2–4]. Some results in Chapter 5 were published in Ref. [5].

In some of the computer simulations described in the text, the chamber geometries are based upon a conceptual design of a proposed tracking chamber in an SSC experiment. However, many results are shown in a normalized manner in order to be used for general purposes.

The coordinate system used throughout this thesis is defined as follows (see Fig. 1.1.1):

- x coordinate is the direction parallel to the anode wires.
- y coordinate is the direction perpendicular to the anode wires but within the wire plane.
- z coordinate is the direction perpendicular to the anode wire plane.

Chapter 2.
Principles of Operation in an MWPC

This chapter describes some of the major physical processes inside an MWPC. Some parameters characterizing a detector's performance are also discussed.

2.1. Energy Loss Mechanism

When an energetic charged particle passes through a gas, it undergoes a series of inelastic Coulomb collisions with the electrons of the gas molecules. As a result, the particle loses its energy by excitation and ionization of the gas molecules, leaving a trail of electron-ion pairs along its trajectory. This is the signature that an MWPC detects.

The theory for ionization loss is given by the Bethe–Bloch formula:

$$\frac{dE}{dx} = -2K\frac{Z}{A}\frac{\rho}{\beta^2}\left[\ln\left(\frac{2m_e v^2}{I\,(1-\beta^2)}\right) - \beta^2\right], \qquad K = \frac{2\pi N_0 z^2 e^4}{m_e c^2} \tag{2.1.1}$$

where m_e is the electron mass, $\beta = v/c$, z and v are the charge and velocity of the particle, N_0 is Avogadro's number, Z and A are the atomic number and mass number of the atoms (or molecules) of the medium, x is the path length in the medium, and I is an effective ionization potential averaged over all electrons ($I \approx 10Z\,\mathrm{eV}$). Eq. (2.1.1) shows that dE/dx is independent of the particle mass M. It varies as $1/v^2$ at non-relativistic velocities, reaches a minimum for $E \simeq 3Mc^2$, increases logarithmically with $\gamma = E/Mc^2 = (1-\beta^2)^{-1/2}$ (called relativistic rise). Generally, $(dE/dx)_{\min} \simeq$1–1.5 $\mathrm{MeVcm^2/g}$ for most media.

Fig. 2.1.1 shows the energy loss in Argon for different particles, and the energy loss of protons in various gases [6].

A classical description of the energy loss distribution in a thin absorber (in which the energy loss is negligible compared with the total energy of the particle) due to Landau, is written as:

$$f(\lambda) = \frac{1}{2\pi}e^{-\frac{1}{2}(\lambda+e^{-\lambda})}, \tag{2.1.2}$$

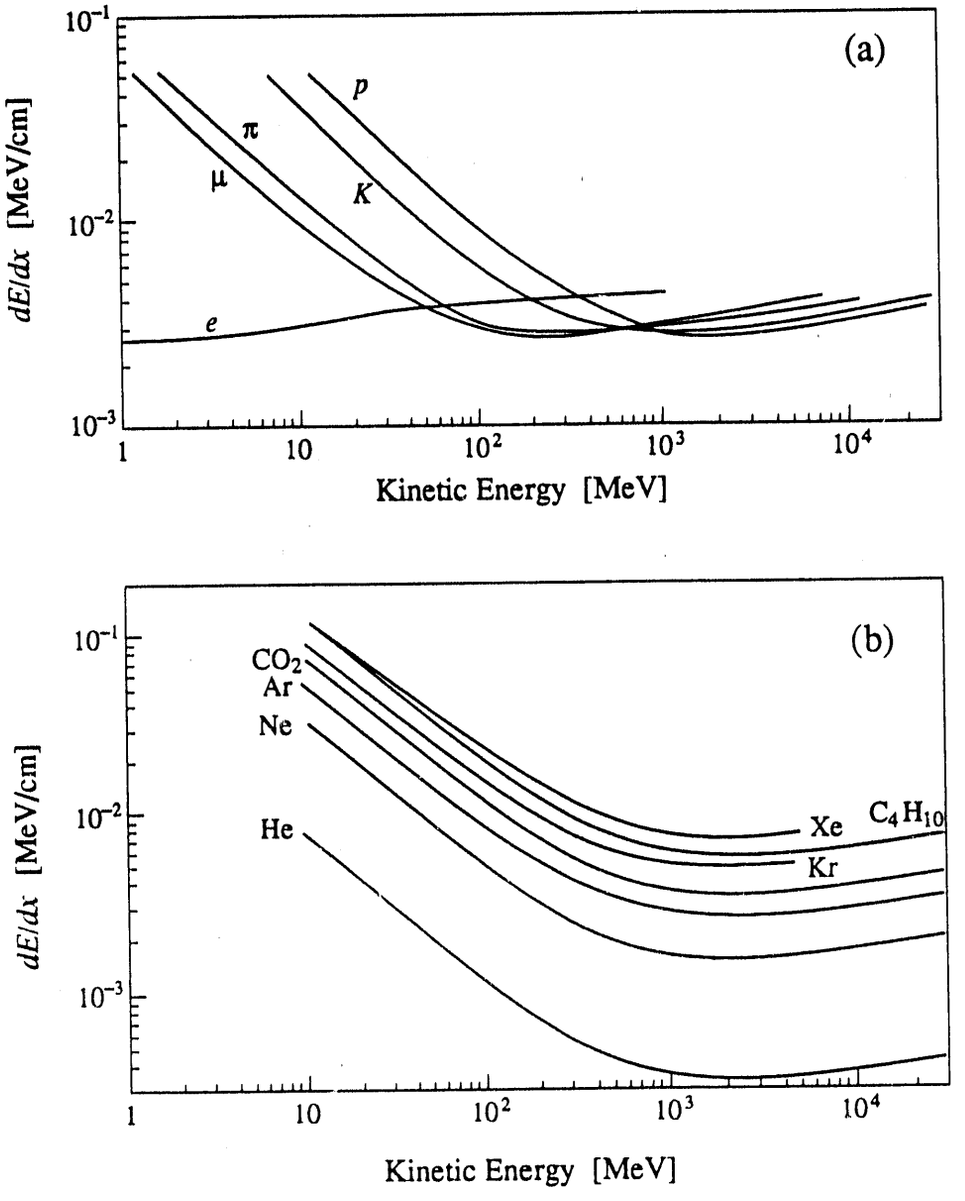

Figure 2.1.1: (a) Energy loss of various particles in argon (b) Energy loss of protons in various gases [6].

where λ represents the normalized deviation from the most probable energy loss $\Delta E_{\rm MP}$:

$$\lambda = \frac{\Delta E - \Delta E_{\rm MP}}{\xi}, \qquad \xi = K\frac{Z}{A}\frac{\rho x}{\beta^2}. \tag{2.1.3}$$

The energy loss distribution calculated from the above expression is narrower than the experimental results from an MWPC. Other models which include corrections from atomic shell structures are given in Refs. [7–8].

The energy range of photons of interest in this work is a few keV. Photons interact with detector gas mainly by the photoelectric effect. It is a single localized event. A simplified process can be described as the following:

The absorption of an x-ray photon of energy E_γ by a gas molecule with a shell energy of E_i ($E_i \leq E_\gamma$) results in the emission of a photoelectron with energy $E_e = E_\gamma - E_i$. The excited molecule (ion) with a vacancy in its inner shell returns to its ground state mainly through either of the following processes:

i. Fluorescence: an outer shell electron with binding energy E_j fills the inner shell vacancy, emitting a photon of energy $E_i - E_j$.

ii. Auger effect: an internal rearrangement involving several outer shell electrons, results in the filling of the inner shell vacancy by an outer shell electron (with binding energy E_j) and emission of an outer shell electron with energy $E_i - 2E_j$.

The fluorescent photon has a relatively long range and it can escape from the detector gas volume, resulting in a deficit in the deposited energy (an escape peak in the energy spectrum). Fig. 2.1.2 shows the energy spectrum obtained from a detector with 5.9 keV x-rays and argon gas mixture.

2.2. Ionization of Gas, Anode Avalanche

The electric field of a typical MWPC geometry used in this work is shown in Fig. 2.2.1 (generated using the program GARFIELD [9] from the CERN Program Library). The ionization caused by the incident charged particles or photons results in a collection of electrons and positive ions. Under the influence of the electric field in the chamber, the electrons drift toward the anode wire and positive ions toward the cathodes. It is the electrons drifting toward the anode wire which are of most

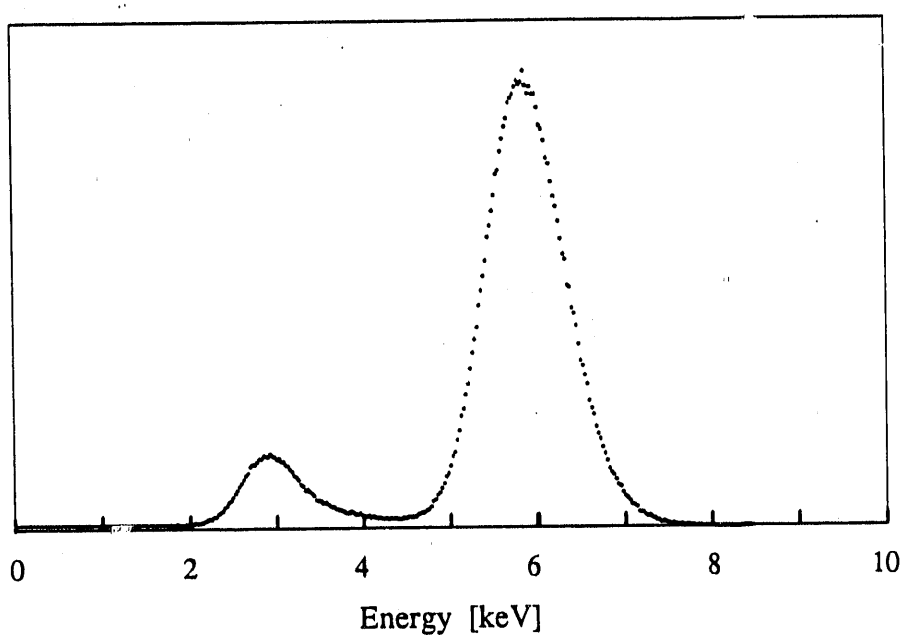

Figure 2.1.2: Energy spectrum of 5.9 keV x-rays in an argon filled MWPC.

importance in the MWPC operation. The positive ions are about a factor of 1000 slower in drift velocity than the electrons.

With the increase of the electric field near the anode wire, an electron gains more and more energy between collisions. When its kinetic energy is greater than the ionization potential of the gas molecules, it can ionize a gas molecule upon collision and create an electron-ion pair. Subsequently, the newly created electrons, together with the original electrons, will gain enough energy to ionize other neutral gas molecules. An avalanche of ionization is therefore formed. The process of ionization by collision is the basis of the avalanche multiplication in a proportional chamber. The typical proportional chamber has a cylindrical electric field near the anode wire. The avalanche takes place within several wire diameters above the anode wire surface.

The slow moving positive ions created by the avalanche process drift away from the anode wire. Compared with the speed of the drifting electrons, they can be considered stationary. For avalanches which create a large number of electron-ion pairs, the presence of the positive ions surrounding the anode wire can form a "shell" which effectively reduces the electric field strength inside, resulting in a reduced gas amplification factor. This is commonly called the space charge effect. It occurs most

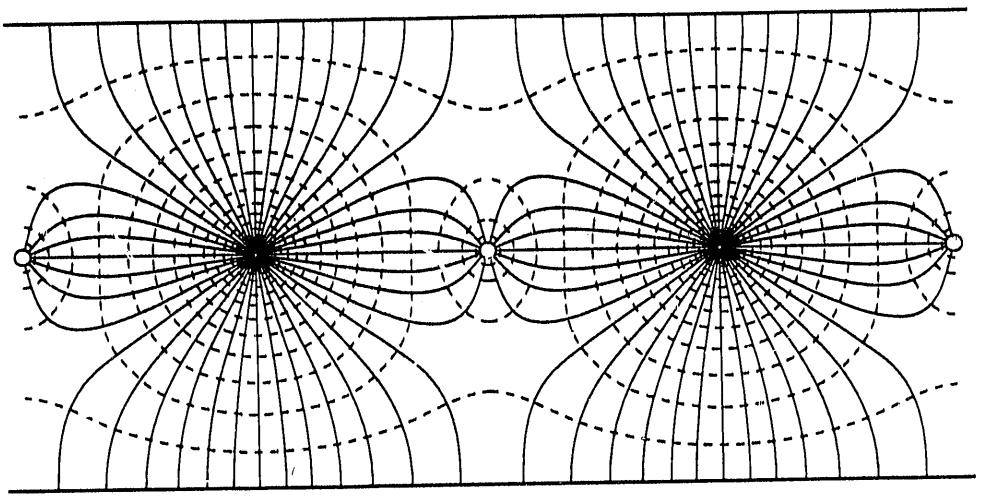

Figure 2.2.1: Electric field lines (solid line) and equi-potential lines (dashed line) in a chamber geometry used in this work.

likely in chambers with thin anode wires, large gas gain, and at high counting rates. In the detectors described in Chapter 4, this effect is deliberately used to reduce the dynamic range required for the readout electronics.

2.3. Induced Charge on Electrodes

The movement of the electrons and positive ions from an avalanche induces charge on the surrounding electrodes. The signal detected by the readout electronics connected to either anode or cathode is due to this induced charge. An understanding of the time development and spatial distribution of the induced charge is crucial to the design and application of the readout electronics and electrode structure.

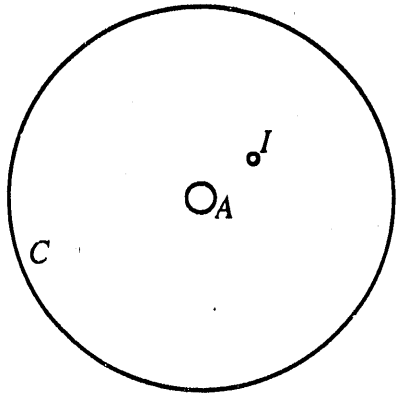

Figure 2.3.1: A simple electrode configuration

2.3.1 Green's Theorem of Reciprocity

Green's theorem of reciprocity states that if charges Q_1, Q_2, ... , Q_n on the conductors of a system give rise to potentials V_1, V_2, ..., V_n and if charges Q'_1, Q'_2, ... , Q'_n on the conductors of a system give rise to potentials V'_1, V'_2, ..., V'_n, then:

$$\sum_{i=1}^{n} Q_i V'_i = \sum_{i=1}^{n} Q'_i V_i. \tag{2.3.1}$$

We consider a simple system with three conductors: A, C and I as shown in Fig. 2.3.1. According to Eq. (2.3.1):

$$Q_A V'_A + Q_C V'_C + Q_I V'_I = Q'_A V_A + Q'_C V_C + Q'_I V_I$$

Let the initial state be: $Q_I = 0$, $V_A = 1$ and $V_C = 0$, and let the final state be: $Q'_I = q_0$, $V'_A = 1$ and $V'_C = 0$. Then we have:

$$Q_A \cdot 1 + Q_C \cdot 0 + 0 \cdot V'_I = Q'_A \cdot 1 + Q'_C \cdot 0 + q_0 \cdot V_I$$

which yields:

$$Q'_A - Q_A = -q_0 V_I. \tag{2.3.2}$$

$Q'_A - Q_A$ is the induced charge on conductor A due to the presence of charge q_0 on conductor I, and V_I is the potential at the location of conductor I for the initial state.

Now let conductor A be the anode, C be the cathode and I be the positive ion cloud created from the avalanche. Then the charge induced on the anode wires is simply $-q_0 V_I$, in which q_0 is the charge of the ion cloud and V_I is the potential at the ion location with the anode raised to *unit* potential and the cathode at *zero* potential. Similarly, the induced charge on the cathode C can be found to be $q_0 V_I$.

2.3.2 Time Development of Induced Charge

Now we consider a cylindrical wire chamber geometry. Let r_a, r_c be the radii of the anode and cathode respectively. Let V_a be the anode voltage and let $V_c = 0$. The electric field at a distance r from the center of the anode $E(r)$ can be described as:

$$E(r) = \frac{1}{\ln(r_c/r_a)} \frac{V_a}{r}, \tag{2.3.3}$$

and the potential $V(r)$ can be expressed as:

$$V(r) = V_a \left[1 - \frac{\ln(r/r_a)}{\ln(r_c/r_a)}\right]. \tag{2.3.4}$$

Assume the avalanche process creates two point charges: q_0 and $-q_0$, where q_0 is the charge of the positively charged ions and $-q_0$ is the charge due to the electrons. Because of the geometry of the chamber, most of the multiplication process occurs at r_0, which is very close to the anode wire (almost half of the total avalanche charge is created in the last mean free path above the anode surface). Assume that the positive ions move towards the cathode under the influence of the electric field, with a velocity defined as: $v(r) = \mu E(r)$, where μ is the positive ion mobility which is considered to be independent of E. Assume the electrons arrive at the anode wire surface after a very short time Δt because of the fast drift velocity and short distance of travel of the electrons.

The charge induced on the anode wire due to the positive ions is, according to Eq. (2.3.2): $Q_i = -q_0 V_i$, and similarly, the charge induced by the electrons on the anode is $Q_e = q_0 V_e$. Assume that the time Δt is short enough that we can consider the ions to be stationary during that period. Then the net induced charge on the

anode wire can be described by the following:

$$Q_A = \begin{cases} -q_0 V_1(r_0) + q_0 V_1(r_0) = 0 & t = 0 \\ -q_0 V_1(r_0) + q_0 \cdot 1 & t = \Delta t \\ -q_0 V_1(r) & t > \Delta t \\ -q_0 \cdot 0 = 0 & t \geq t_c \end{cases} \tag{2.3.5}$$

where t_c is the time when the positive ions arrive at the cathode surface, and $V_1 = 1 - \frac{\ln(r/r_a)}{\ln(r_c/r_a)}$ is the potential at the ion location with the anode raised to *unit* potential while the cathode is at zero potential.

In a MWPC, it is normally considered that the electrons are very close to the anode surface (most of them are within a few mean free paths of ionizing collision). For most applications, the induced charge due to the motion of electrons can be ignored (this results in less than 5% error in the total signal charge) [10]. However, the contribution of electrons to the anode signal cannot be ignored in cases where very fast readout electronics are used. Eq. (2.3.5) can then be rewritten in terms of the induced current:

$$i_A = \frac{dQ_A}{dt} = -q_0 \frac{dV_1(r)}{dr}\frac{dr}{dt} \tag{2.3.6}$$

while:

$$\frac{dV_1(r)}{dr} = -E_1(r) = -\frac{1}{r\ln(r_c/r_a)} \tag{2.3.7a}$$

$$\frac{dr}{dt} = v = \mu E(r) = \frac{\mu}{\ln(r_c/r_a)}\frac{V_a}{r}. \tag{2.3.7b}$$

From Eq. (2.3.7b) one obtains:

$$r dr = \frac{\mu V_a}{\ln(r_c/r_a)} dt. \tag{2.3.8}$$

integrate Eq. (2.3.8):

$$\int_{r_a}^{r} r' dr' = \frac{\mu V_a}{\ln(r_c/r_a)} \int_0^t dt'$$

$$\Longrightarrow \quad r = r_a \left[1 + \frac{2\mu V_a t}{r_a^2 \ln(r_c/r_a)}\right] = r_a \sqrt{1 + \frac{t}{t_0}}, \tag{2.3.9}$$

and

$$t_0 = \frac{r_a^2 \ln(r_c/r_a)}{2\mu V_a} = \frac{r_a}{2\mu E_a} \tag{2.3.10}$$

where $E_a = \dfrac{V_a}{r_a \ln(r_c/r_c)}$ is the electric field strength on the anode surface. t_0 determines the time scale of the ion motion and of the induced signal.

Substitute $r = r_a\sqrt{1 + t/t_0}$ into Eq. (2.3.7a) and Eq. (2.3.7b), we can write Eq. (2.3.6) as:

$$\begin{aligned} i_A &= q_0 \frac{\mu V_a}{[\ln(r_c/r_a)]^2} \cdot \frac{1}{r_a^2} \cdot \frac{1}{1 + t/t_0} \\ &= q_0 \frac{1}{2\ln(r_c/r_a)\, t_0} \cdot \frac{1}{1 + t/t_0} \end{aligned} \tag{2.3.11}$$

while the signal current in the anode readout electronics is:

$$i_a = -i_A = -q_0 \frac{1}{2\ln(r_c/r_a)\, t_0} \cdot \frac{1}{1 + t/t_0}, \qquad t \le t_c = t_0 \left[(r_c/r_a)^2 - 1\right] \tag{2.3.12}$$

and the signal current in the cathode readout is:

$$i_c = -i_a = q_0 \frac{1}{2\ln(r_c/r_a)\, t_0} \cdot \frac{1}{1 + t/t_0} \tag{2.3.13}$$

Note that the relationship $i_c = -i_a$ is only valid for a two electrode system. In systems with multiple electrodes, the induced charge is distributed among many electrodes, and the time development of the signal may vary from electrode to electrode.

For an arbitrary electrode configuration, the Weighting-Field concept developed by Radeka [11] is more convenient to use for calculating the induced charge.

2.3.3 Anode Avalanche Angular Distribution

The avalanche process is not uniformly distributed around the circumference of the anode wire. As illustrated in Fig. 2.3.2, it is concentrated towards the direction where the primary ionization takes place. This asymmetry results in the angularly localized positive ion distribution, which in turn results in asymmetry in the cathode induced charge distribution. The avalanche angular distribution is dependent on the anode wire diameter, avalanche size, gas mixture and type of radiation.

Fig. 2.3.3 shows some results [12] on the angular distribution of the avalanche around the anode wire in an argon-methane mixture with different anode wire diameters. The measurements were performed with an azimuthally segmented cylindrical proportional counter.

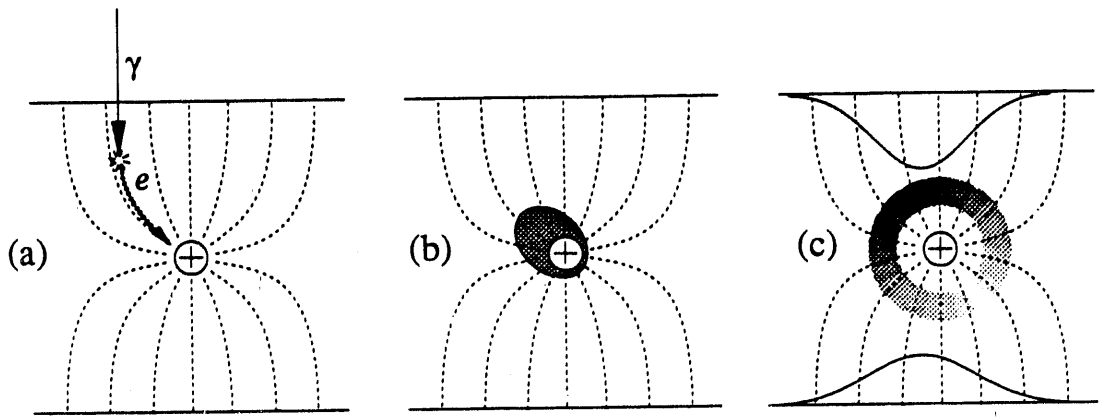

Figure 2.3.2: Illustration of the avalanche process leading to the angular distribution of avalanche, and the shift of induced charge distribution. (a) A photon traversing the chamber ionizes gas molecules and creates electron-ion pairs. The electrons drifts towards the anode wire along the electric field line. (b) Avalanche takes place and the angular charge density of the electron or ion is non-uniformly distributed around the anode wire in most cases. (c) Positive ions drift away from the anode wire along the electric field lines. The angular charge density of the ion is more concentrated in the direction of the primary ionization. The motion of the positive ion induces charge on both cathode planes. The asymmetry in the ion distribution causes changes in the centroid and width of the induced charge distribution on the cathodes.

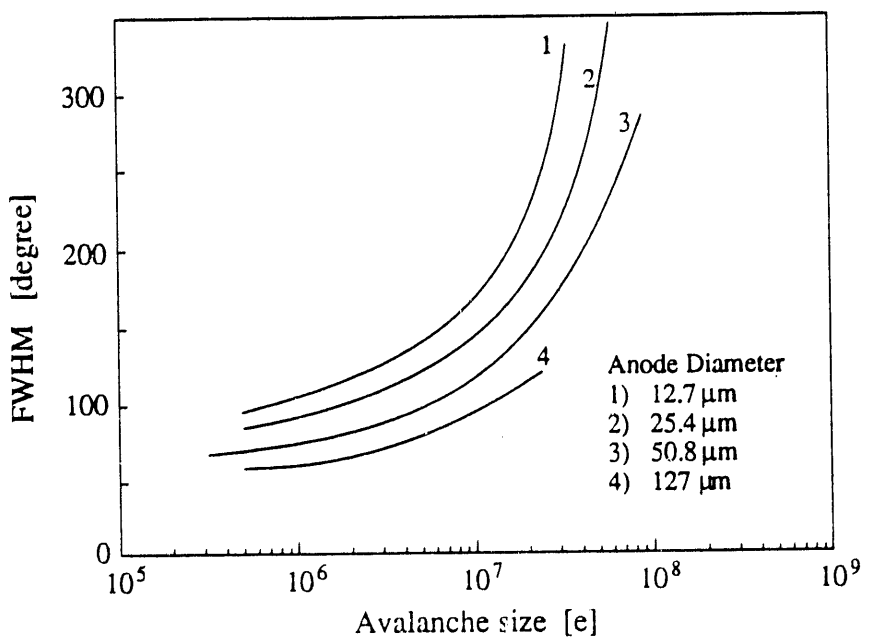

Figure 2.3.3: FWHM of the angular distribution of the avalanche as a function of avalanche size for 5.9 keV x-rays in 90% argon 10% methane mixture.

2.3.4 Induced Charge Distribution on the Cathode

The induced charge density distribution on the cathode plane due to the anode avalanche has been described in several publications [13–17]. The results are summarized here.

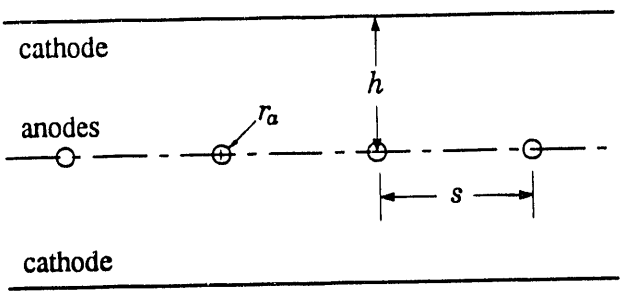

Figure 2.3.4: Cell geometry and parameters of an MWPC

A simple model to calculate the induced charge distribution is to use the image charge method [18]. Ignoring the presence of the wires, the system can be considered to consist of only two infinite parallel conducting planes. The charge created by the anode avalanche is located in between the two planes. We assume that the charge is pointlike and is located midway between the two planes separated by $2h$. The image charges are an infinite series of point charges at intervals $2h$ along a line perpendicular to the cathode planes with alternating polarities. The induced charge distribution is proportional to the induced electric field at the surface of the cathode plane of interest. It can be described by a simple expression:

$$\rho(x,y) = \frac{-Q_A}{2\pi} \sum_{n=0}^{\infty} (-1)^n \frac{(2n+1)\,h}{\left[(2n+1)^2 h^2 + x^2 + y^2\right]^{3/2}} \tag{2.3.14}$$

where Q_A is the avalanche size.

The charge distribution along any one dimension can be derived by integrating Eq. (2.3.14) over the other dimension:

$$\rho(x) = \int_{-\infty}^{\infty} \rho(x,y)\,dy$$

$$= \frac{-Q_A}{\pi} \sum_{n=0}^{\infty} \frac{(2n+1)\,h}{(2n+1)^2\,h^2 + x^2}$$

$$= -\frac{Q_A}{4h} \operatorname{sech} \frac{\pi x}{2h} \tag{2.3.15}$$

The integral of the above expression is:

$$\int_{x_1}^{x_2} \rho(x)\,dx = -\frac{Q_A}{\pi} \left[\arctan\left(e^{\pi x/2h}\right)\right]_{x_1}^{x_2} \qquad \text{for} \quad 0 \le x_1 \le x_2 \tag{2.3.16}$$

A three parameter empirical formula was developed by Gatti et al., [13] for the induced charge distribution along the anode direction. Mathieson et al., [14,16] calculated the exact one dimensional distribution for the direction along and perpendicular to the anode wires. They also developed a single parameter empirical expression based on the Gatti formula [15,17]. It was found that the difference between the induced charge distribution along the anode wire direction (ρ_1) and the distribution perpendicular to the wires (ρ_2) is negligible for all practical purposes. The single parameter formula is given, as a function of a normalized coordinate λ ($\lambda = \frac{x}{h}$), as the following:

$$\frac{\rho(\lambda)}{Q_A} = K_1 \frac{1 - \tanh^2(K_2\lambda)}{1 + K_3 \tanh^2(K_2\lambda)} \tag{2.3.17}$$

where:

$$K_1 = \frac{K_2\sqrt{K_3}}{4 \arctan \sqrt{K_3}}$$

$$K_2 = \frac{\pi}{2}\left(1 - \frac{1}{2}\sqrt{K_3}\right)$$

K_3 is a parameter whose value depends on the geometry of the chamber. The values of interest in this work are shown in Fig. 2.3.5. The integral of Eq. (2.3.17) is:

$$\int \frac{\rho(\lambda)}{Q_A} d\lambda = \frac{K_1}{K_2\sqrt{K_3}} \arctan\left[\sqrt{K_3} \tanh(K_2\lambda)\right]. \tag{2.3.18}$$

Naturally, when $h/s = 0$, the geometry degenerates into two parallel plates. Under this condition, $K_3 = 1$ and Eq. (2.3.17) becomes identical to Eq. (2.3.15).

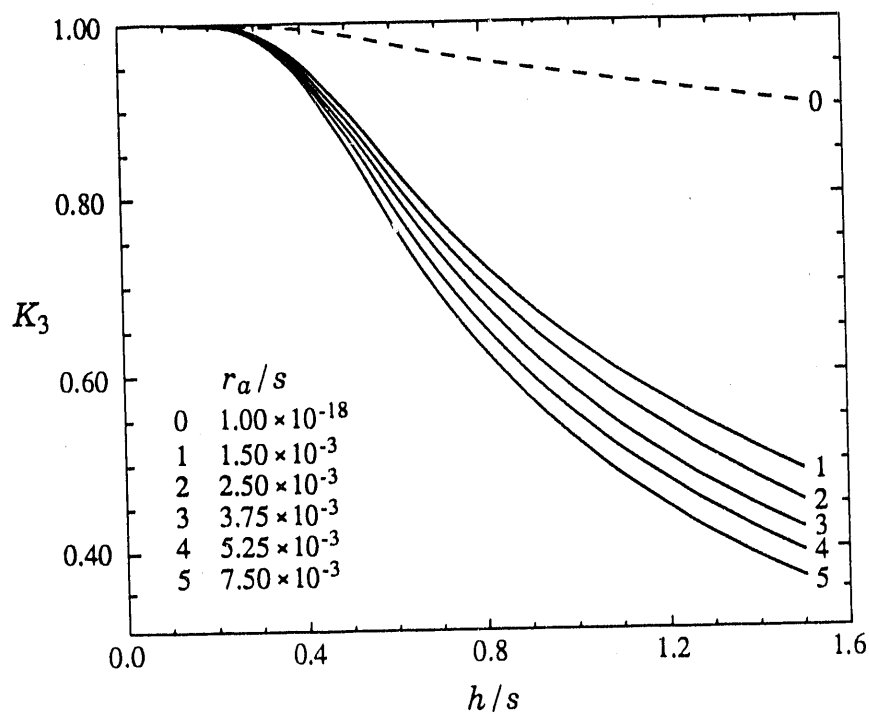

Figure 2.3.5: Values of K_3 in Eq. (2.3.17) as a function of chamber parameter h/s and r_a/s [17].

2.4. Signal Processing

2.4.1 Preamplifier

The amount of charge collected by the anode or the cathode in a gas proportional chamber is sufficiently small to require the use of low noise front end electronics. The preamplifier is the first stage of amplification for the signal from the detector electrode. The most commonly used type is the charge sensitive preamplifier, which converts the amount of charge from the input to a voltage output. It is an inverting amplifier with a feedback loop through a capacitor. The output voltage of the preamplifier is proportional to the input signal charge. Its gain is determined by the feedback capacitor. One of the low noise, high performance preamplifiers used throughout this work is BNL-IO-454-4, designed by Stephani of BNL. Fig. 2.4.1 is a photograph of the preamplifier and its circuit diagram.

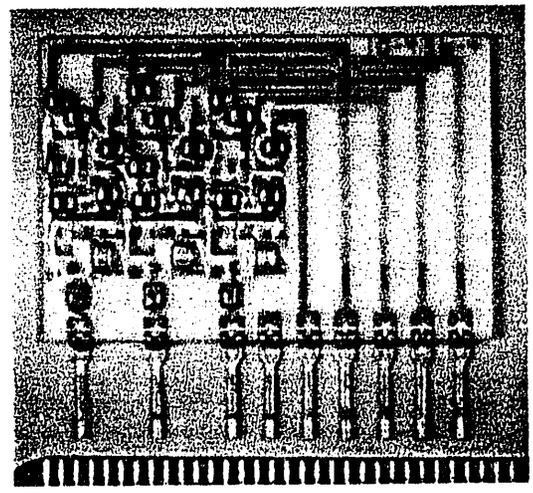

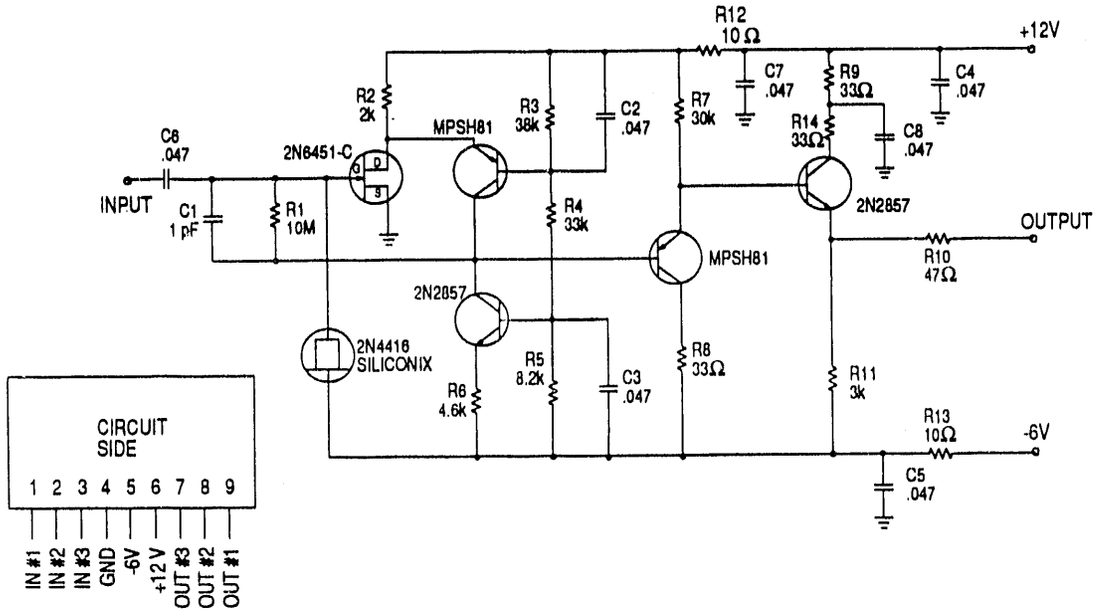

Figure 2.4.1: Photograph and the circuit diagram of the "triple preamplifier" used in the detectors.

2.4.2 Shaping Amplifier

The output of a preamplifier normally has a rather long decay time (10–100 μs typically). To reduce the duration of the signal pulse and to limit the bandwidth for the reduction of noise, shaping amplifiers are used to process the preamplifier output. Shaping amplifiers can consist of delay line clipping, or R-C, C-R networks.

2.4.3 Final Stage of Analog Signal Processing

The final stage of analog signal processing differs, depending on the application of the MWPC. The simplest process is to discriminate the signal from shaping amplifiers, which results in an output logic pulse when the input exceeds certain threshold. The discriminator output can be used to determine whether a particular channel has a hit. For applications where the avalanche size is of interest, the shaping amplifier outputs are connected to analog to digital converters (ADCs) which convert the analog signal into digital information to be used for computer analysis. The shaping amplifier outputs can also be sent to analog processing devices such as a Pulse Height Analyzer (PHA) or other application specific devices. An analog centroid finding system has been used throughout this work. Its operating principle is described in Appendix A [19].

2.5. Measures of Detector Performance

As a position sensitive detector, position resolution and position linearity are two of the most important measures of a detector's performance.

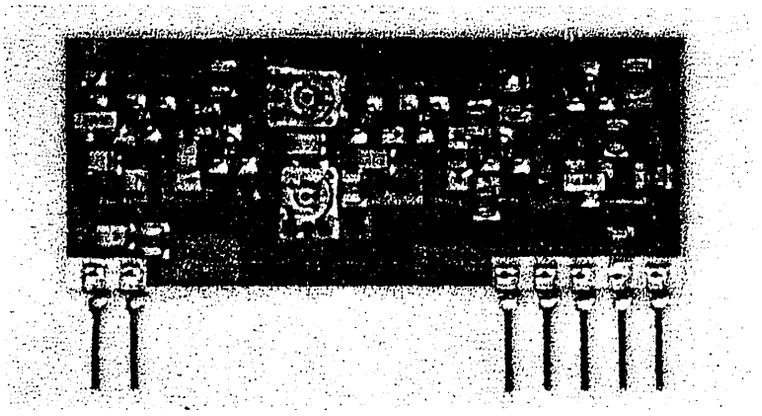

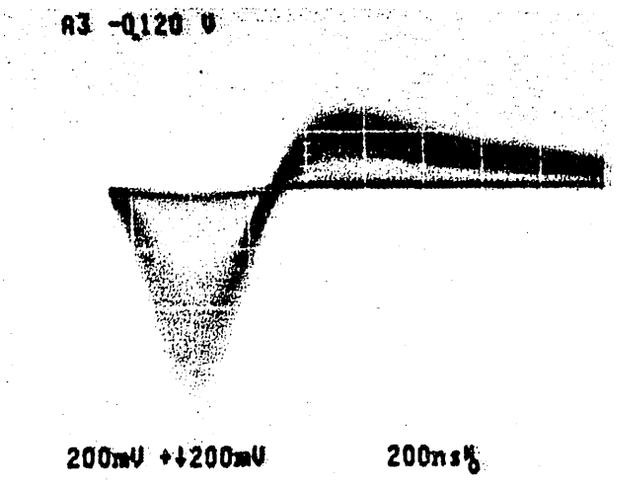

Figure 2.4.2: (a) Photograph of a 200 ns shaping amplifier. (b) Photograph of the cathode signal waveform of the shaping amplifier. Radiation was 15 GeV proton.

2.5.1 Position Resolution

Position resolution is defined as the standard deviation σ or the full width at half maximum (FWHM) of the reconstructed position distribution for a given incident particle or photon beam whose position distribution is a δ-function. The position resolution of a detector system is determined by many factors, such as the signal to noise ratio of the readout electronics, the physical spread of the primary ionization, the physical spread of the avalanche and the width and incident angle of the radiation.

2.5.2 Linearity and Uniform Irradiation Response

Assume a track's reconstructed position y is a function of the true position x: $y = f(x)$, as plotted in Fig. 2.5.1. Assume that a section (x_1—x_2) of the chamber is under uniform irradiation from a source whose spatial distribution is: $u(x) = \text{const.}$ Consider a small segment δl along the $y = f(x)$ curve, whose slope is $f'(x)$. Its projection on the x axis is δx and on the y axis is δy. Now all the flux from the uniform irradiation within the segment δx will be mapped to a response function $v(y)$ along the y axis within the segment of δy. (The effect of finite position resolution of the detector is neglected.) Therefore:

$$\delta x : u(x) = \delta y \cdot v(y)$$

or, if we normalize $u(x) = 1$, rewrite $v(y)$, we have:

$$v(y) = \frac{\delta x}{\delta y}$$

Let $\delta l \Longrightarrow 0$, we then have

$$v(y) = \frac{1}{f'(x)} \tag{2.5.1}$$

$v(y)$ is a normalized uniform irradiation response (UIR) as a function of the reconstructed position y, and $f'(x)$ is the derivative of the reconstructed position as a function of the true position. In an ideal position sensing detector, $f'(x) = 1$.

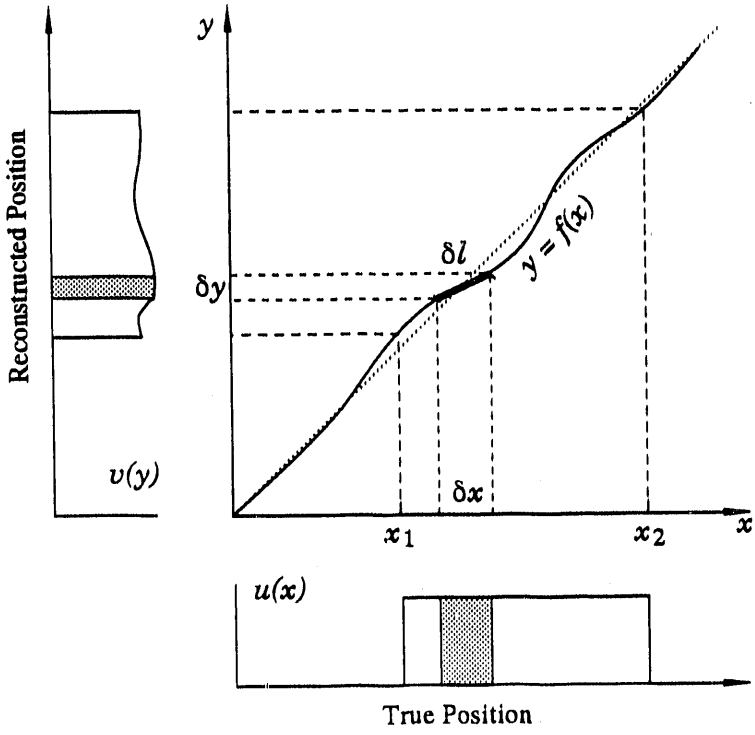

Figure 2.5.1: Principle of the Uniform Irradiation Response (UIR). $y = f(x)$ is the detector response function. $u(x)$ is the detector input function (uniform irradiation), and $v(y)$ is the detector response to such an input function.

For a position encoding system with good linearity, i.e. $f'(x) - 1 \ll 1$, we can ignore the difference between $v(y)$ and $v(x)$ and use the latter for convenience. Then:

$$f'(x) = 1/v(x)$$
$$f(x) = x_1 + \frac{1}{x_2 - x_1} \int_{x_1}^{x} 1/v(x')\, dx' \qquad (2.5.2)$$

In most of the position encoding systems discussed here, the position non-linearity has a periodic form. As a simple example, assume the periodic form is a sinusoidal function:

$$f(x) = x + A \sin\left(\frac{2n\pi x}{l_a}\right) \qquad (2.5.3)$$

where n is the frequency of modulation within a readout spacing l_a, A is the amplitude of the modulation ($2n\pi A \ll l_a$). The UIR function can be written as:

$$v(x) = \frac{1}{f'(x)}$$

$$= \frac{1}{1 + \frac{2n\pi A}{l_a} \cos\left(\frac{2n\pi x}{l_a}\right)}$$

$$\approx 1 - \frac{2n\pi A}{l_a} \cos\left(\frac{2n\pi x}{l_a}\right) \tag{2.5.4}$$

One of the commonly used measures of non-linearity is the differential non-linearity (DFNL), which is defined as:

$$\text{DFNL} = \frac{v_{\max} - v_{\min}}{(v_{\max} + v_{\min})/2} \tag{2.5.5}$$

Apply the expression from Eq. (2.5.4):

$$\text{DFNL} = \frac{2n\pi}{l_a} \cdot 2A \tag{2.5.6}$$

The above expression reveals the relationship between DFNL and the maximum reconstructed position error.

DFNL is a very stringent measure of the linearity of the detector encoding system because its value is derived from the maximum and minimum of the UIR spectrum. In some cases, a large DFNL could be caused simply by a "kink" in the response function $y = f(x)$ over a very small distance, or a large spatial frequency of modulation n, even though the actual position error could be quite small.

In many of the computer simulations on the linearity studies, a quantity "normalized rms position error" is used to evaluate the average response of a detector. Denoted by σ_{N}, it is defined as:

$$\sigma_{\text{N}} = \frac{1}{l_a N} \sqrt{\sum_{i=1}^{N} (y_i - x_i)^2} \tag{2.5.7}$$

where x_i and y_i are the true position and reconstructed position of a sample point, respectively, N is the total number of sample points. All the sample points are uniformly distributed within a range which is equal to the readout spacing l_a.

If the DFNL of a detector system is small, and the position error $y - x$ is a near sinusoidal function of x, it can be easily proven that:

$$\text{DFNL} = 4\sqrt{2}\pi n \sigma_{\text{N}}. \tag{2.5.8}$$

Chapter 3.
Review of Interpolating Methods in MWPCs

A single plane of a conventional MWPC gives positional information of the incident particle in one direction, and the position resolution is given by the anode wire pitch ($\sigma = s/\sqrt{12}$). An interpolating method is one in which signals from a few readouts can be processed to obtain position information much finer than the readout spacing.

Interpolating methods have been used in many charged particle or photon detectors. They can be roughly divided into three categories: resistive charge division, capacitive charge division and geometrical charge division.

3.1. Resistive Charge Division

In a proportional gas chamber, an avalanche creates signals on both the anode and cathode. One or both of the two signals can be used for position measurement. A detector using resistive charge division has finite resistances in its readout electrodes. The charge created by the avalanche is collected by more than one readout. Using the fact that the amount of signal collected by the readout is inversely proportional to the resistance between the signal source and the readout node, the position of the avalanche can be determined.

3.1.1 Charge Division with Resistive Anode Wire

Resistive electrodes have been used in many forms in radiation detectors. For instance, they were used by Schottky in 1930 with photodetectors, used in semiconductor detectors by Louterjung et al., and in spark chambers by Charpak et al. in 1963 [20].

The most commonly used position sensitive detectors with resistive electrodes use the charge division method. Reference [21] describes a single wire proportional counter using resistive anode charge division. Reference [22] describes a two dimensional MWPC with resistive charge division on both anode wires and cathode grids.

Reference [23] describes a large scale MWPC system using the resistive charge division method (see Fig. 3.1.1). In this system, a position resolution (σ) of 0.4% of the anode wire length (1.2 m long) was achieved. The charge division with resistive electrodes is independent of the capacitance and resistance of the electrode. It can be easily adapted in various applications.

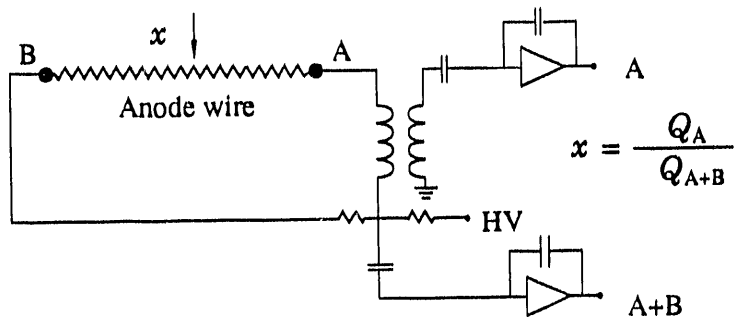

Figure 3.1.1: Schematics of a large scale MWPC with resistive charge division

The theoretical analysis of such systems is described in Refs. [24] and [25]. Several readout configurations were discussed in Ref. [25].

3.1.2 Resistively Coupled Cathode Strips and Wires

Another charge division scheme was introduced by Radeka et al., [19]. This method utilizes the induced charge on the cathode of an MWPC. As illustrated in Fig. 3.1.2, one or both cathode planes were divided into strips interconnected by resistors. Certain strips at regular intervals were connected to charge sensitive preamplifiers. The centroid of the induced charge on the cathode (in the direction across the strips) can be calculated by using signals from only a few readout channels. This method equally applies to the special cases of cathode strips—individual or group of interconnected cathode wires.

The position resolution of such a system is primarily determined by the signal to noise ratio and the readout spacing. An optimal performance in position resolution with a minimum number of electronic signal channels can be achieved with this

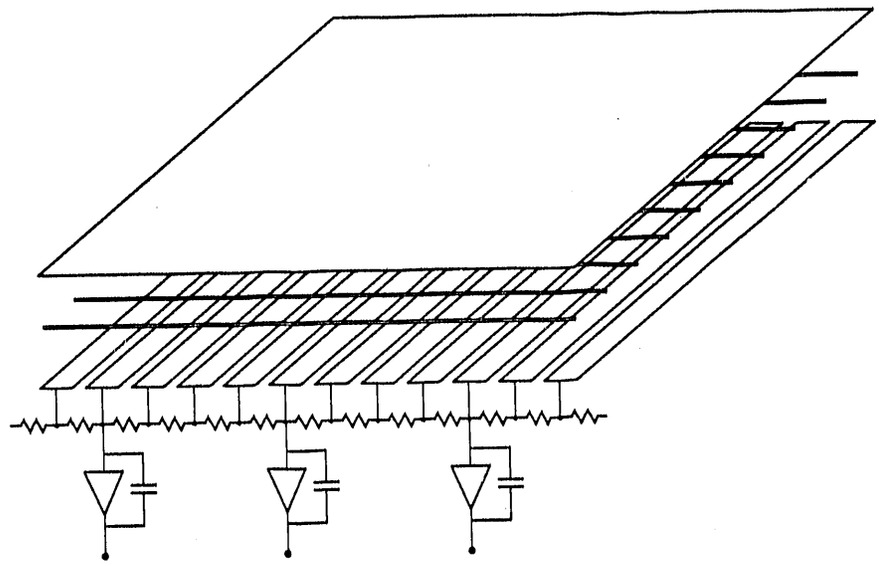

Figure 3.1.2: Schematic structure of an MWPC with resistively coupled cathode strips

"subdivided" resistive charge division method. Typically, no more than three readout channels are used to perform centroid computation to minimize the noise contribution from preamplifiers. The position linearity of the system is determined by the uniformity of the resistance, the width of the individual strip and the matching of time constants of the electrode and the electronics [19]. Because the centroid finding is performed locally, the position resolution is independent of the dimension of the detector. Application of this readout system has been reported in Refs. [26–27].

3.2. Geometrical Charge Division

As discussed in Chapter 2, the induced charge on the cathode plane from an avalanche is spread over a localized area. The other type of interpolating position sensing MWPCs uses specially shaped electrodes to sample the avalanche charge. The amount of charge induced on the electrodes varies with the position of the avalanche. The position of the avalanche therefore can be determined with good accuracy.

3.2.1 Strip Cathode

The simplest geometry uses cathode strips side by side with strip widths slightly less than the anode-cathode spacing to sample the induced charge. Each of the strips can be directly connected to a preamplifier [28]. In fact, the best position resolution from a gas proportional chamber was obtained in a detector with this type of strip cathode [29]. Closely spaced cathode wires can also be used for this purpose. The optimum width of the strips is discussed in Ref. [13].

3.2.2 Wedge and Strip Cathode

The Wedge and Strip electrode is a classical example of the geometrical charge division method. Introduced around mid 1960s by Anger [30] to be used as the anode of a photomultiplier tube, it became a very popular two dimensional position sensing method, and it has evolved into several other variations [31].

The original wedge and strip electrode is shown in Fig. 3.2.1: Electrodes A and B are wedge shaped. Their width varies linearly along the y direction. Therefore the y coordinate of an event centroid can be determined from the ratio: $\frac{A-B}{A+B}$ or $\frac{A}{A+B}$, where A and B are the electric charge signals collected on electrodes A and B respectively. Along the x direction, the width of electrode C increases while that of electrode D decreases. Therefore the x coordinate of an event can be determined by the ratio: $\frac{C-D}{C+D}$ or $\frac{C}{C+D}$. It is obvious that the position linearity of the system depends critically on the footprint of the induced charge. That is, the spread of the induced charge must cover several groups of the wedges and strips in order to achieve a good position linearity. Fig. 3.2.1b&c show two variations of the wedge and strip electrode pattern.

Wedge and strip electrode has also been used as the cathode plane of MWPCs. Reference [32] describes both microchannel plate detector systems and MWPC systems using wedge and strip electrodes. The electrode pattern used in the MWPC is the same as shown in Fig. 3.2.1b. It is important to keep the spacing between anode plane and the wedge and strip cathode plane larger than the period of the wedge and strip pattern, so that the footprint of the charge induced on the cathode plane is spread over several wedge and strip patterns.

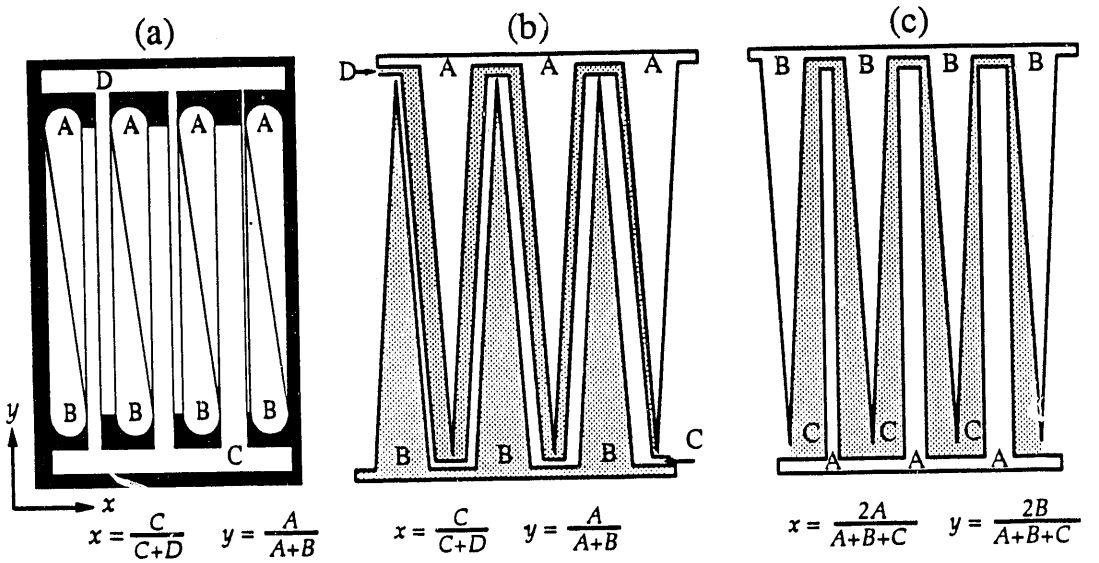

Figure 3.2.1: (a) The original wedge and strip electrode developed by Anger. (b, c) Variations of the wedge and strip pattern.

This is a true two-dimensional interpolating method. However, the reconstructed position in the direction across the anode wires suffers large modulations at a period of the anode wire spacing. This is due to the nature of the MWPC, in which avalanches are localized to near the anode wires. This limits the position resolution of an MWPC to the anode pitch in the direction across the anode wires.

The large electrode capacitance limits the maximum dimension of these electrodes, due to the electronic noise. The minimum size of such electrodes is limited by the etching technique.

3.2.3 Backgammon Cathode

Allemand and Thomas [33] developed this new method of position encoding in an MWPC. Fig. 3.2.2 shows the pattern of their Backgammon Cathode and the detector structure.

As in the case of the Wedge and Strip electrode, the period of the zigzag pattern must be maintained at a fraction of the anode-cathode spacing to avoid nonlinearity due to too coarse sampling of the induced charge. The large capacitance of the electrodes is not suited for high resolution and large area applications.

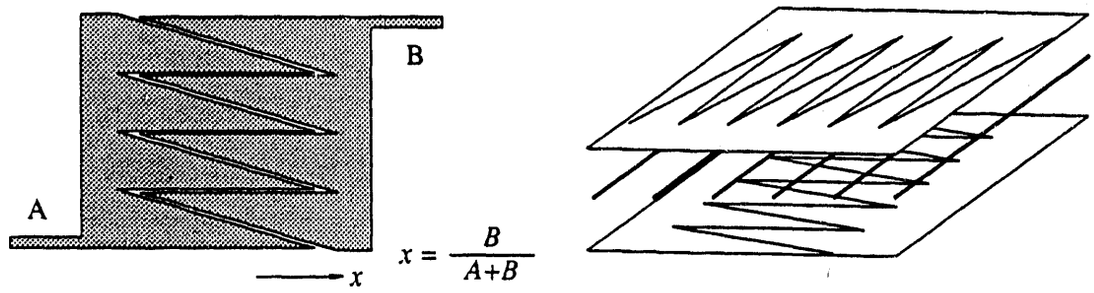

Figure 3.2.2: Backgammon Cathode and its application in an MWPC

3.2.4 Graded Density Cathode

Mathieson et al. [34] introduced a new "progressive geometry" position encoding method (see Fig. 3.2.3). It uses a plane of cathode wires with constant pitch which are electrically connected into two groups in such a manner that the linear density of each group changes linearly with distance. The centroid of induced charge on the cathode plane is shared by the two wire groups according to their local wire densities. Further improvements were made by subdividing the graded density cathode [35–36] and with tailored coupling capacitances and non-linear grouping of wires [37].

This interpolating method can be realized by conventional MWPC construction technique. However, it does require a large wire density to achieve a good position linearity. The special tailoring technique is somehow difficult to apply for arbitrary geometries.

3.2.5 Wedge or Diamond Shaped Cathode Pads, Vernier Method

Two similar types of cathode readout system (wedge shaped pads [38] and diamond shaped pads [39] were introduced in 1984 and 1985. Fig. 3.2.4 shows both cathode structures. In both methods, a pair of specially shaped electrodes are placed under and along an anode wire. Charge division is performed on the two electrodes to give position information within the period of the wedge or diamond pattern (vernier method). In both methods, additional position information is required to determine within which period the avalanche is located. This is typically done by using charge division with resistive anode wires. Both methods would exhibit large non-linearities

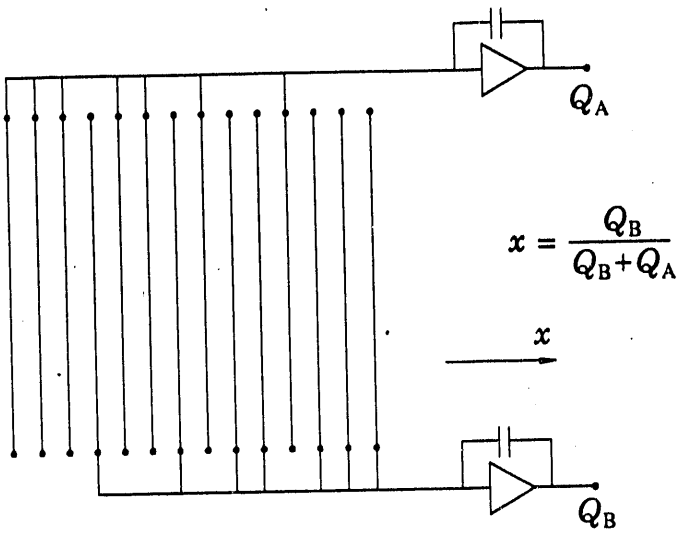

Figure 3.2.3: Graded Density Cathode

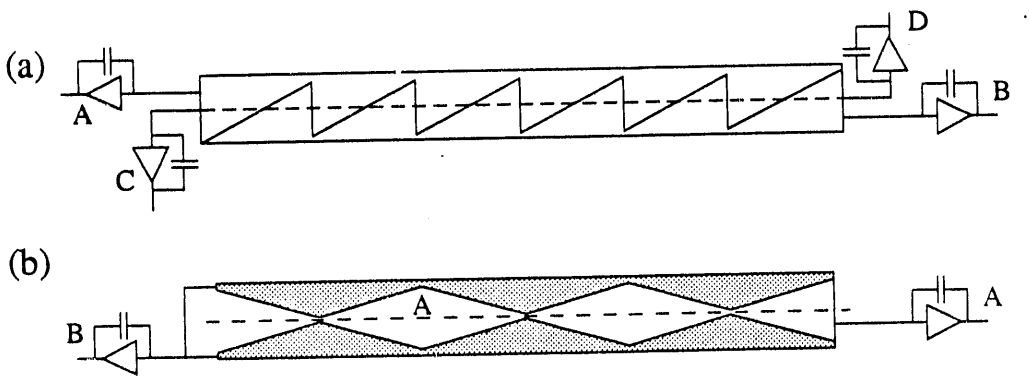

Figure 3.2.4: (a) Wedge shaped cathode; (b) Diamond shaped pad cathode.

near the vertices of the wedge or diamond pads. In the diamond pad method, another pair of electrodes (displaced along the wire direction by 1/4 of the diamond period) was placed on the other side of the anode wire to improve the system linearity.

3.2.6 Zigzag Strip Cathode

The zigzag shaped pad cathode was first described in Ref. [40]. A more detailed study was carried out by Mathieson and Smith [42]. As shown in Fig. 3.2.5, this cathode pattern is a combination of the strip cathode and the backgammon cathode.

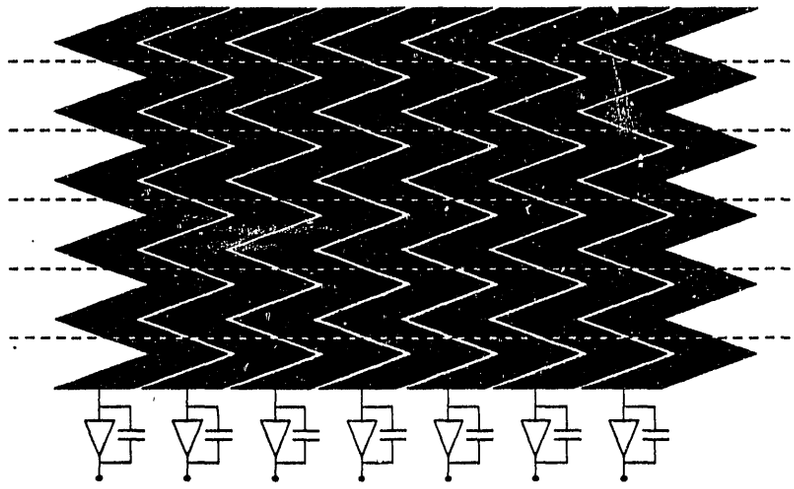

Figure 3.2.5: Zigzag strip cathode. The anode wire positions are indicated by the dashed lines.

This is a very versatile one dimensional interpolating method. It can be used in many areas of applications. The readout spacing is no longer restricted to be less than the anode-cathode spacing as in the case of straight cathode strips. However, its inter-strip capacitance is much larger than that of conventional straight strips, which will add noise to the electronics. Its maximum dimension is limited by the capacitance of the strip, while the minimum is determined by the etching technique of printed circuit board. Due to its close relationship with the interpolating method described in chapter 5, some of its properties are discussed there.

3.3. Capacitive Charge Division

Similar to the principle of resistive charge division, Smith et al. [41–42] introduced this charge division scheme, utilizing the intrinsic capacitive coupling among cathode strips. Schematics of two cathode layouts are shown in Fig. 3.3.1. In the "single intermediate strip" cathode, for example, the charge induced on the intermediate strip is coupled to the two neighboring strips via the inter-strip capacitance C_1. A fraction of the induced charge is lost to the ground due to the capacitance to ground C_2, which causes the non-linearity in the charge division. The position non-linearity

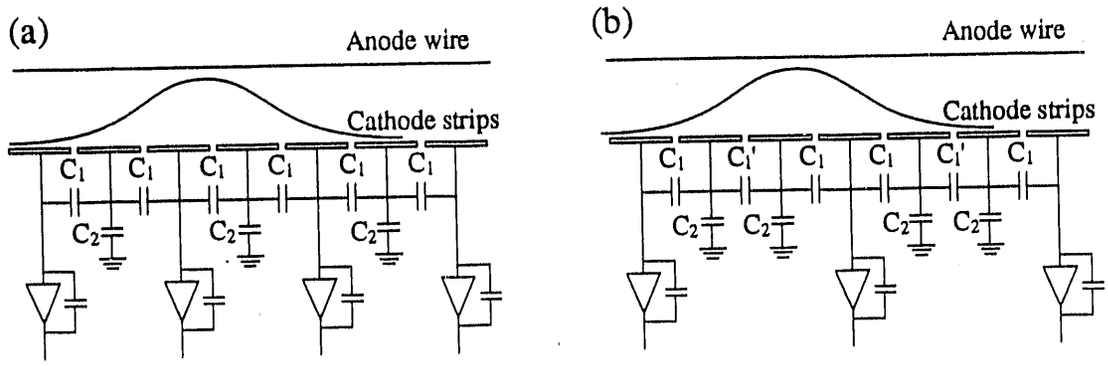

Figure 3.3.1: Examples of the capacitive charge division method. (a) Single Intermediate Strip method; (b) Two Intermediate Strip method.

is negligible if $C_1 \gg C_2$. In the case of the "two intermediate strip" cathode, the C_1' can be tailored to achieve a optimized position linearity.

Due to the presence of the capacitance between strip and ground, it is impossible to achieve perfect charge division. However, by minimizing the strip-to-ground capacitance and increasing the inter-strip capacitance, the differential non-linearity of such a system can be reduced to negligible level.

One of the advantages of the capacitive charge division method is the reduction of the capacitive load of the preamplifiers. In the case of the "single intermediate strip" cathode, the capacitance of the readout strip as seen by the preamplifier is nearly halved. The capacitive load of a "two intermediate strip" cathode strip has about 1/3 of the load of a conventional cathode strip. This reduction will improve the signal to noise ratio of the system.

One limitation of this capacitive strip cathode is that the readout spacing is limited to no more than about $2.5h$, because the width of each strip has to be less than $0.8h$ to maintain a good linearity [19,41]. However, it is possible to overcome this limitation by using the zigzag strips described in the previous section. The width of each zigzag strip is not limited by the anode-cathode spacing. The large inter-strip capacitance of zigzag strip will enhance the capacitive coupling.

Chapter 4.
Pad Chamber with Resistive Charge Division

4.1. Principle of Operation

The resistive pad chamber is a natural extension of the early designs of resistive cathode strip chambers. As shown in Fig. 4.1.1a, rows of rectangular conductor pads lie underneath the anode wires. A resistive strip with uniform resistance interconnects all the pads under an anode wire. Certain pads at regular intervals along a pad row are connected to the readout electronics. These pads are often referred to as readout nodes. The spacing between the readout nodes is denoted by l_a.

Fig. 4.1.1c illustrates the principle of charge division on such a cathode. When a charged particle or photon traverses the chamber, it ionizes the gas molecules and generates an avalanche near the anode wire. The charge (Q_i) induced on each pad (at position x_i) under the anode wire is equal to the integral of the cathode charge density over the area of the pad. The charge is collected by the nearest two preamplifiers tapped at positions (x_{k-1}, x_k) along the pad row. The amount of charge that goes to either side of the preamplifiers ($Q_{i,k-1}, Q_{i,k}$) is inversely proportional to the resistance values from this pad to the readout pads. It can be easily proved that (see Appendix B) the centroid of the induced charge distribution x_c, which is defined as:

$$x_c \equiv \frac{\int x\rho(x)\,dx}{\int \rho(x)\,dx} \tag{4.1.1}$$

can be calculated from the information obtained from the readout nodes:

$$x_c = \frac{\sum x_k Q_k}{\sum Q_k}. \tag{4.1.2}$$

provided that the length of the pad along the wire direction is kept below $0.8h$.

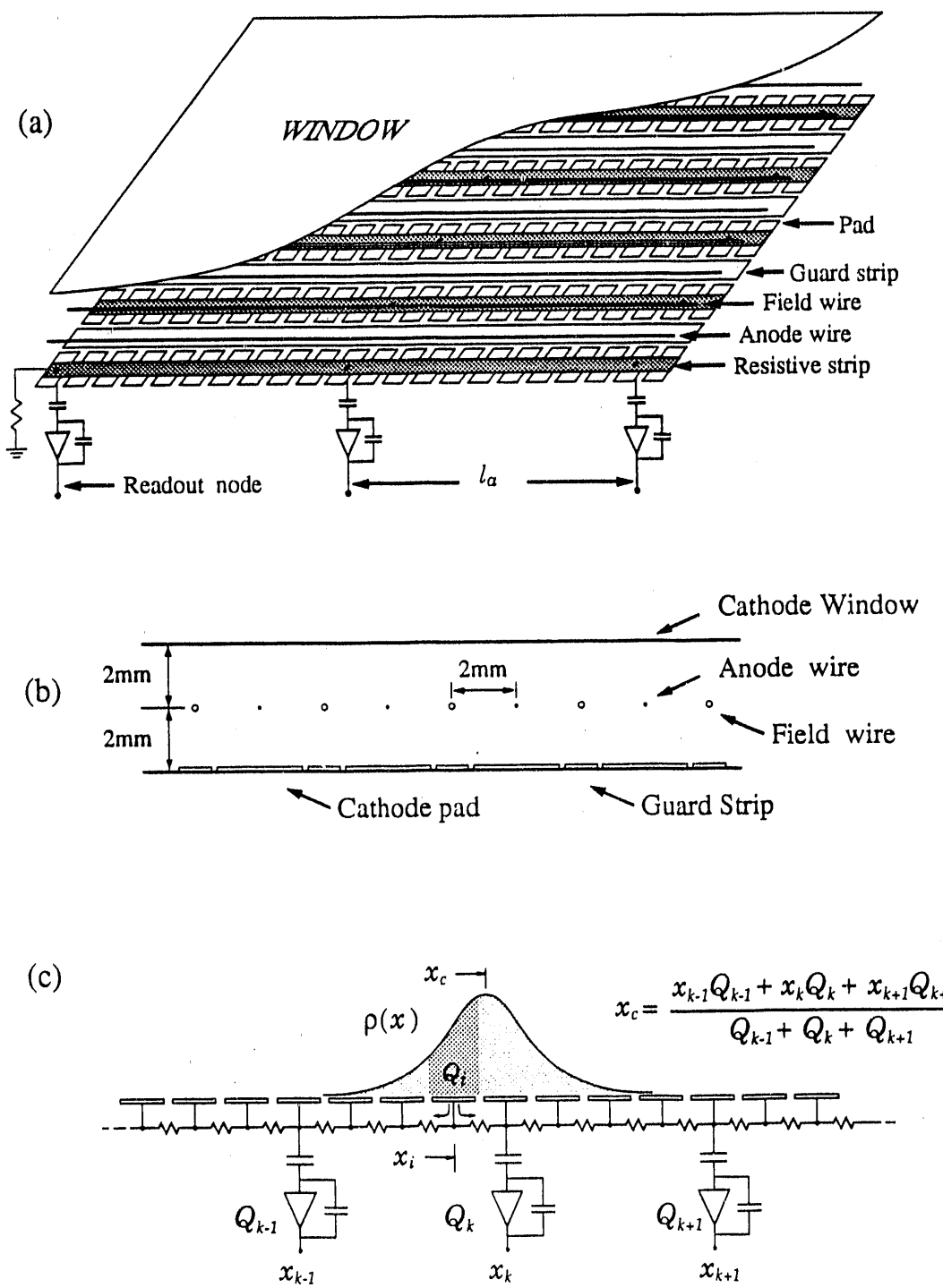

Figure 4.1.1: (a) A "3-D" view of a pad chamber structure, (b) A cross section of the pad chamber showing the cell geometry. (c) Principle of resistive charge division

4.2. Detector System Overview

Two chambers with resistive pad readout have been built at BNL. The detailed constructions of both chambers are discussed in Chapter 6. The following is a summary of their major parameters.

A prototype chamber was first built to study the performance and construction of such a detector system. It has 525 readout channels, which cover a sensitive area of 20 cm × 10 cm. The readout node spacing (l_a) is 1 cm. Each pad is 0.6 mm long (along the wire direction) and 2 mm wide. There are 10 pads per readout node. A wire plane consists of alternating anode and field wires is placed 2 mm above the cathode pad plane. There are 25 anode wires and 26 field wires. The diameter of the anode wire is 17.5 μm and that of the field wire is 125 μm. The spacing between the anode wire and the field wire is 2 mm. Another 2 mm above the wire plane is the cathode window. The cathode window and the field wires were at ground potential during operation. Argon (90%) and methane (10%) mixture (a.k.a. P-10) was used in this chamber.

A full-size chamber was designed and built for the heavy ion experiment (E-814) at the Alternating Gradient Synchrotron (AGS) of BNL. Some of its parameters are:

- 1016 readout channels; 26 cm × 16 cm active area; 40 anode wires, 41 field wires; The pad size is 0.8 mm in x by 2 mm in y;
- Wire plane to window spacing is 4 mm to get a larger primary ionization from particle tracks. The wire plane to cathode spacing is 2 mm.
- The readout spacing is 6 mm in the center of the active area, 15 mm at one end and 12 mm for the rest of the active area. This arrangement was to accommodate the anticipated track density of the experiment in order to maintain a good double track resolution.
- The gas mixture used was 50% argon and 50% ethane during most of the tests.

There were basically two types of readout system used in the pad chamber studies:

During the lab test, an analog centroid finding system [19] was used. The schematic diagram of the electronics is shown in Fig. 4.2.1. The ^{55}Fe source which generates 5.9 keV x-rays and a chromium anode source which generates 5.4 keV x-rays were used throughout the tests. The outputs of several on-board preamplifiers (maximum 15, due to the available electronics) connected to a row of pads were sent to the sample-and-hold module. They were shaped by a trapezoidal filter with a response about 1.4 μs wide and sampled. The sequential switch module sent the sampled signals to the centroid finding filter. Fig. 4.2.2 is a photograph of the sequential switch output. The anode signal was collected by a charge sensitive preamplifier and the output sent to a shaping amplifier. The output of the shaping amplifier was used by the centroid finding system as a trigger signal. This trigger signal, synchronized with the internal clock of the centroid finding system, was also used as the *start* signal of a time to amplitude converter at a later stage. Upon arrival of the trigger signal, the output from the sequential switch was convoluted with the centroid finding filter. A timing signal corresponding to the zero crossing time of the convoluted signal was generated and used as the *stop* signal in the time to amplitude convertor. The output of the time to amplitude convertor was analyzed by a pulse height analyzer.

As shown in Fig. 4.2.3, the chromium x-ray source was mounted on a stepping motor controlled x–y stage. The motion of the x-ray source can be controlled by a computer to an accuracy of 1 μm. The x-ray source can be used as a diffused source of uniform irradiation over an area of about 10 cm by 10 cm, or as a collimated beam with an aperture down to 13 μm by 500 μm. A monochromator can also be used to obtain mono-energetic x-rays.

The second readout system was employed in the heavy ion experiment. The schematic of this system is shown in Fig. 4.2.4. The cathode signals were processed by the on board preamplifiers. Transformers were used at the output for isolation purposes as well as impedance matching. Their outputs were sent through 50 m of individually shielded twisted pair ribbon cables to shaping amplifiers and then digitized by charge sensing ADCs. The digital information was stored on magnetic tape for off-line analysis.

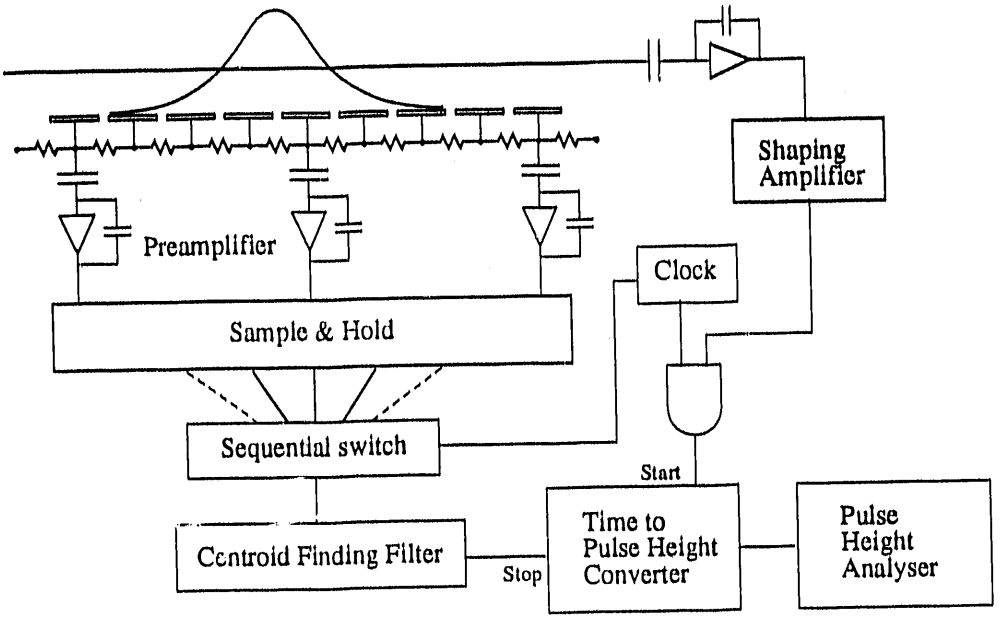

Figure 4.2.1: Schematic diagram of the electronic setup during x-ray lab tests.

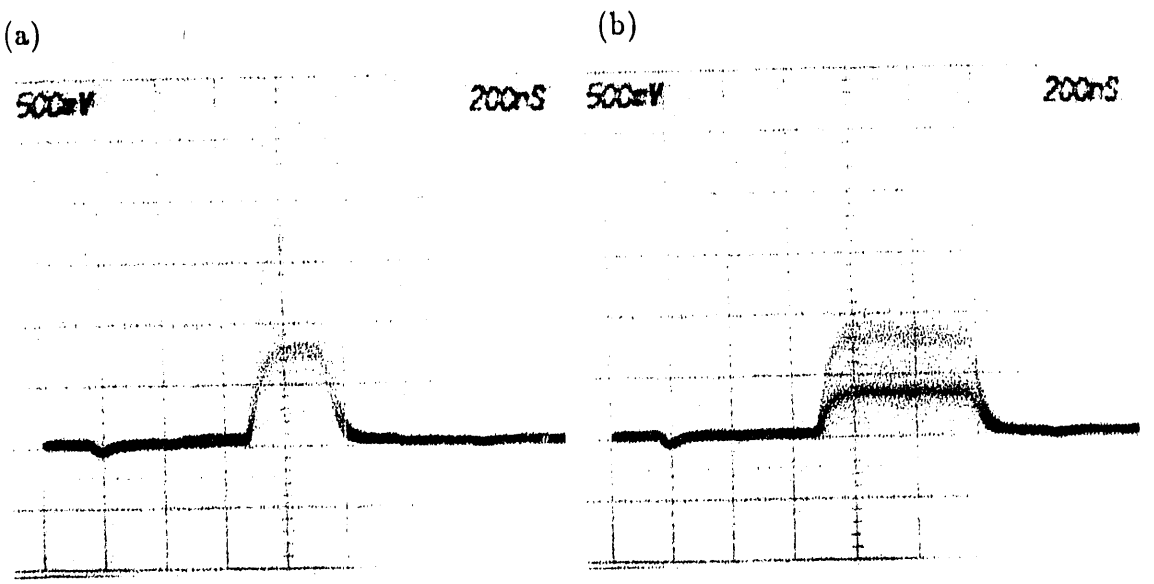

Figure 4.2.2: Photographs of two sequential switch output waveforms on an oscilloscope. The one on the left shows the waveform when the x-ray beam is located over a readout node. The one on the right shows the waveform when the x-ray beam is located midway between two nodes. The waveforms are convoluted by a specially designed bipolar filter response to give the centroid position.

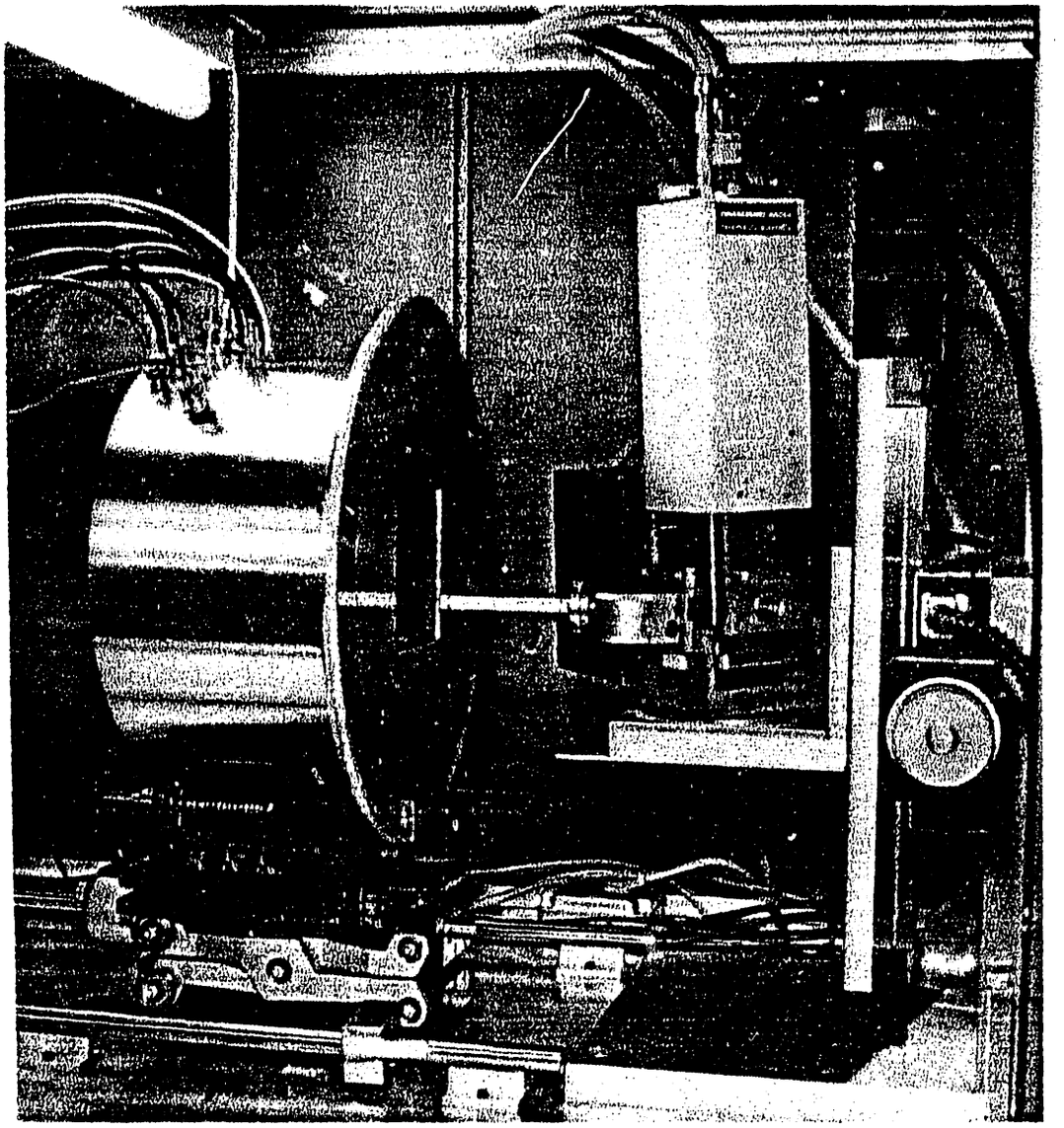

Figure 4.2.3: The x-ray source used during detector lab tests. The white vertical cylinder at the right hand side of the photo is the x-ray source. It houses an x-ray vacuum tube with a chromium anode and a cathode filament. The threshold voltage differential, between anode and cathode, for generating x-rays is 5.4 keV, and the intensity of the x-ray beam can be adjusted by controlling the voltage and current through the cathode filament. A monochromator with a collimator is mounted on the front side of the x-ray tube. The x-ray source is mounted on an x–y stage controlled by a pair of stepping motors, shown to the right of the x-ray source. The stepping motor can be moved in 1 μm increments in either axis, and has a total span of about 25 cm. The detector shown here is for an x-ray imaging study. A platform is mounted with ball bearings on a pair of stainless steel rails. Detectors mounted on the platform can be moved along the x-ray beam direction. For tests with uniform x-ray irradiation, the detector is moved to the left end of the rails, and the mono-chromator and collimator are removed. The whole system is enclosed in a radiation proof box.

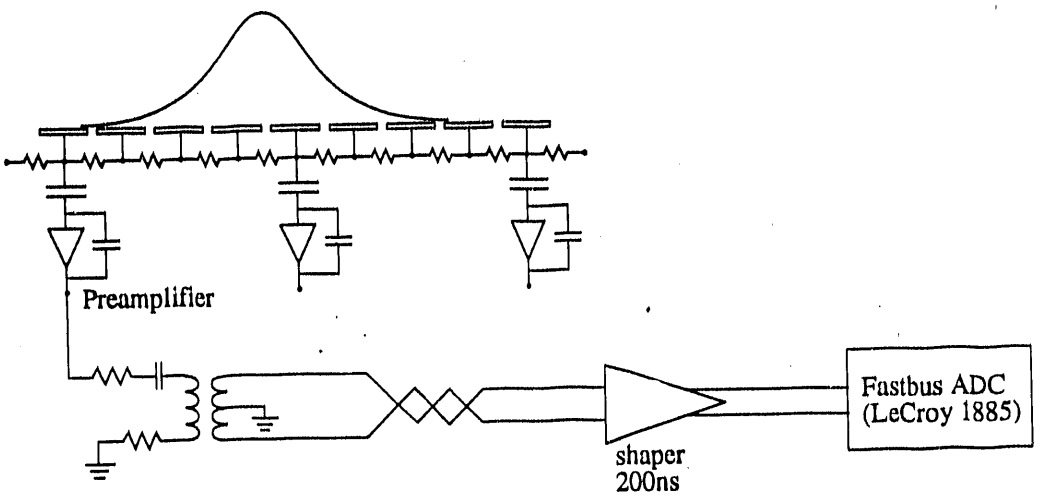

Figure 4.2.4: Schematic diagram of the electronics chain used in an experiment at the AGS of BNL

During the course of the experiment, particle beams such as proton, oxygen and silicon were used. Some data from the heavy ion running is presented in Appendix E.

4.3. Design Considerations

For detectors of this type, the dimensions of the active area are obviously defined by the application. The limitations on the size of the detector are based mostly upon mechanical considerations. Some of the mechanical difficulties, such as wire tension, flatness of the cathode plane, size of available printed circuit board materials, and location of readout electronics are discussed in Chapter 6.

The area each readout channel covers is primarily determined by the incident particle density and the occupancy of the detector. It is often a compromise between the double track resolution and the permissible number of readout channels. The centroid finding method is used only along the anode wire direction, while the coordinate in the other direction is given by the wire spacing. Therefore a small wire spacing is desired for applications where good position resolution in the direction across anode wires is required. This usually leads to a small anode to cathode spacing, for the following reasons:

i. It is preferable to have a square cell structure, i.e. the boundary of one anode cell is a square. This implies that the anode wire pitch s is equal to twice the anode to cathode spacing h. It is preferable to put ground or negatively biased field wires between anode wires for field shaping to enhance the charge collection efficiency.

ii. The induced charge distribution has a FWHM about $1.6h$. If the anode wire pitch is small while the anode-cathode spacing is large, the induced charge from one anode will be spread over rows of pads under other anode wires. The signal level on the primary pad row will be less, resulting in a lower signal to noise ratio. In many cases, the charge shared to other pad rows could complicate the pattern recognition along those pads and degrade the accuracy of the centroid reconstruction.

However, the tolerances of mechanical construction place a strong restriction on the anode-cathode spacing, especially for detectors with large active areas. It is a well known fact that improperly tensioned anode wires will deflect under the influence of the electrostatic force of the operating high voltages [43]. Small anode-cathode spacing may also cause high voltage breakdown. The variation in flatness of the cathode plane will result in large gas gain variation if not breakdown. In addition, since the ionization of gas molecules by a charged particle or a photon is a statistical process, its fluctuation in a thin detector is relatively large. Sometimes the energy deposition is insufficient to be detected, resulting in a reduction of detection efficiency. This problem can be solved, though, by using an asymmetrical cell structure, i.e. by increasing the spacing between the anode wire plane and the cathode window, while maintaining the spacing between the anode wire plane and the cathode pad plane. Cares have to be taken in such an arrangement to optimize the voltage setting of all electrodes for optimum detector operation.

As described in Chapter 2, the cathode charge distribution has a FWHM of approximately $1.6h$ for the cell geometry of this detector. Clearly the length of the pad along the wire direction will play a role in the linearity of the system. Calculations [19,41] on the performance of resistive cathode strip readout systems show that the differential non-linearity of the system is negligible if the width of the

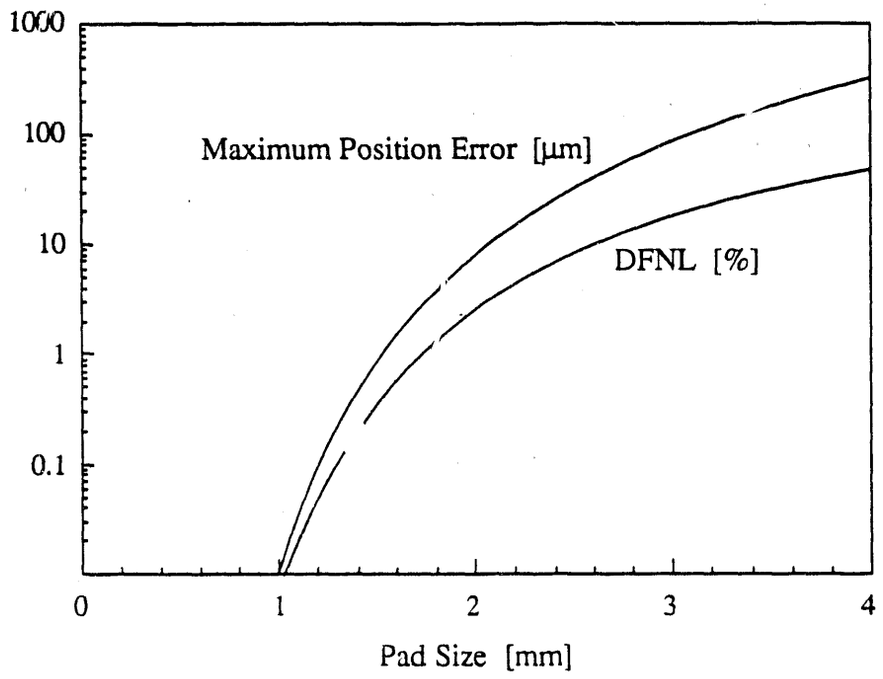

Figure 4.3.1: Computer simulation on the effect of pad size on the position linearity. The anode to cathode spacing is 2 mm. The maximum position error and differential non-linearity does not depend on the readout spacing l_a.

strip is kept less than $0.8h$. This rule is equally applicable to the choice of the pad size in a pad cathode. Fig. 4.3.1 shows the results of a computer simulation on the DFNL and maximum position deviation as a function of the pad size. Readout node spacings of 6 mm, 10 mm, 12 mm and 15 mm were calculated for both DFNLs and maximum position errors. However, the readout spacing does not affect the dependences in either case. This is because the non-linearity is due to the averaging of the induced charge over each discrete pad, as compared to a linear weighting over the width of the pad in the ideal situation (see Appendix B).

One also has to consider the fact that a certain minimum gap has to be maintained between pads for the deposition of resistive strip. Because only limited resistivity values of the resistive material are available, one needs to adjust the width and length (the gap between pads) of the resistor to reach a given resistance.

In the direction across the wires, a guard strip can be used between two adjacent pad rows. The primary function of the guard strip is to reduce the amount of

charge induced on adjacent pad rows. By doing this, however, the guard strip will take away a certain fraction of the signal charge. The width of the guard strips used in our detectors is 1/4 of the anode pitch [2].

The capacitance of the pad electrodes to ground is determined essentially by the cell dimension and readout node spacing. The resistance between the pads can then be determined by the following relationship:

$$\tau_F \approx R_n C_n \tag{4.3.1}$$

where τ_F is the effective integration time of the shaping amplifier, R_n and C_n are the resistance and capacitance of the pad electrodes per readout node. This will result in a fast signal resolving time while maintaining the optimal signal to noise ratio and position linearity.

The preamplifier used in this type of electrode has to be AC-coupled through a capacitor C_b so that the resistance between readout nodes will not affect the bias of the preamplifier. However, the value of the capacitor C_b has to be large enough such that [25]:

$$\tau_F \ll C_b R_n$$

where R_n is the resistance between readout nodes. If the time constant $C_b R_n$ is small compared to the time constant of the readout electronics, the induced charge will be equally shared by the readout nodes instead of being shared according to the resistive values. Since all the preamplifiers are AC-coupled, one or two resistors per resistive pad chain of pads are needed to provide the bias of the cathode pad electrode.

The design considerations on this type of electrode are discussed in detail in Ref. [25], some computer simulations are reported in Ref. [44].

4.4. Detector Performance

4.4.1 Calibration

Two calibration systems were built into both detectors, as shown in Fig. 4.4.1. Since there is no calibration input on the preamplifier, an alternative method was used to inject a pulser signal into the preamplifiers. On the prototype chamber, a copper strip 2.5 mm wide was etched on a ground plane 380 μm above the leads connecting the pads to the preamplifiers. The capacitance between the strip and the readout leads is approximately 0.1 pF. The capacitive coupling between the strips and the signal leads enable a known amount of charge to be injected into the input of the preamplifiers. However, there was some variation in the capacitance values for different channels. It is believed that the variation in the capacitance is due to a small variation in the spacing between the two planes, variation in the width of the readout leads, and the strip's close proximity to the preamplifiers. The results obtained from pulsing the cathode strip were primarily used for calibrating the linearity of the ADC system.

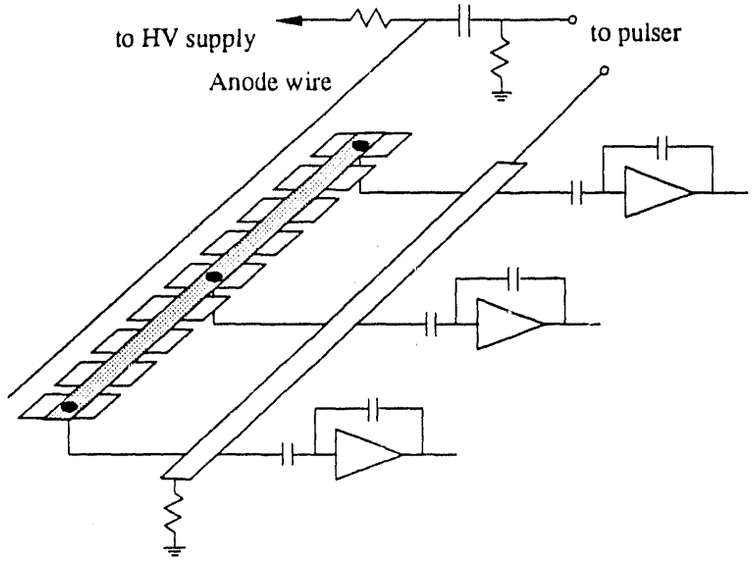

Figure 4.4.1: Calibration system for the pad chamber

The full-size chamber has wider calibration strips (1.27 cm) to increase the capacitance in order to accommodate the higher dynamic range of the ADC system.

The second calibration method was to pulse the anode wire, inducing charge on the cathode pads directly underneath. The anode wires were connected into several groups in such a way that neighboring anode wires were connected into different groups. Details of the anode wire plane are described in Chapter 6. The variation in capacitance between the anode wire and the pads is much smaller than that of the embedded strips. Because the variation is a reflection of the variation of induced charge on the readout pads, pulsing the anode wires is a more realistic and accurate way of calibrating the electronics gain.

The ADC system (LeCroy 1885F) used in the experiment requires calibrations at two separate input signal ranges. The capacitance between the anode and the pads is too small to be used to calibrate the high range of the ADC system. Two sets of calibration were performed. The first calibration was pulsing the strips on the readout board. Two sets of slopes ($S = dN_{\rm ADC}/dQ_{\rm pulser}$) were obtained for each channel in both ranges: $S'_{\rm high}$ and $S'_{\rm low}$. The second calibration was pulsing the anode plane. A set of slopes was obtained for the low range $S_{\rm low}$. The slope for the high range is then extrapolated by:

$$S_{\rm high} = S_{\rm low}\frac{S'_{\rm high}}{S'_{\rm low}}$$

The noise in the electronics chain was measured by injecting known amounts of charge on the calibration strip and it was found to be equivalent to 1500 electrons rms.

4.4.2 Gas Gain of the Chamber

The energy spectra of 5.9 keV x-rays and 14.5 GeV protons are shown in Fig. 4.4.2. The energy resolution for 5.9 keV x-rays was 18% in the full-size chamber at optimum voltage settings (see Chapter 6 for more details on the voltage settings).

The diameter of the anode wires used in both detectors is 18 μm. Studies [45] have indicated that by using anode wires with diameters in this range, space charge saturation will occur at large anode avalanche sizes. This is desired in our case, because of the large dynamic range in ionization seen by the chamber. As described

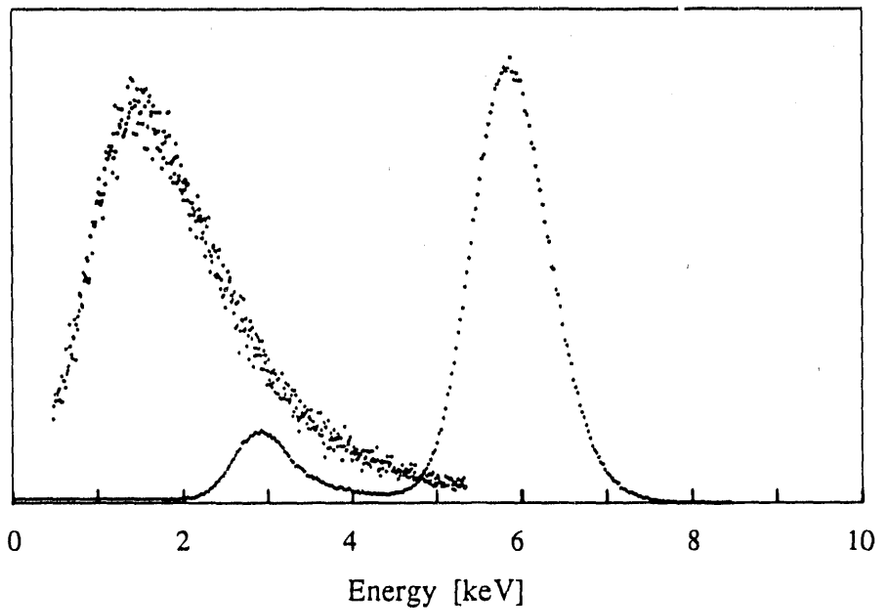

Figure 4.4.2: Energy spectra of 15 GeV protons and 5.9 keV x-rays from the full-size chamber. The vertical scales for both spectra are arbitrary. Gas used was 50% argon and 50% methane. The depth of the chamber gas volume is 6 mm.

in Chapter 2, the energy deposited in the detector volume by a charged particle is proportional to Z^2, where Z is the atomic number of the incident particle. So the primary ionization caused by a silicon ion is therefore a factor of 200 larger than that of a minimum ionizing particle. Simultaneous detection of both particles will require readout electronics with a very high dynamic range. It was the intention to utilize the space charge saturation effect of thin anode wires to reduce the dynamic range required to detect both minimum ionizing particles and heavy ions.

Fig. 4.4.3 shows the results of a series measurements on the anode signal charge as a function of the anode voltage for different radiation sources. The ratio in signal sizes between silicon ions and protons is about 50–100. The gas mixture used in the full-size chamber was 50% argon and 50% ethane. Compared with the P-10 gas mixture used in the prototype chamber, this gas has a faster electron drift velocity, but requires roughly 300 V higher anode voltage to obtain the same gas gain.

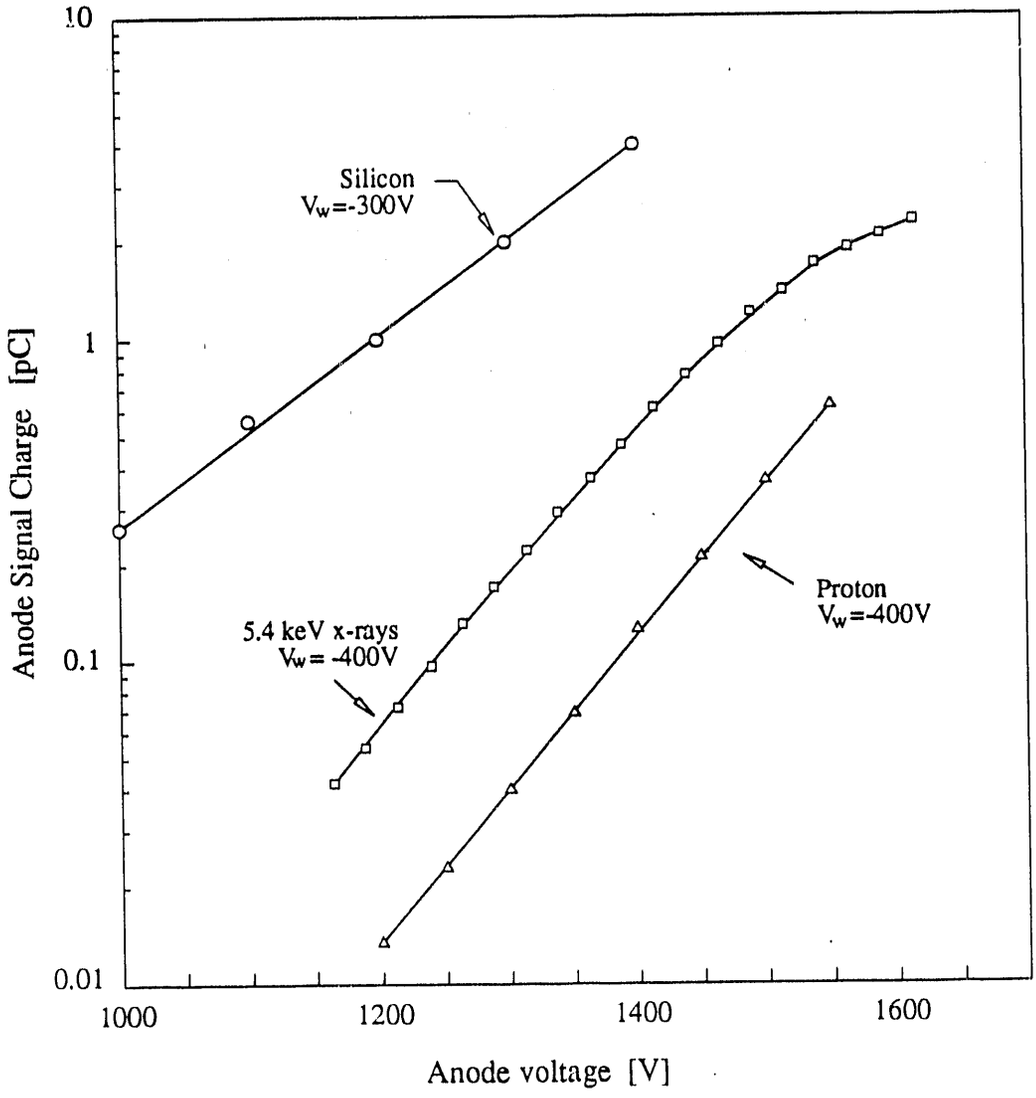

Figure 4.4.3: Anode avalanche charge as a function of high voltage. The results of the full-size chamber are shown here. The gas mixture used was 50% argon and 50% ethane. Anode charges were measured with a 200 ns shaping time. The window voltage settings are indicated on the graph. The depth of the chamber gas volume is 6 mm.

4.4.3 Linearity of the Chamber

The most important function of a position-sensitive detector is the ability to provide position information for an incident particle. Position linearity is one of the most important properties in determining the quality of a detector.

DFNL can be obtained from a position spectrum for uniform irradiation. Measurements have been made by obtaining a uniform irradiation response, with 5.4 keV x-rays, from a section of the pad cathode. For this measurement, the analog centroid finding system was used. The ADC system available during lab tests (LeCroy 2249A) has 10 bit resolution, which did not have enough dynamic range to give a realistic response.

For the uniform irradiation test, the pad chamber was mounted vertically at the far end of the x-ray box. The collimator of the x-ray source was removed. The preamplifier signals were fed to the centroid finding system and the resulting position signals analyzed with a pulse height analyzer. Fig. 4.4.4a shows the UIR across eight readout nodes of the DC1 prototype. The locations of the readout nodes, are indicated by tick marks on the abscissa. Differential non-linearity is better than 12%. The absolute position error as a function of x-ray position is shown in Fig. 4.4.4b. The position error is derived by evaluating the UIR spectrum. The reconstructed position can be derived from this equation:

$$y(x) = a + \frac{1}{b-a}\int_{-\infty}^{+\infty} v(y)\,dy \int_{-\infty}^{x} \frac{1}{v(y)}dy \qquad (4.4.1)$$

where x is the true position, assuming the irradiation is uniform and is limited to $a \leq x \leq b$. y is the reconstructed position. $v(y)$ is the counts from the UIR spectrum obtained on a pulse height analyzer.

If the differential non-linearity is small, one can consider the UIR spectrum as a function of the true position u instead of reconstructed position y. This results in the following approximation:

$$y(x) \approx a + \frac{1}{b-a}\int_{a}^{b} v(u)\,du \int_{a}^{x} \frac{1}{v(u)}du \qquad (4.4.2)$$

The position error curve shown in Fig. 4.4.4b was derived using this expression.

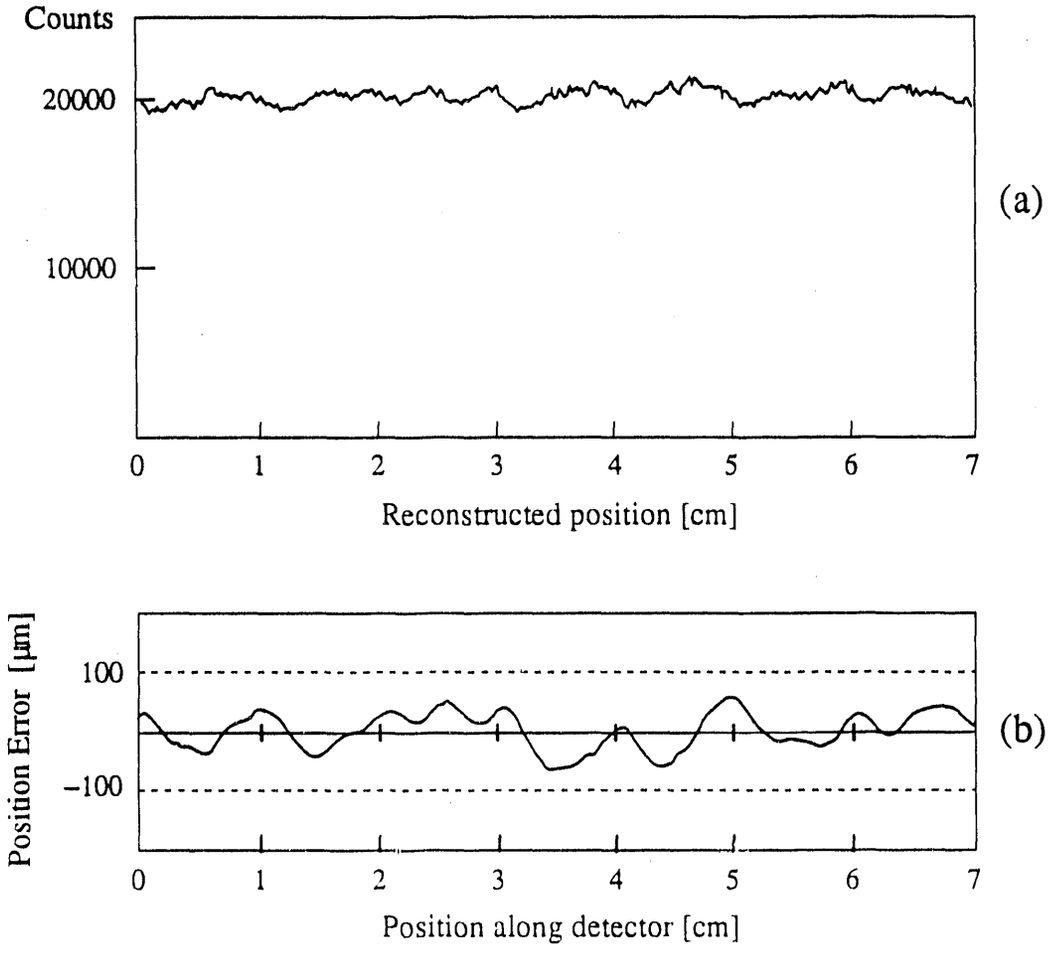

Figure 4.4.4: (a) Uniform irradiation response of 5.4 keV x-rays from the prototype pad chamber. (b) Absolute position error derived from the above spectrum

4.4.4 Position Resolution and Anode Charge

The position resolution from electronic noise alone for pad detectors with resistive charge division is determined as [19]:

$$\begin{aligned} \text{FWHM} &\approx 3a_f \frac{l_a}{Q_s}\sqrt{\frac{\tau_F kT}{R_n}} \\ &= 3a_f \frac{l_a}{Q_s}\sqrt{\frac{\tau_F}{\tau_n}}\sqrt{kTC_n} \end{aligned} \tag{4.4.3}$$

where a_f is a constant factor ($2 \leq a_f \leq 3$), Q_s is the amount of charge of the cathode signal, T is the absolute temperature, k is the Boltzmann constant, τ_F is the shaping time of the electronics, and $\tau_n = R_n C_n$ is the RC time constant of one readout node. A shorter shaping time will improve the resolution. However, if $\tau_F < \tau_n$, the position linearity will be degraded because the cathode signals are not completely collected by the readout electronics. The optimum choice is to make $\tau_F \approx \tau_n$. Under this condition, the position resolution given from the equation above is independent of the resistance between readout nodes [19].

A measurement of the position resolution was performed by using the 5.4 keV x-ray source with the monochromator and a collimator with a 15 μm wide aperture. At a fixed x-ray beam position, a large number of events were processed by the centroid finding filter and recorded with a pulse height analyzer. The width of the reconstructed position distribution was calculated as the position resolution of the detector.

Fig. 4.4.5 shows the position resolution as a function of the anode charge level for the prototype detector. The gas mixture used was 90% argon and 10% methane. The anode charge was measured with a 200 ns shaping time. The readout spacing in this detector is 1 cm. The measurements were made when the x-ray beam was located at approximately midway between two readout nodes. It will be shown later that the position resolution depends upon the location of the measurement as well.

The observed dependence of the resolution on the signal level was typical for a gas chamber operated under such conditions. At low charge levels, electronic noise, which is a constant, is the dominant limiting factor. Therefore the position resolution improves according to the signal to noise ratio ($1/Q_A$ relationship). For

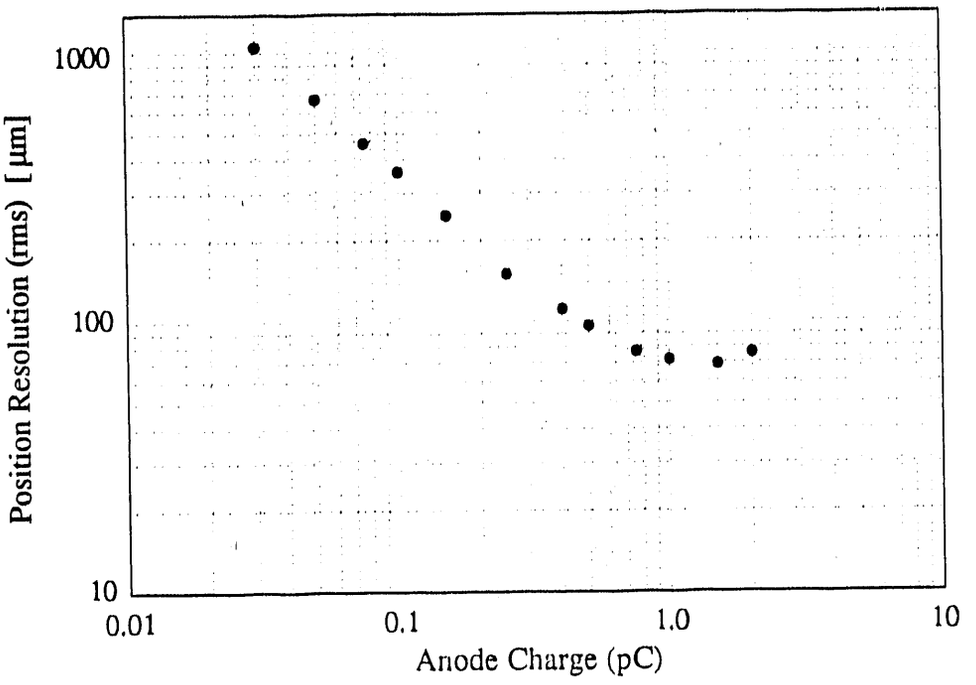

Figure 4.4.5: Position resolution as a function of the anode charge for 5.4 keV x-ray. l_a = 1 cm. Gas mixture was 90% argon and 10% methane. Anode signal was measured with 200 ns shaping time.

Q_A above 0.2 pC, however, the position resolution improves more slowly than $1/Q_A$ because of the increased influence of phenomena such as electron range and diffusion. A minimum value of about 70 μm (rms) was attained for $Q_A \approx 1.5$ pC. At higher charge levels, the position resolution starts to deteriorate due to the spreading of the avalanche along the anode wire.

4.4.5 Charge Ratio Method and Double Track Resolution

Fig. 4.4.6 shows one of the characteristics of this type of detector. By choosing signals from three adjacent readout nodes such that the one in the middle has maximum signal $Q_{\max}$, and plotting the ratio of the signal from the node on the left Q_{left} to $Q_{\max}$, versus the ratio of Q_{right} to $Q_{\max}$, one produces this charge ratio plot [46]. The width of the band is a direct measure of the signal to noise ratio and therefore the position resolution. The data for Fig. 4.4.6 were taken from the full-size chamber during a proton beam test at the AGS with an ADC system. The anode charge level

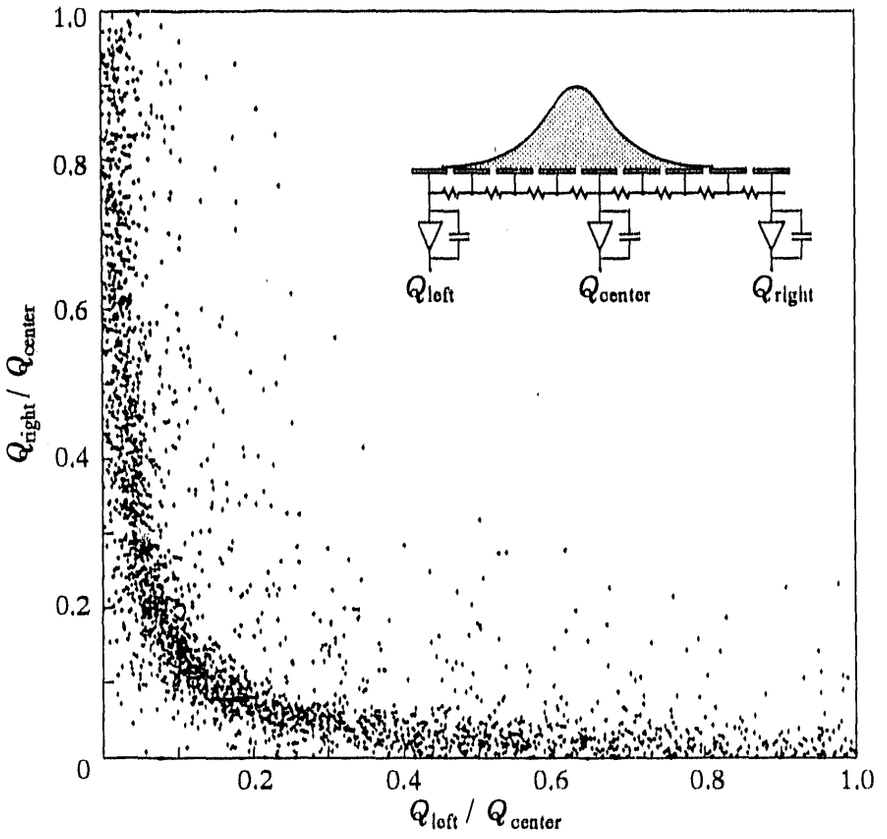

Figure 4.4.6: Charge ratio plot of the full-size chamber with readout spacing of 6 mm. Data was taken from a proton beam test. The charge level was about 0.15 pC. The position resolution was estimated to be about 120 μm.

was approximately 0.15 pC. The position resolution estimated from the width of the band is about 120 μm (rms) with a readout spacing of 6 mm.

This is a very simple and straightforward technique to estimate the detector's position resolution, since it does not require a well defined beam, neither does it require other auxiliary detectors to define the location of the incident tracks.

This method has also been used to calculate the position of the anode avalanche, as an alternative to the charge centroid method. It was reported that for certain detector configurations, it gives better results than the centroid method [46]. This is not due to any intrinsic property of the charge ratio method compared to the centroid method, since the charge ratio method is equivalent to the centroid method using

three nodes.* However, if the relation between the incident beam (or track) position and the two charge ratios is known, either by means of experimental measurements or calculations, the charge ratio method will give better results for detectors with poor linearities. It is equivalent to using a centroid finding formula modified to compensate for the non-linearity of a particular detector. The shape of the charge ratio curve depends on the detector geometries, such as the readout spacing, anode-cathode spacing and the type of electrode.

In addition, if the induced charge distribution spreads over more than three readout nodes, but the position encoding system is limited to analyze only three signal channels, using the charge ratio method will give better accuracy.

The shape of the band of the charge ratio plot can be used as a confirmation of the theoretical model of the cathode charge distribution. Sometimes a simple empirical expression is more convenient to use than the more accurate, yet complicated expression. Functional forms such as gaussian or hyperbolic secant have been used in many simulation programs. Their parameters can be optimized by fitting the simulated charge ratio curve to the experimental data.

Fig. 4.4.7 shows a series of simulated charge ratio curves using the expression developed by Mathieson et al.. In this case, the readout spacing is normalized to unity. The series of solid lines represent the results with different anode to cathode spacings. As the anode to cathode spacing increases, the curve moves further away from the origin. However, when the anode cathode spacing becomes too large compared with the readout spacing, say $h > 0.6 l_a$, the induced charge will spread over more than 3 nodes, which results in degradation of the position resolution due to the increase of noise charge from the large number of nodes. The dashed lines indicate the avalanche locations with respect to the center node for various h/l_a values. The dashed lines converge at (1,1) which is the extreme case when h/l_a is so large that all three nodes

* Let: $u = \frac{Q_A}{Q_B}$, and $v = \frac{Q_C}{Q_B}$ then:

$$x_c = \frac{Q_C - Q_A}{Q_A + Q_B + Q_C} = \frac{v - u}{u + v + 1}.$$

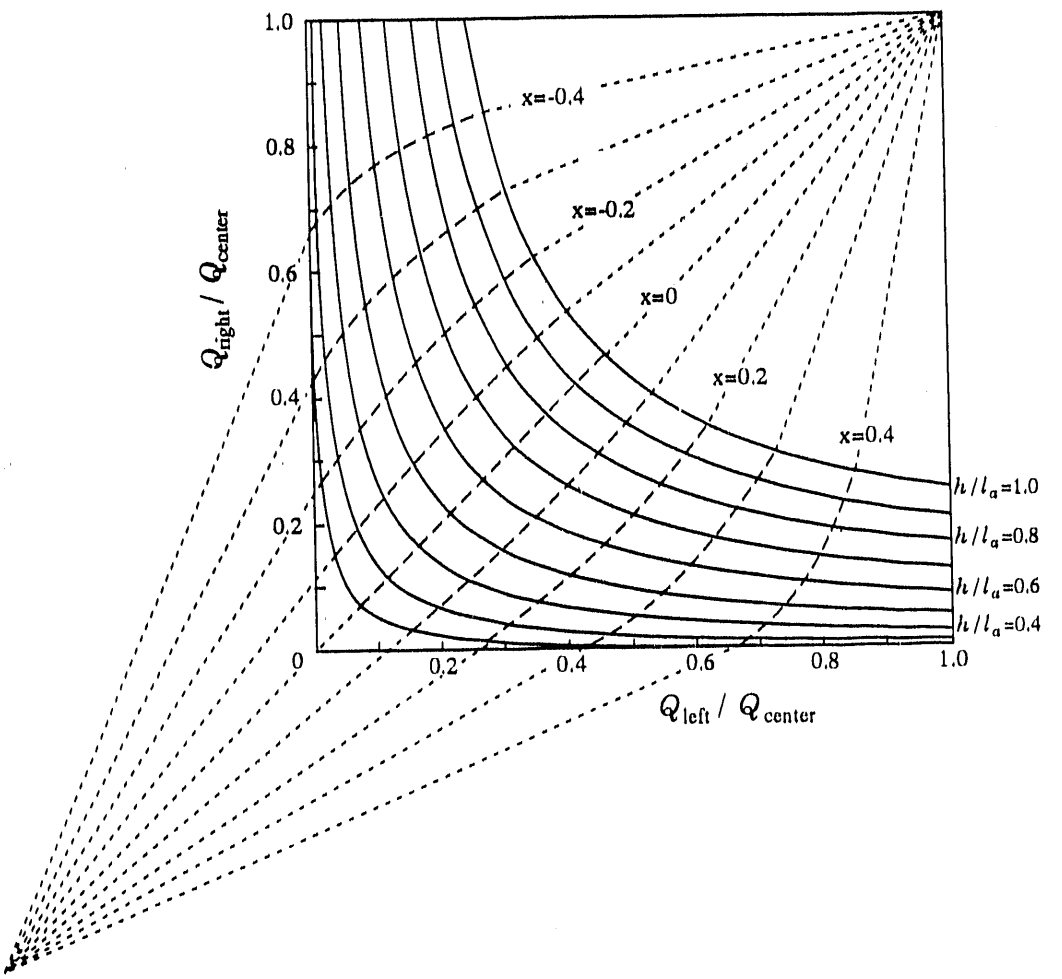

Figure 4.4.7: Computer simulated charge ratio plot with different h/l_a ratios.

collect the same amount of signal. In the other direction they point to $(-0.5, -0.5)$, which can be obtained from the expression:

$$x_c = \frac{v-u}{u+v+1}, \qquad \text{where}: \; u = \frac{Q_A}{Q_B}, \; v = \frac{Q_C}{Q_B}.$$

The above expression is only accurate when the induced charge spreads no more than three nodes, which is adequate for cases where $h < 0.4 l_a$.

Perhaps the most important application of the charge ratio method is to perform double track identification and separation. As can be seen in Fig. 4.4.7, for a certain detector geometry the h/l_a ratio is fixed. So for any given particle hit, its position on the charge ratio plot must lie close to only one of the curves. Any deviation from that curve indicates an abnormal induced charge distribution. The cause of such abnormality can be the crosstalk between readout channels, non-uniform gain in the electronics ..., and the most important one—multiple hits.

In interpolative readout systems such as the resistive and geometric charge division detectors described here, the ability to record multiple hits along a single anode wire is a very important. It is trivial to resolve two hits whose separation is larger than $2 \sim 3 \, l_a$. But what is the lower limit of the double track resolution?

A computer simulation was performed to understand the system response for double hits. It is based on a simple model: for each event, two hits are generated with certain separation between them. The induced charge distribution for each hit follows the Mathieson formula and the amount of induced charge for both hits is the same. There is no noise present. Fig. 4.4.8 demonstrates the results. The solid lines represent the charge ratio curve for certain double hit separations. The dashed lines represent the average position of the two hits. It seems obvious from the figure, that there is enough information to separate the double tracks even if their separation is below $0.5 l_a$. The family of the charge ratio curves has a shape close to a hyperbola. For example, the curve with $\delta x = l_a$ fits fairly well with the function: $(u+0.7)(v+0.7) = \text{const}$, while the curve with $\delta x = 0.4 l_a$ fits well to $(u+0.01)(v+0.01) = \text{const}$. The average centroid of the two hits can be calculated simply from the centroid formula. As a first order estimation of the double hit separation, the quantity uv is sufficient.

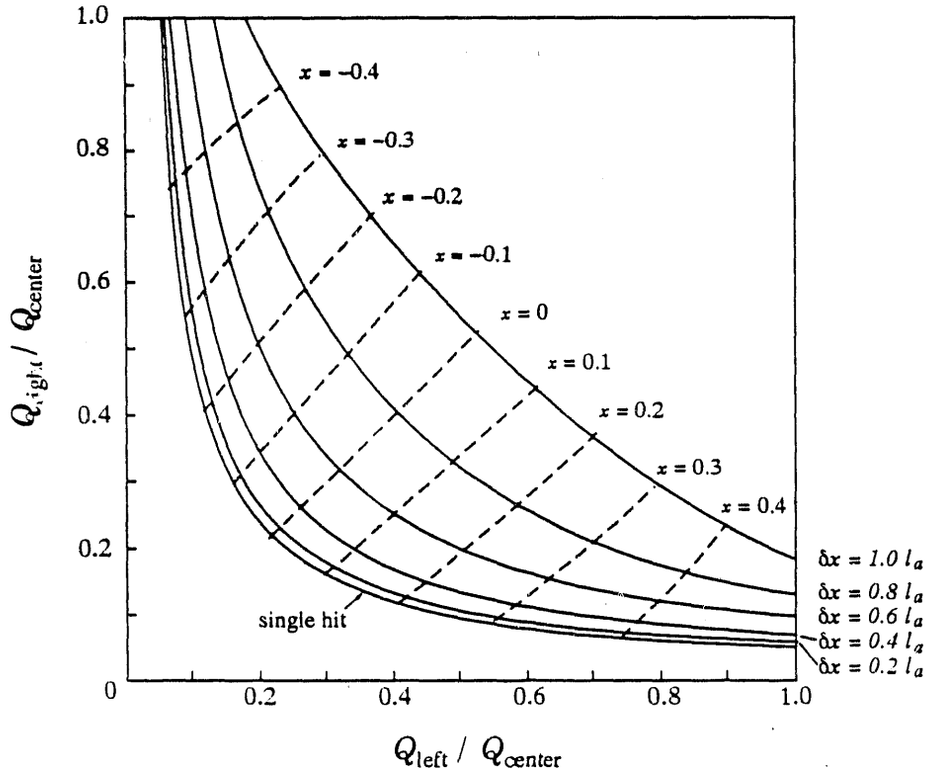

Figure 4.4.8: Simulations of the charge ratio curves for different double track separations. $l_a = 2h$ for all cases. This model assumes equal amount of signals from both hits. No noise is included.

The model used above is a very simple one. In reality, it is unlikely that both hits generate the same amount of signal. Further simulations included some pulse height distributions of the incident particles. Fig. 4.4.9 shows the results from hits with a wide Landau type pulse height distribution (data were taken from a proton test, see Fig. 4.4.2), and 1% noise to single-hit-signal ratio. The six bands represent the data from single hits and double hits with separation of $20\%l_a$, $40\%l_a$, $60\%l_a$, $80\%l_a$ and $100\%l_a$ respectively. Even though the data points have a much wider spread, it is still possible to identify double hits and estimate their separation for cases where $\delta x > 0.4l_a$. If the signal charge is collected by only three nodes, it is impossible to reconstruct the two hits precisely, because the number of unknown variables in this case is 4: two pulse heights, and two hit positions (the width of the distribution of each hit is a known quantity determined by the cell geometry). Additional information is needed in order to resolve the two hits. This usually can

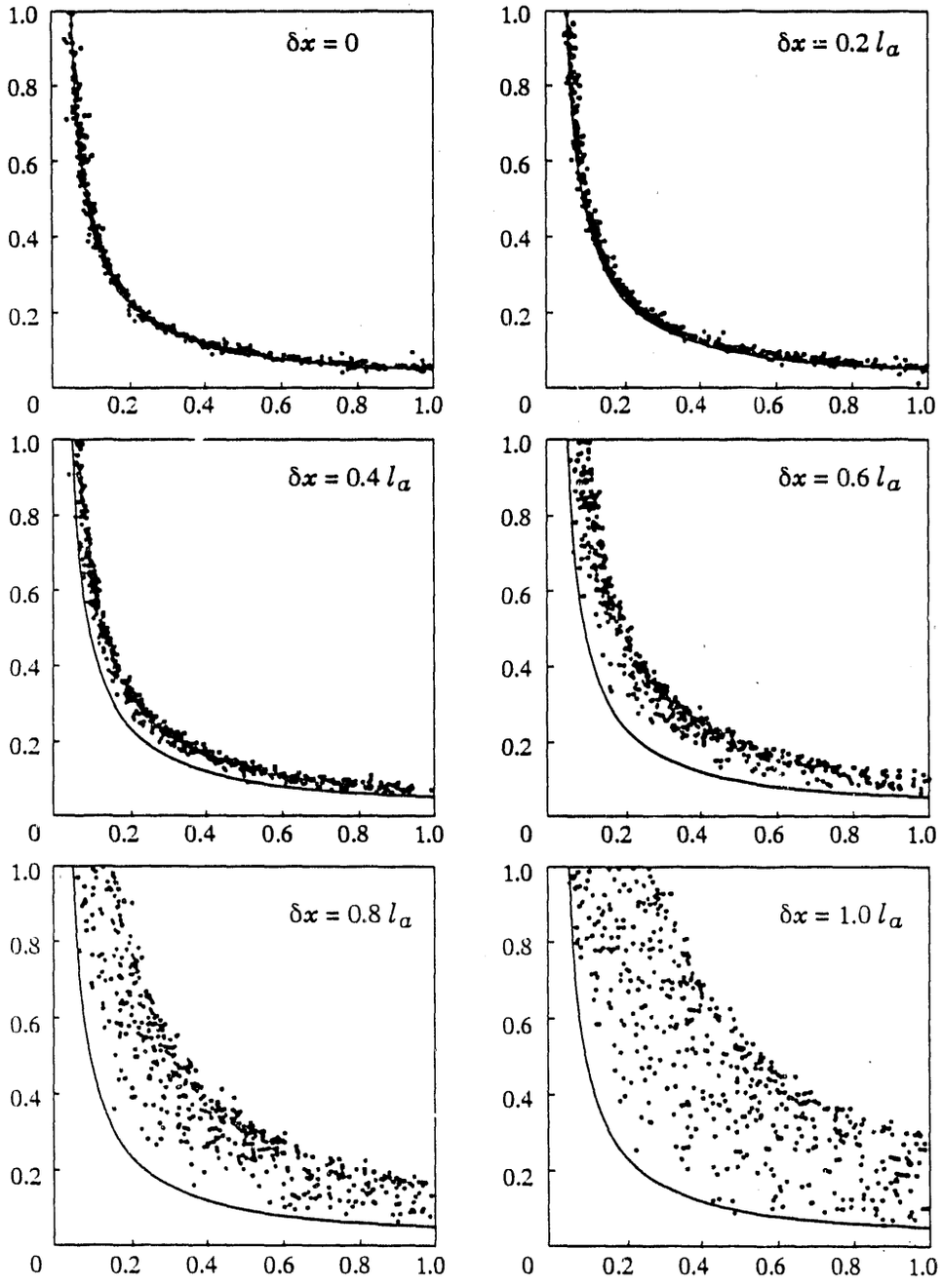

Figure 4.4.9: Charge ratio plots of events with double hits. Energy loss distribution is based on the full-size pad chamber with 15 GeV proton beam. Noise level of 1% of signal level is used.

be done by using information from other tracking detectors. For the cases where four or more adjacent nodes have signal, the two tracks can theoretically be reconstructed by using an appropriate algorithm to fit the data.

4.4.6 Position Linearity and Resistance Uniformity

For detectors with this type of resistive charge division, it is obvious that the position linearity is dominated by the uniformity of the resistance values of individual resistors between pads.

Fig. 4.4.10a is a plot of the measured resistance value and location of each individual resistor from a section of a pad chamber. The nominal value is about 10 kΩ. Their values have a long range non-uniformity. The short range differences are small, with one exception indicated by an arrow on the graph where one of the resistors has a value 70% higher than the rest. The dots in Fig. 4.4.10b are from a UIR spectrum measured in the same section of the chamber. The effect of the abnormal resistor is obvious. The solid line in Fig. 4.4.10b is the result of a computer simulation. The simulation was based on the information of the measured resistance values and the cell geometry of the chamber. The simulated result closely resembles the experimental results. From the same simulation, the position error caused by the resistor was calculated. Fig. 4.4.10c shows the reconstructed position error along the length of the chamber. The position error caused by this large resistor deviation is about 500 μm.

In principle one can use the measured values of the resistors to simulate the response of the detector, and therefore maintain a database to correct the experimental data. For a small detector, a high degree of linearity can be achieved by using some correction. However, it may not be practical or feasible to measure every resistor on a large detector (there are 5000–7000 resistors on our chambers).

Clearly, a better way of improving linearity is to control the resistance values within a tolerable range. Some results from computer simulations are shown in Fig. 4.4.11 through Fig. 4.4.13. The simulation shows that a $\pm$10% variation in resistance values will result in a $\pm$100 μm position error (with l_a = 6 mm). The precision of silk screening resistors is no better than $\pm$10%. The possibility of trimming the

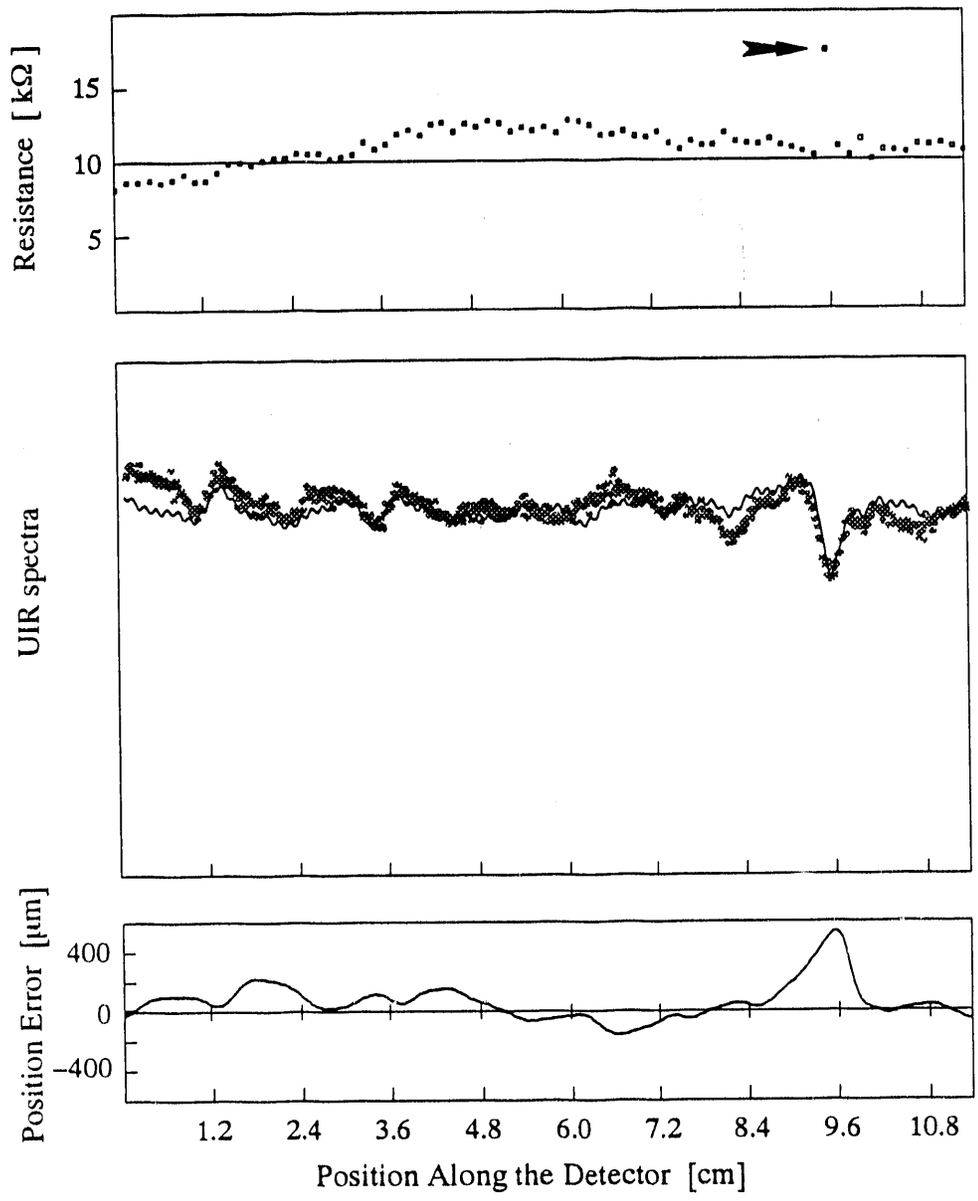

Figure 4.4.10: Effect of a resistor with an incorrect value on the linearity of the detector (a) Resistance of the resistors in a section of the full-size chamber (b) Experimental x-ray UIR spectrum (dots) and simulated spectrum (line) (c) Simulated Position error

resistors has been investigated. One of the printed circuit boards for the full-size chamber was abrasively trimmed by a commercial facility. The non-uniformity was ±5%. This can be translated into a ±5% differential non-linearity across the whole detector. The position error is more sensitive to local non-uniformity (within readout node spacing) in resistance value rather than to global non-uniformity.

The simulation results indicate that the linearity of the system is directly related to the variation of resistance values. It also depends on the location of the abnormal resistors. The local uniformity of the resistance value is more crucial than the global uniformity.

4.4.7 Charge Sharing Across the Wire Direction

Due to the relatively large spread of the induced charge on the cathode plane, some charge is shared by the pads under the two neighboring anode wires. As described in Chapter 2, the induced charge distribution across the anode direction is not necessarily symmetrical with respect to the anode wire. Due to the effect of the avalanche angular localization, particles or photons striking at positions some distance away from the anode wire will induce charge with centers of gravity towards the side of wire where the particle or photon passes. This is a small but measurable effect, especially if the charge collection time of the electronics is long.

To study the charge sharing from one pad row to its neighbor, a collimated 15 μm wide beam of x-rays was used to scan the chamber from one cell boundary to the next at a fixed position along the x axis. The beam was placed over a readout node. The signal from the main anode wire and its neighbor were recorded as well as signals from the three pads directly underneath the main anode, and those from two more pads on the rows directly above and below.

Fig. 4.4.14a shows the ratios of charge shared to the next pad row as a function of the y position of the x-ray beam. The pad row associated with the anode wire below the main wire receives an average 1.5 to 2% of the charge and the pad row associated with the anode wire above barely receives 1% of the charge. The asymmetry can be explained by the main wire's not being placed exactly in the center of the pad row.

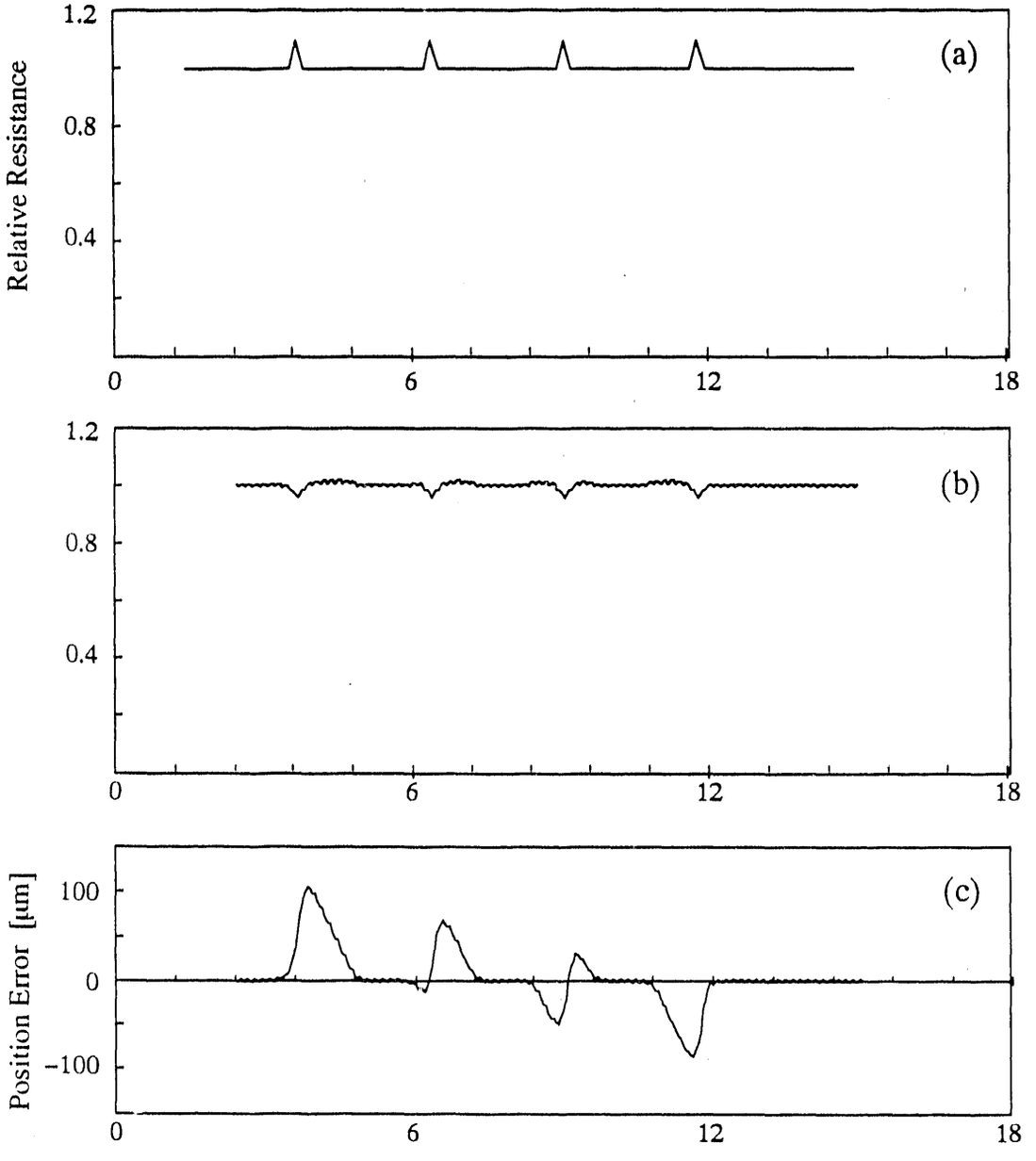

Figure 4.4.11: Computer simulated results for a resistive pad chamber. $l_a = 12\,\text{mm}$. There are 8 pads per readout. $h = 2\,\text{mm}$. (a) Resistive values of the resistors as a function of their locations. Single resistor with 110% of the nominal value is positioned at various locations with respect to the readout node. The readout node positions are indicated by the tick marks. (b) Uniform irradiation response of the system with the above resistive values. (c) Reconstructed position error as a function of the true position.

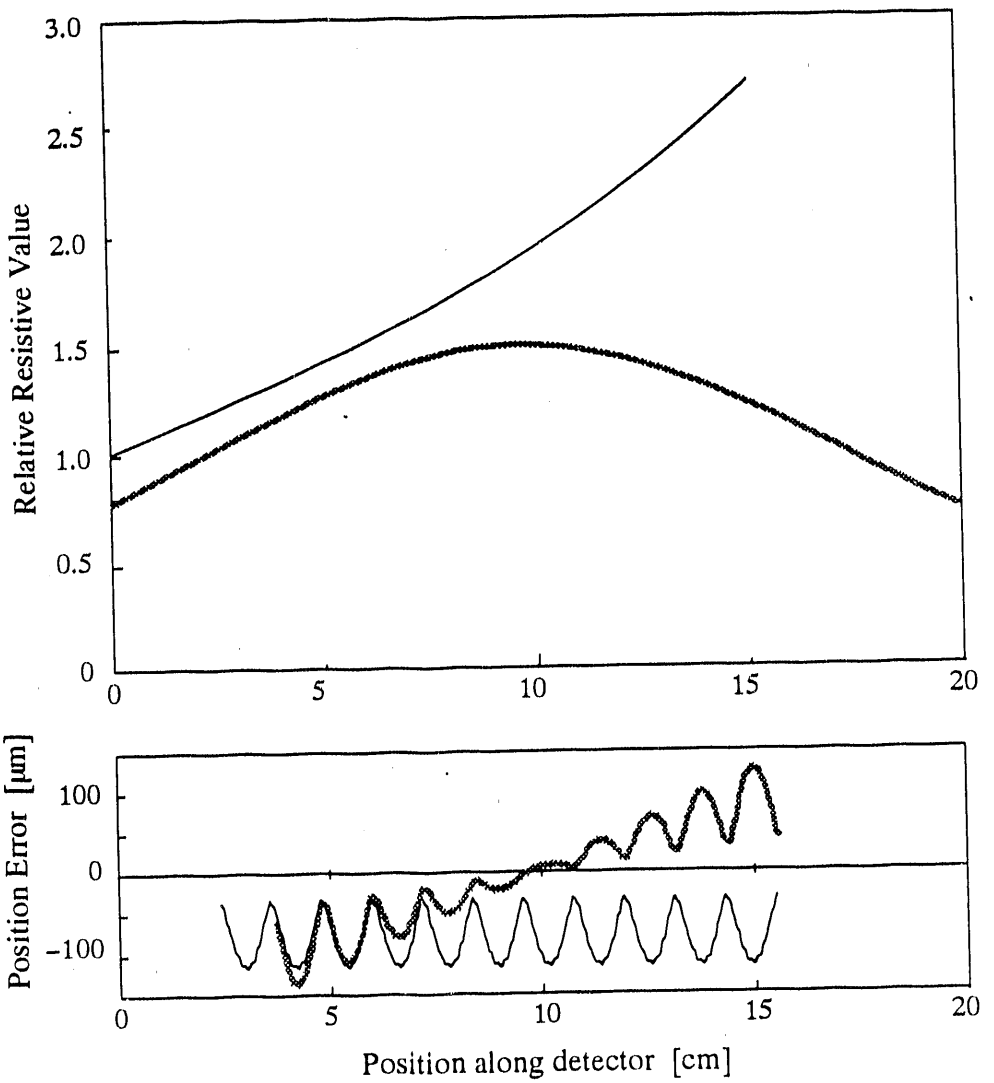

Figure 4.4.12: Effect of global changes in resistance. The detector parameters are the same as the previous plot ($l_a = 12\,\text{mm}$). (a) Resistive values of the resistors as a function of their locations. In one case, every resistor is 1% higher than its neighbor to its left (black line). In another case, the resistance for each resistor follows a sinusoidal form, with an amplitude of ±50% (shown in shaded line). (b) Reconstructed position error as a function of the true position. The absolute position error in this case is about the same as that of a 10% change of a single resistor.

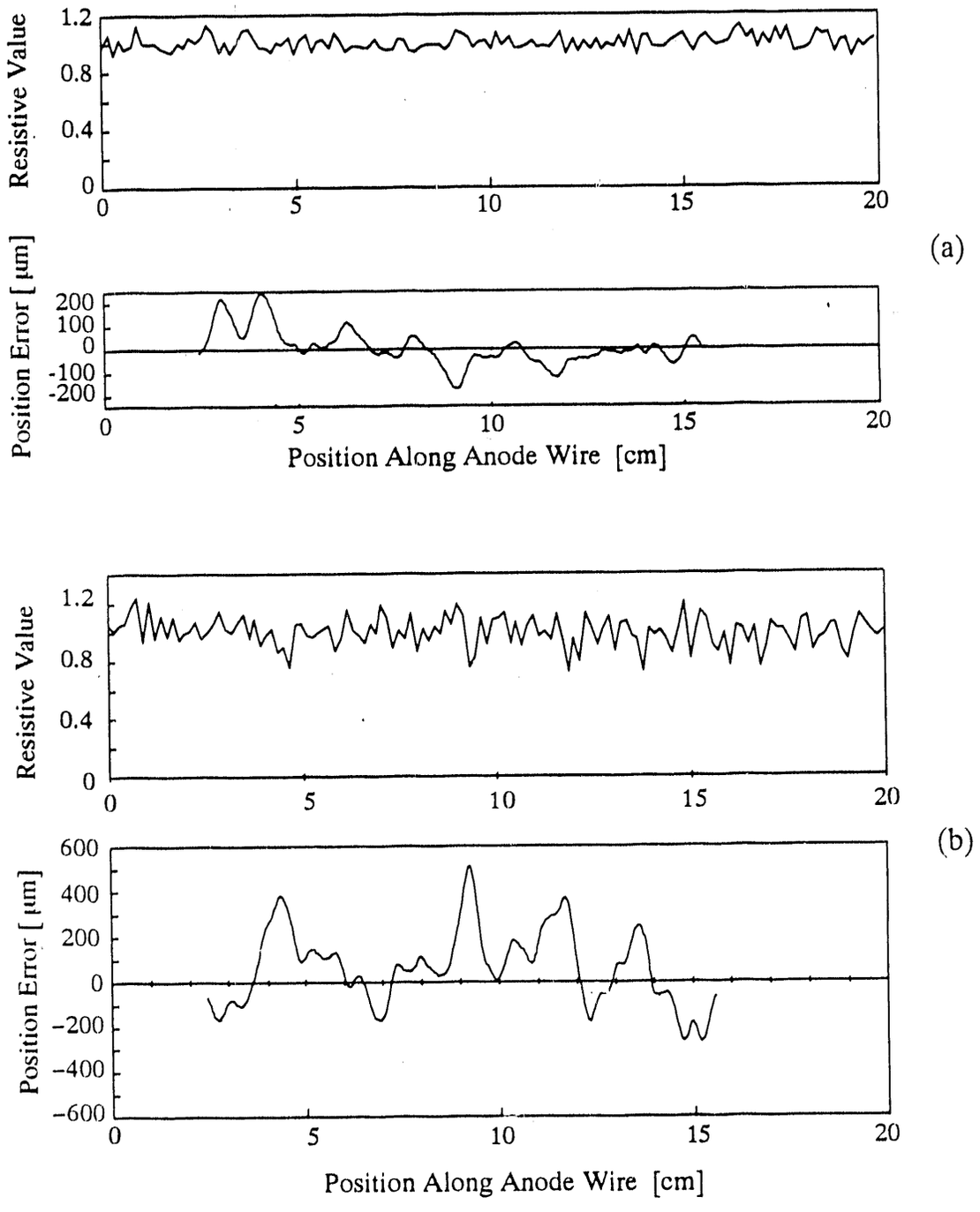

Figure 4.4.13: Another example of the effect of a set of randomly distributed resistors. All the parameters are the same as the previous plot (l_a=12 mm). (a) A set of resistors whose distribution of the resistance value follows a gaussian with a σ 5% of its mean. The reconstructed position error as a function of the true position is also shown. (b) Resistors with 10% rms errors.

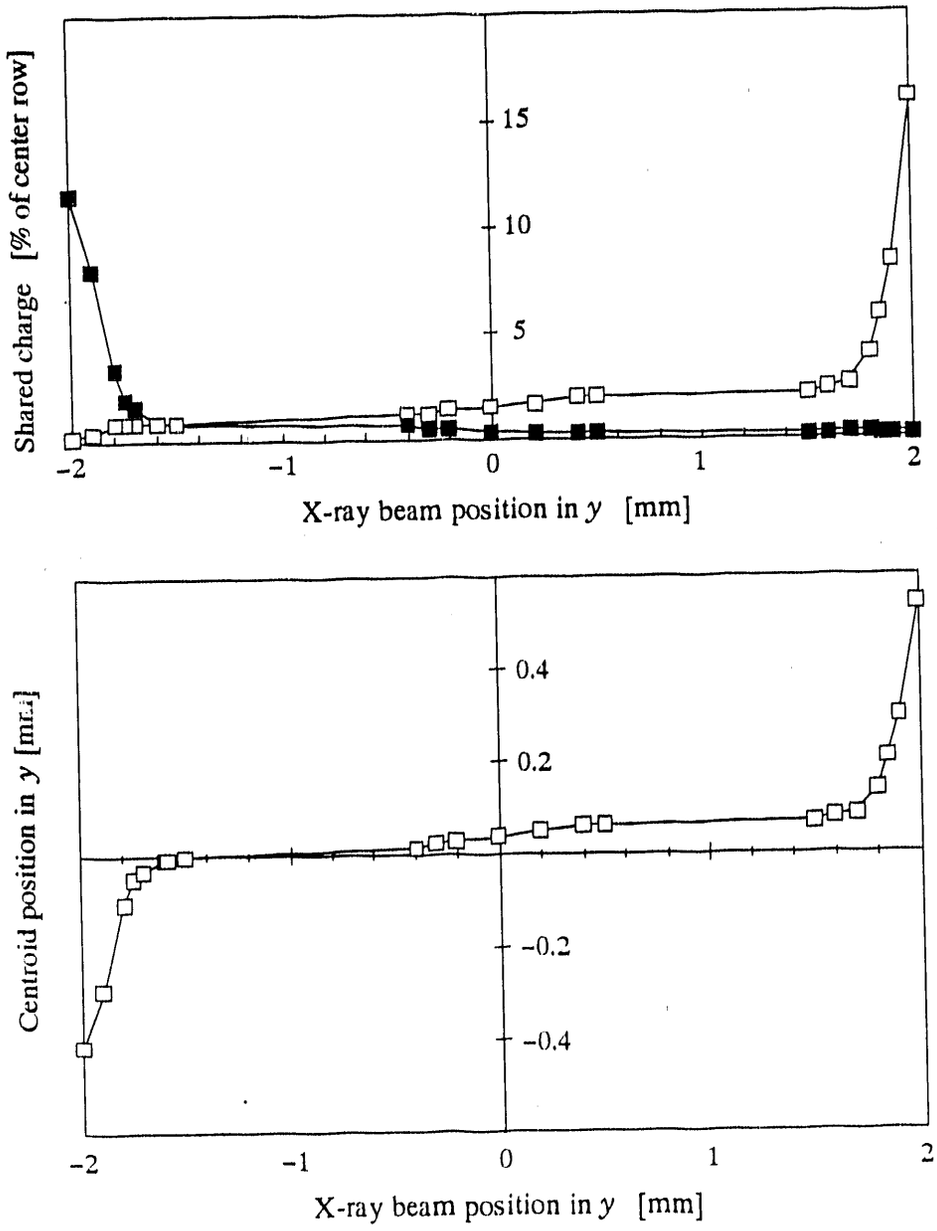

Figure 4.4.14: (a) Ratios of the amount of signal collected by neighboring pad rows to the primary pad row as a function of the x-ray beam position in y direction. (b) Centroid shift in y direction as a function of the x-ray position in y. Data was based on the results above.

Fig. 4.4.14b shows the centroid of signals in the y direction as a function of the y coordinate of the x-ray beam.

For systems with a longer shaping time, the centroid position will have a larger swing across the anode wire, since position ions produced in the avalanche will move farther from the anode wire. This information can be used to improve the position resolution of the detector in the direction across the anode wires. Applications using similar principles have been used in MWPCs and drift chambers to improve position resolution and to aid in resolving left-right ambiguities [47–48].

4.4.8 Effect of Non-uniform Electronics Gain

One advantage of this resistive charge division readout is that it is relatively insensitive to global non-uniformity of the electronics gain. Because each of the read-out nodes is well defined in position, it is in fact self-calibrating. As long as the electronics gain within the near neighboring nodes remains fairly equal, the reconstructed position will not suffer large deviation. Of cause, one should put every effort to ensure the uniformity of the gas gain in order to maintain stable chamber operation against voltage breakdown as well as to maintain a high detection efficiency. One can also use the pulse height information as a measure of ionization if the gain is uniform.

To demonstrate the effect of electronics gain non-uniformity on the position accuracy of the system, results of some computer simulations are shown in Fig. 4.4.15. It can be clearly seen that the error in encoded position is determined by the difference in channel to channel gain, not by the absolute change in gain.

Variations in gas gain of the detector will not affect the position linearity. However, it may affect the position resolution due to the variation in the signal to noise level.

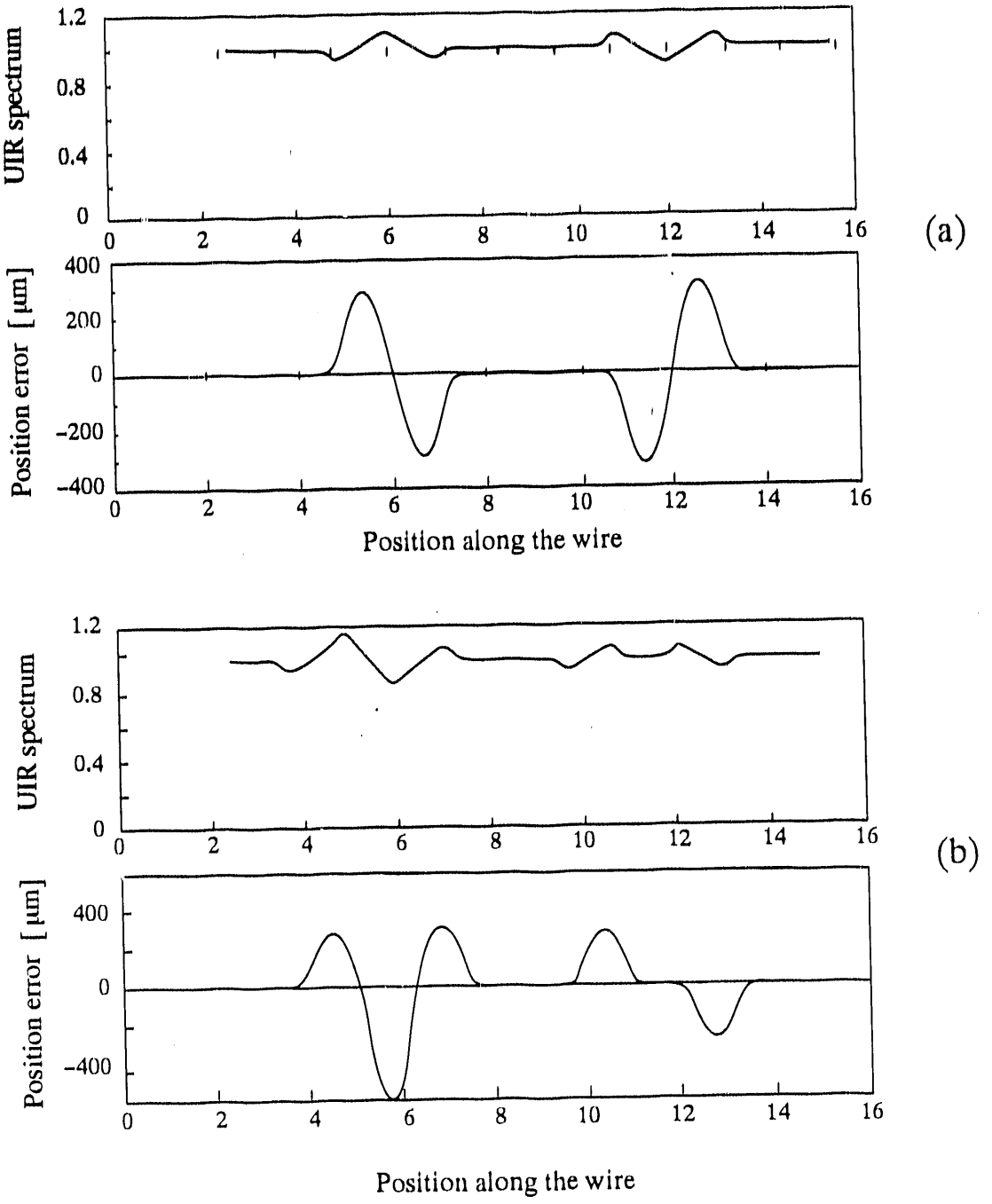

Figure 4.4.15: Local non-uniformity in electronics gain and the effect on linearity of the detector Both UIR spectrum and position error were simulated for each case. l_a=12 mm. (a) 10% variation in a single channel. The non-linear response on the left was result of a channel gain 10% higher. The one on the left was result of a 10% lower gain. (b) 10% variation in two adjacent channels. To the left, one channel has 10% higher and its neighbor 10% lower in gain. To the right two channels have 10% higher gain.

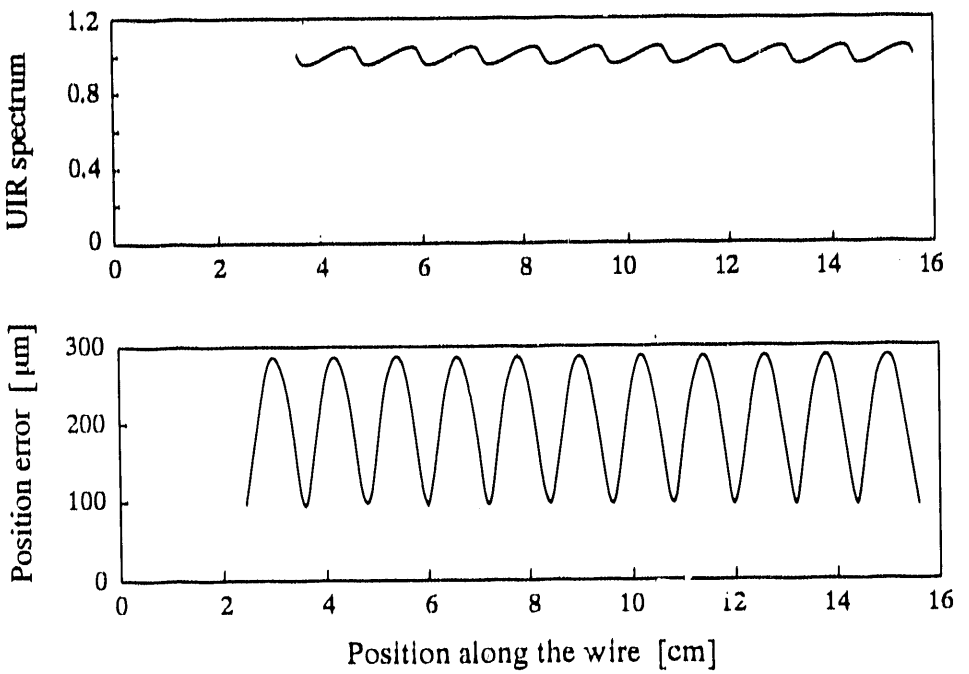

Figure 4.4.16: Global non-uniformity in electronics gain and the effect on the linearity. In this case, each channel is 10% higher in gain than its neighbor on the left. Note that the position deviation is less than that from a single channel with 10% variation. $l_a = 12\,\mathrm{mm}$.

Chapter 5.
Pad Chamber with Geometrical Charge Division

5.1. Introduction

Following the evolution of many geometrical charge division methods as described in Chapter 3, a new type of two dimensional pad readout system has been developed. It can be considered as a hybrid of the Zigzag Strip cathode [42] described in Chapter 3 and the resistive pad cathode described in Chapter 4.

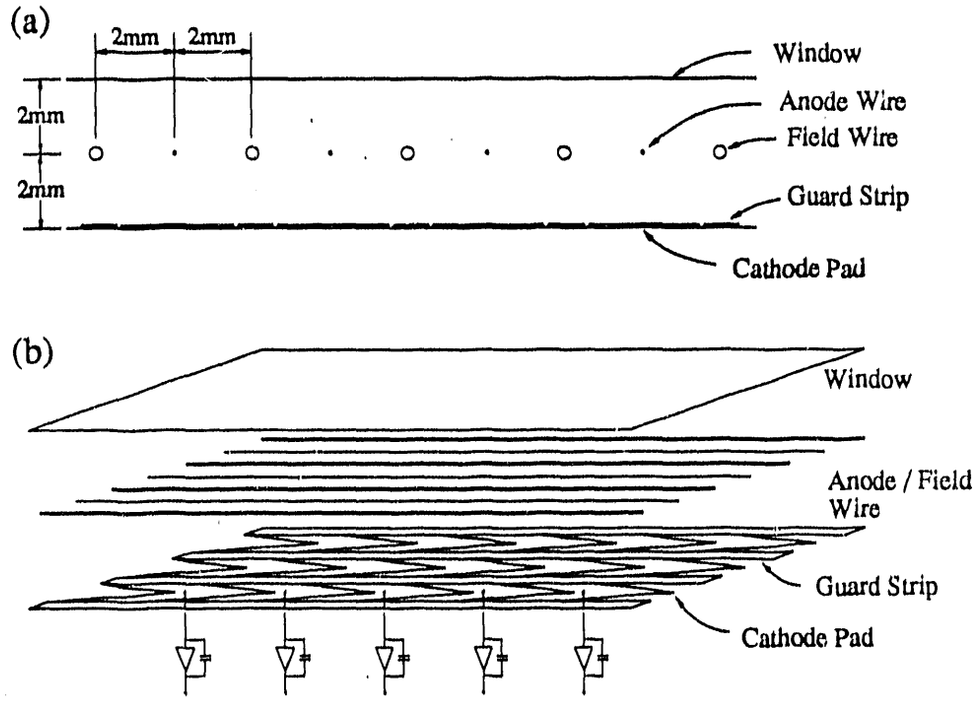

Figure 5.1.1: (a) Side view of the detector showing the cell structure (b) Exploded view (centered single chevrons used)

As shown in Fig. 5.1.1, replacing rows of rectangular pads and resistive strips, specially shaped cathode pads are used to perform charge division geometrically. Each of the pads is connected to a readout channel. The simplest and the first geometry used looks like a chevron, hence the name "Chevron Pad" was used for all these

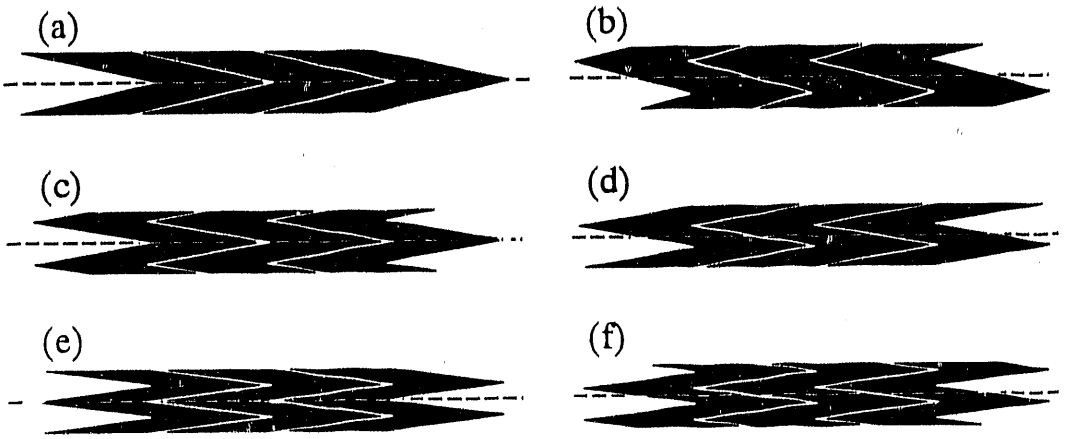

Figure 5.1.2: Patterns of (a) centered single chevron (b) displaced single chevron (c) centered one & a half chevron (d) displaced one & a half chevron (e) centered double chevron (f) displaced double chevron. Dashed line indicates anode wire position.

geometries. It should be pointed out that the chevron cathode has close relationship to the zigzag strip cathode, and they bear many functional similarities.

As the convention of this work, chevrons patterns are named by their "types," which refer to the number of the "chevron" periods in one pad. The simplest and the first pattern tested is called "single chevron" pattern, as shown in Fig. 5.1.2a, since each pad consists of one complete chevron. Subsequently, "one and a half chevron" (Fig. 5.1.2 c & d) and "double chevron" (Fig. 5.1.2 e & f) patterns were tested. The zigzag strip cathode [42] can be considered as a continuous chevron pattern.

Each type of chevron pattern, is further labeled with two "versions" based on the relative location of the zigzag apices with respect to the anode wire. In Fig. 5.1.2, (a), (c) and (e) are "centered" versions because the chevron patterns are symmetrical with respect to the anode wire, while (b), (d) and (f) are "displaced" versions because the anode wire is placed midway between two adjacent apices.

As in the case of the resistive pad chamber, we define the readout spacing, which is also the pitch of the pad along the x direction, to be l_a. The depth of the chevron pattern is then defined to be $f_x l_a$, where f_x is a form factor defining the amount of overlap of the chevron tips. The f_x factor is explained in Fig. 5.1.3, which illustrates the effect of different f_x values on the double chevron pattern. A quantity w, used in some computer simulations, is defined as the width of one complete chevron

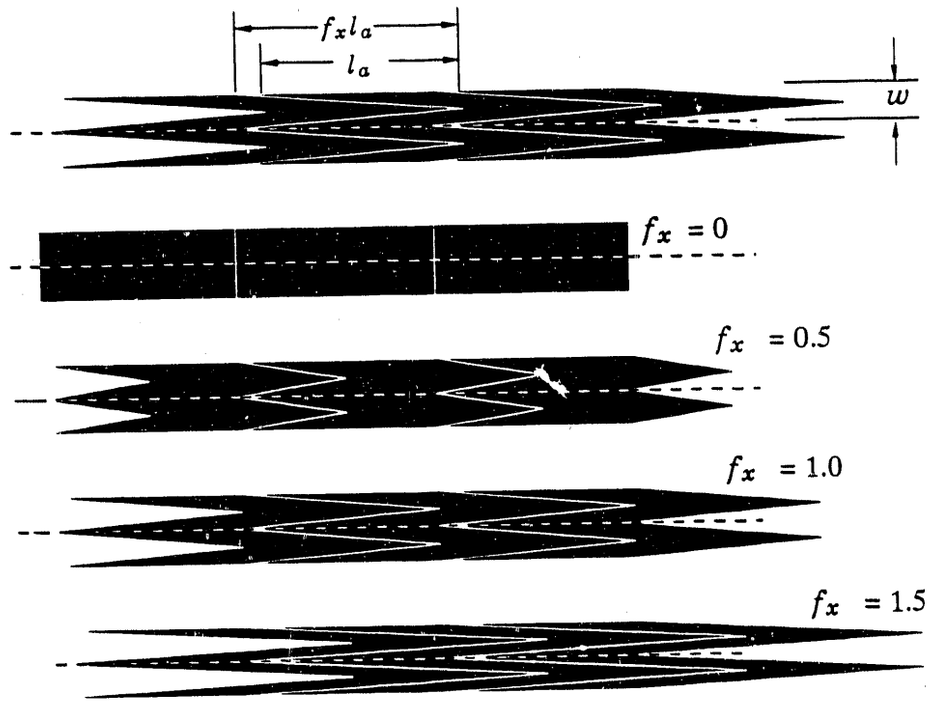

Figure 5.1.3: Examples of double chevron pattern with different f_x values. Note that l_a and w are the same for all cases.

(zigzag) pattern, see Fig. 5.1.3. Note that w is not necessarily the physical width of the chevron pad.

5.2. Previous Work

The first study on the property of chevron shaped cathode pads was performed by Chase [49] with a scaled up model (40 to 1) of a chamber. The measurement of the charge sharing was simulated by capacitance measurements.

The test setup is shown in Fig. 5.2.1a. The chevron cathode is placed over a ground plane, separated by G-10 sheet with various thicknesses. A stainless steel tube (representing the anode wire) is placed 8 cm above the cathode plane. A 4 mm band, wrapped around the tube, is connected by a coaxial cable to a capacitance bridge to simulate the anode charge. Another ground plane is placed 16 cm over the chevron plane. Three chevron electrodes can be connected to the bridge sequentially. Capacitance values were measured between each chevron pad to the "signal source"

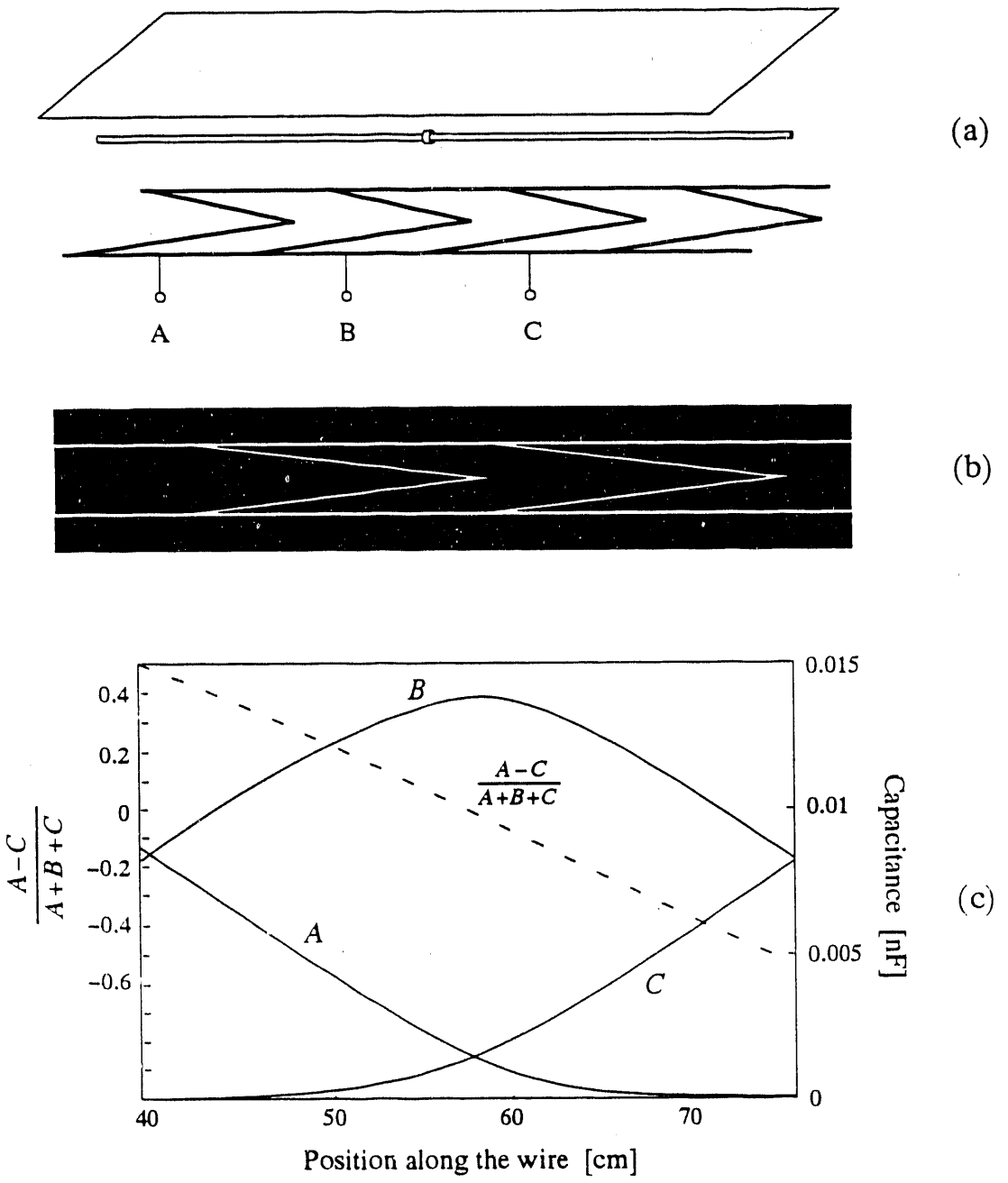

Figure 5.2.1: Scaled up simulation of the first chevron cathode by Chase [49]. (a) Test setup, (b) A section of one chevron cathode, (c) Capacitance measurements and the calculated centroid.

at different locations. Fig. 5.2.1c shows the relationship between the capacitance values from chevron pad A, B and C. The dashed line shows the computed values of $\frac{A-C}{A+B+C}$, which is a measure of the source position.

Three chevron planes were tested with the following parameters: chevron gap 40 μm, guard gap 40 μm; chevron gap 125 μm, guard gap 125 μm; chevron gap 125 μm, guard gap 500 μm. The expression $\frac{A-C}{A+B+C}$ was evaluated for each position of the "signal source" and fitted to a straight line using the Least Squares method. Table 5.2.1 summarizes the results.

Table 5.2.1: Some results of the scaled-up simulation

Chevron Gap	Guard Gap	G10 Thickness	σ_N	Max. Deviation from Straight Line
40 μm	40 μm	40 μm	0.0112	2.0%
125 μm	125 μm	40 μm	0.0086	1.0%
125 μm	500 μm	40 μm	0.0135	2.0%
125 μm	500 μm	200 μm	0.0162	2.5%

5.3. Detector Performance

5.3.1 Apparatus

A small test detector, whose basic dimensions were based on the resistive pad chambers described in the previous chapter, has been constructed for investigation of the performance of various chevron geometries. Details about its construction are described in chapter 6. Some of the highlights are given here.

The cell geometry is the same as in the prototype resistive pad chamber. The anode–cathode spacing h is 2 mm, and anode wire spacing is 4 mm, (diameter 18 μm). There are field wires (diameter 125 μm), also with spacing of 4 mm, between anode wires. The window, or upper cathode, is 25 μm thick aluminized mylar.

The cathode pad plane is made from a three-layer printed circuit board. The first layer is the cathode pads, the third is the leads connecting the cathode pads via plated-through holes. A ground plane lies in between these two layers to isolate

the readout leads from the cathode pads, thereby reducing the cross-talk between a chevron pad and the leads running underneath. The width of the pads is 3.05 mm, which is approximately 3/4 of the anode-anode pitch. Each cathode board contains three active pad rows. Typically, each row of chevron pads has a different f_x value. The design of the test detector assures that the cathode board can be easily replaced by another with different chevron patterns. Nearly 30 of the readout boards with various readout patterns have been fabricated and tested.

Each row of cathode pads is separated from its neighboring row by a guard strip of width 0.95 mm, whose main purpose is to reduce the amount of charge induced on the neighboring row. The presence of the guard strip is not crucial to the operation of the chamber.

Two types of readout electronics were used for the testing, (see Fig. 5.3.1):

i. Each pad in one row is connected to a charge sensitive preamplifier and shaping amplifier; a centroid is then determined by the analog centroid finding electronic system, as was used in the tests of the resistive pad chamber [19]. Most of the measurements were carried out with this configuration,in which signal shaping times of 1.4 μsec and 500 nsec were used.

ii. Each pad in one row is connected to a delay line whose signal timing characteristics allow an accurate center of gravity of the anode avalanche to be determined [26]. This configuration allowed us to reduce the signal shaping time to 100 nsec.

5.3.2 Position Resolution

The cathode board is fabricated on a three layer printed circuit board 0.75 mm thick. The pads themselves are on the first layer The middle layer is a continuous ground plane to minimize coupling between readout lines and the chevron pads. Each pad, therefore, has quite a large capacitance to ground, of order 20 pF. In spite of this, using the centroid finding electronics [19], with a spacing of only 12 mm between readout nodes, minimum position resolution is not limited by electronic noise.

Position resolution was measured by using a pencil beam of 5.4 keV x-rays. It is shown as a function of anode charge in Fig. 5.3.2. All the chevron patterns

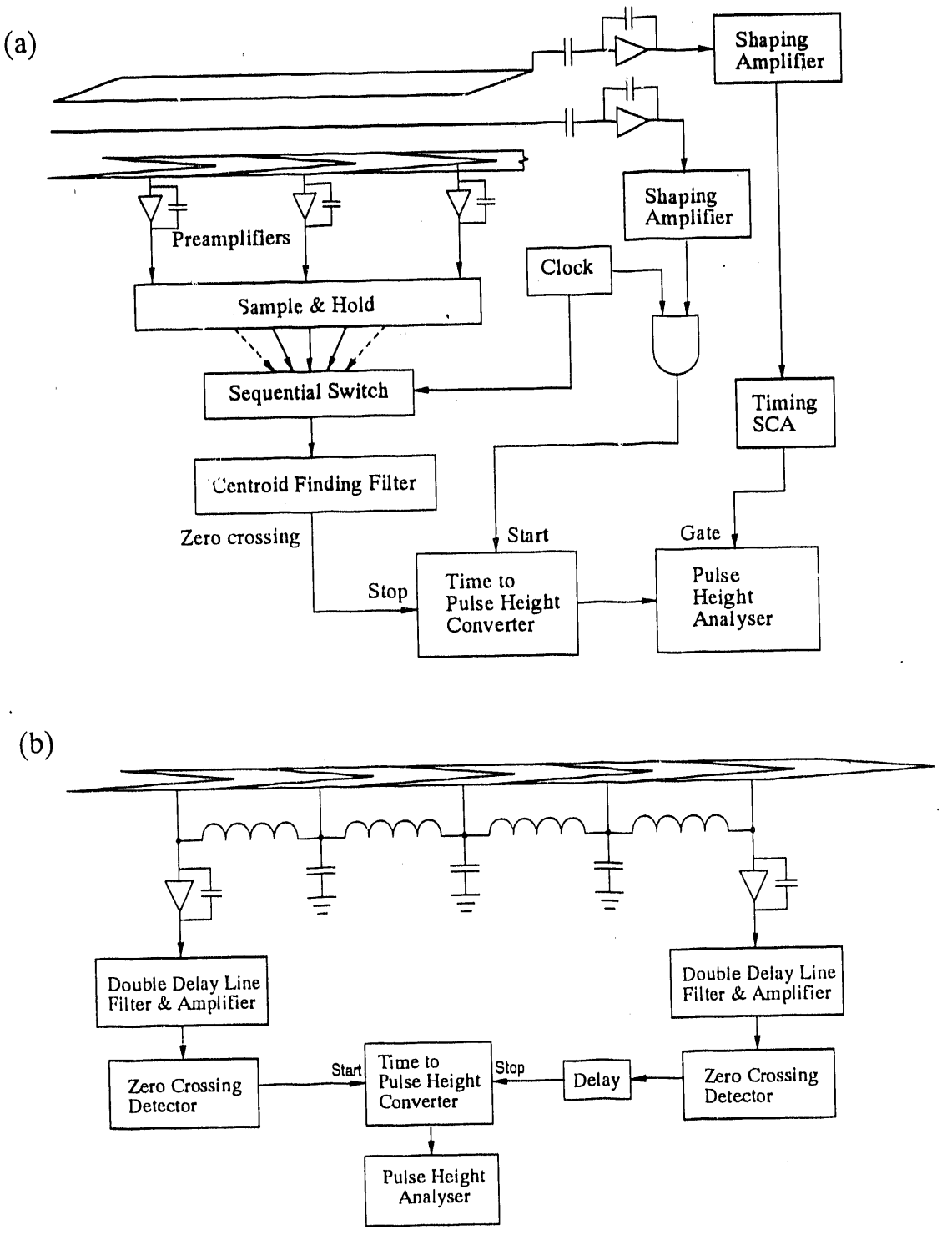

Figure 5.3.1: Schematic diagrams of the electronic readout systems used for the chevron test. (a) Centroid finding system (b) Delay line system

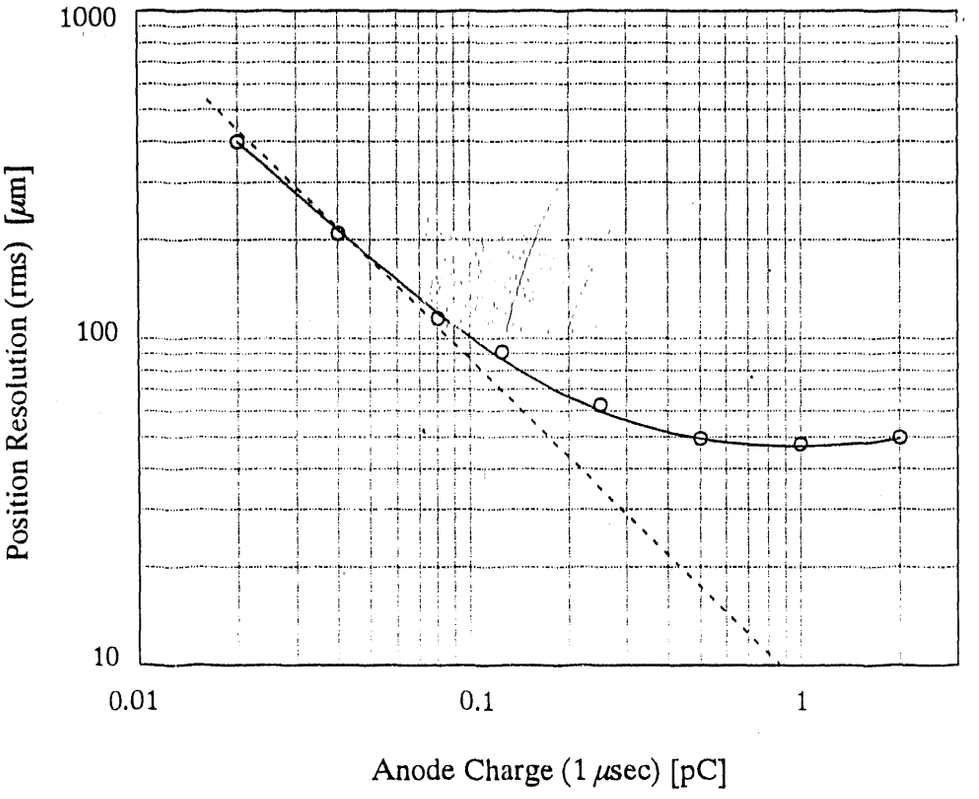

Figure 5.3.2: Position resolution vs anode charge. Results were measured from a 12 mm single chevron cathode. using centroid finding electronics

exhibit similar position resolution characteristics. At low anode charge, less than about 0.08 pC, the resolution is electronic noise limited, but at higher charge levels it gradually reaches a plateau level of about 110 μm (FWHM), which is consistent with the limit of resolution due to photoelectron and Auger electron range [28]. Compared with the resistive pad chambers described in the previous chapter, these chevron pad chambers have a better position resolution, due to their lack of resistors as noise sources.

Another phenomenon affecting position resolution is the avalanche angular localization. It is discussed in detail below.

5.3.3 Position Linearity

Nearly exact calculations of non-linearity can be carried out using the single parameter empirical distribution of cathode charge [15,17]. It was found that a

gaussian distribution, whose FWHM is adjusted to give a best fit to the calculations using the empirical distribution, yielded results which were very close to those from the correct distribution, and were easier to compute [50]. Thus, all the computer simulations included in this chapter have been calculated with the best fit gaussian induced charge distribution. The following simulation assumes there were no gaps between adjacent chevron pads.

The continuous lines in Figs. 5.3.3(a)–(f) show the predicted behavior of differential non-linearity (DFNL), as a function of f_x, for the six chevron patterns illustrated in Fig. 5.1.2. There is a trend common to all six curves, namely that DFNL has a minimum at, or very close to, $f_x = 1.0$. Displaced versions of a particular chevron type always yield a better DFNL than the centered counterpart. This advantage is especially significant for the single, and one & a half chevron types. However, the effects of avalanche angular localization, which are discussed below, can cause undesirable effects which are more significant for the displaced chevron than for the centered chevron. Therefore the choice of a particular chevron pattern should not be based on DFNL alone. As one might expect, the performance of zigzag cathodes [42] also showed that minimum DFNL was attained when the anode wires passed between the apices of the pattern.

Experimental measurements of DFNL have been performed by uniformly irradiating the test chamber with a broad beam of x-rays. The resulting uniform irradiation response was obtained by analyzing signals from the position encoding electronics with a pulse height analyzer. Values of experimental DFNL are shown as the hollow circles in Fig. 5.3.3. There is, in general, quite a good agreement between prediction and measurement, save for the fact that the curve through the measurements is displaced by about $f_x = +0.05$ in the abscissa, relative to the predictions. This discrepancy is indicated in Fig. 5.3.3 with the dotted lines for each set of measurements. The dotted lines were drawn with a displacement of $f_x = -0.05$. A similar phenomenon was also observed with zigzag cathodes [42].

The shift in the optimum f_x values for each geometry is believed to be caused primarily by the finite gap between the chevron pads. Fig. 5.3.4(a) illustrates this point by magnifying the part of the design artwork for the displaced one & a half

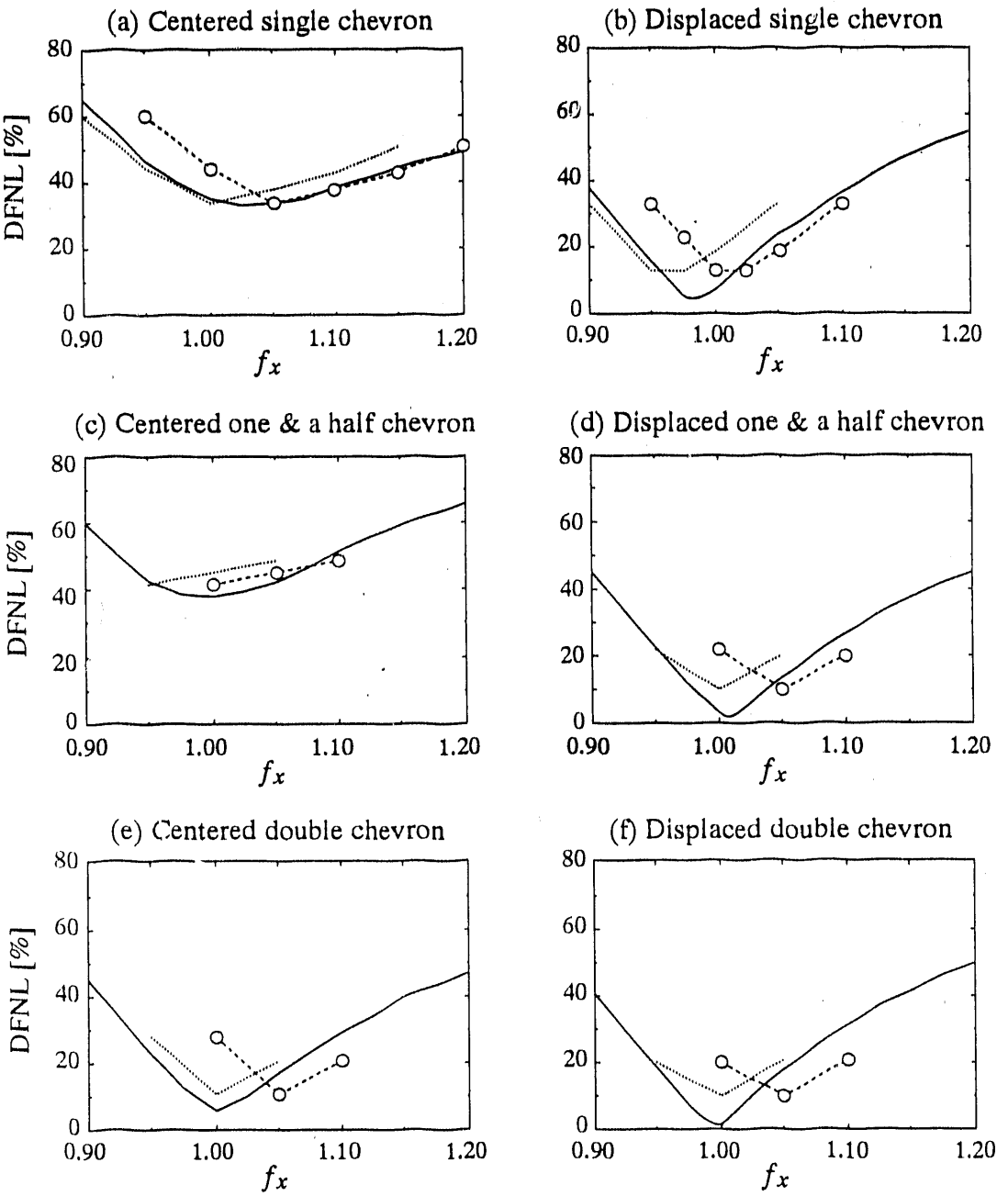

Figure 5.3.3: Differential non-linearity (DFNL) versus f_x for (a) centered single chevron (b) displaced single chevron (c) centered one & a half chevron (d) displaced one & a half chevron (e) centered double chevron (f) displaced double chevron. The continuous lines in Figs. 5.3.3(a)–(f) show the predicted behavior of differential non-linearity. The dashed lines with circles are experimental measurements. The dotted lines are the experimental results shifted by $f_x = -0.05$.

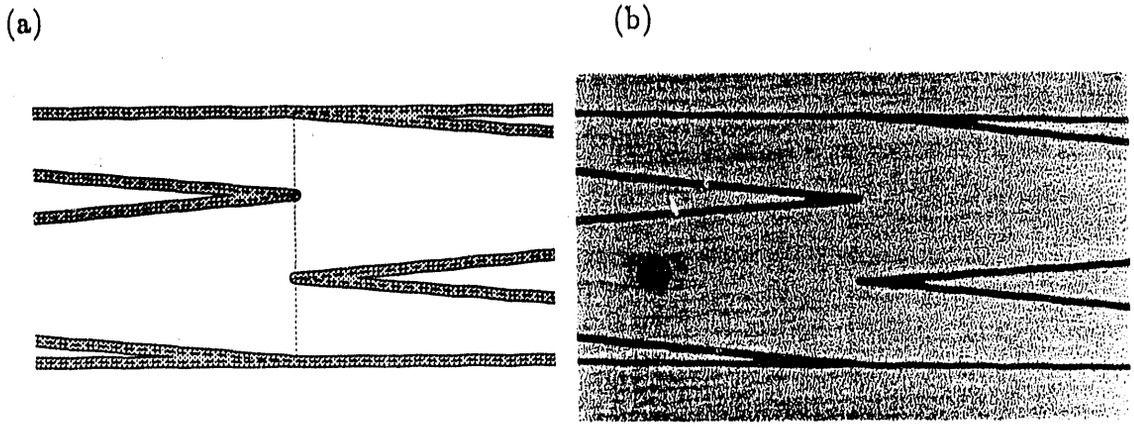

Figure 5.3.4: Enlarged view of chevron apices on displaced one & a half chevron pattern, $f_x = 1.0$. (a) Design drawing, the gap width is exaggerated. (b) Photograph of same area of actual cathode (black circle is a plated-through hole).

chevron. The dashed lines represent the assumed boundaries between adjacent pads on which the theoretical prediction was based, and the shaded area is the part that is assumed to be etched away. As shown by the vertical dotted line, the chevron apices and bases should all be in line for this configuration with $f_x = 1.0$, but the etched gap pulls the apices away from each other. Fig. 5.3.4(b) shows a photograph of the same area of the actual cathode; with our best print and etch techniques we can presently achieve, with uniformity and reliability, a gap of about 60 μm. For this particular cathode, the apices of the chevrons are separated, in the axis of the anode wire, by about 1.5 mm, or 12% of the pad spacing l_a. It appears that a value of 0.88 for the f_x would be more accurate. However, the experimental results show that the DFNL of this chevron pattern lies in the vicinity of 0.95, which implies that a certain amount of charge which would have been induced on the area of the gap is shared by the two electrodes.

In comparing theory with experiment, the shape of the UIR is as important as the value of DFNL. Using the displaced one & a half chevron as an example, Fig. 5.3.5 illustrates the predicted and experimental UIRs for this pattern. Fig. 5.3.5(a) shows predicted UIRs for $f_x = 0.95$, 1.0 and 1.05, while Fig. 5.3.5(b) shows experimental UIRs for $f_x = 1.0$, 1.05 and 1.1. The offset of 0.05 in these comparisons is intentional, in order to further illustrate the effect described earlier in this section. It can be

clearly seen that there is good agreement between the shape of the predicted and experimental spectra.

The DFNL increases with the readout spacing l_a for a given geometry. The relationship is outlined in Fig. 5.3.6.

5.3.4 Gap Between Chevron Pads and f_x

Experimental results indicate that the DFNL increases with the gap width between chevron pads. In some preliminary tests we performed on single chevrons, the DFNL more than doubled when the gap width was increased by two. Test results also show that there exists an optimum value of f_x for a given geometry and a given gap width. The simulated results shown in Fig. 5.3.7 are attempts to evaluate quantitatively the relationship between the gap width and the f_x factor. A Gaussian was used for the cathode induced charge density. The simulation assumes that the charge is simply lost over the area sustained by the gap, and that there is no distortion in the partition of charge at the gap between adjacent pads. Please note that these results are based on a simplified model and there is little experimental information to verify it. From the limited experimental results obtained so far, it seems that the simulated optimum f_x is larger than the real optimum. The real optimum must lie between this simulation and the simulation without using the gaps.

Fig. 5.3.7 is a contour plot of the normalized rms position error as a function of the gap width g and the f_x factor for a zigzag cathode. The presence of a "valley" diagonally across the graph is obvious.

5.3.5 Avalanche Angular Localization

X-rays, unlike particle tracks, produce almost point-like deposits of primary ionization which, at low to moderate avalanche size, will create an anode avalanche which is localized to a small part of the anode wire circumference, depending along which field lines the primary ionization has drifted. In very simple terms, we can distinguish between four types of events. The first are due to x-rays which have been absorbed between the anode wire and the cathode pad plane, and the second to those absorbed between the anode wire and the window; these are referred to as "pad-side"

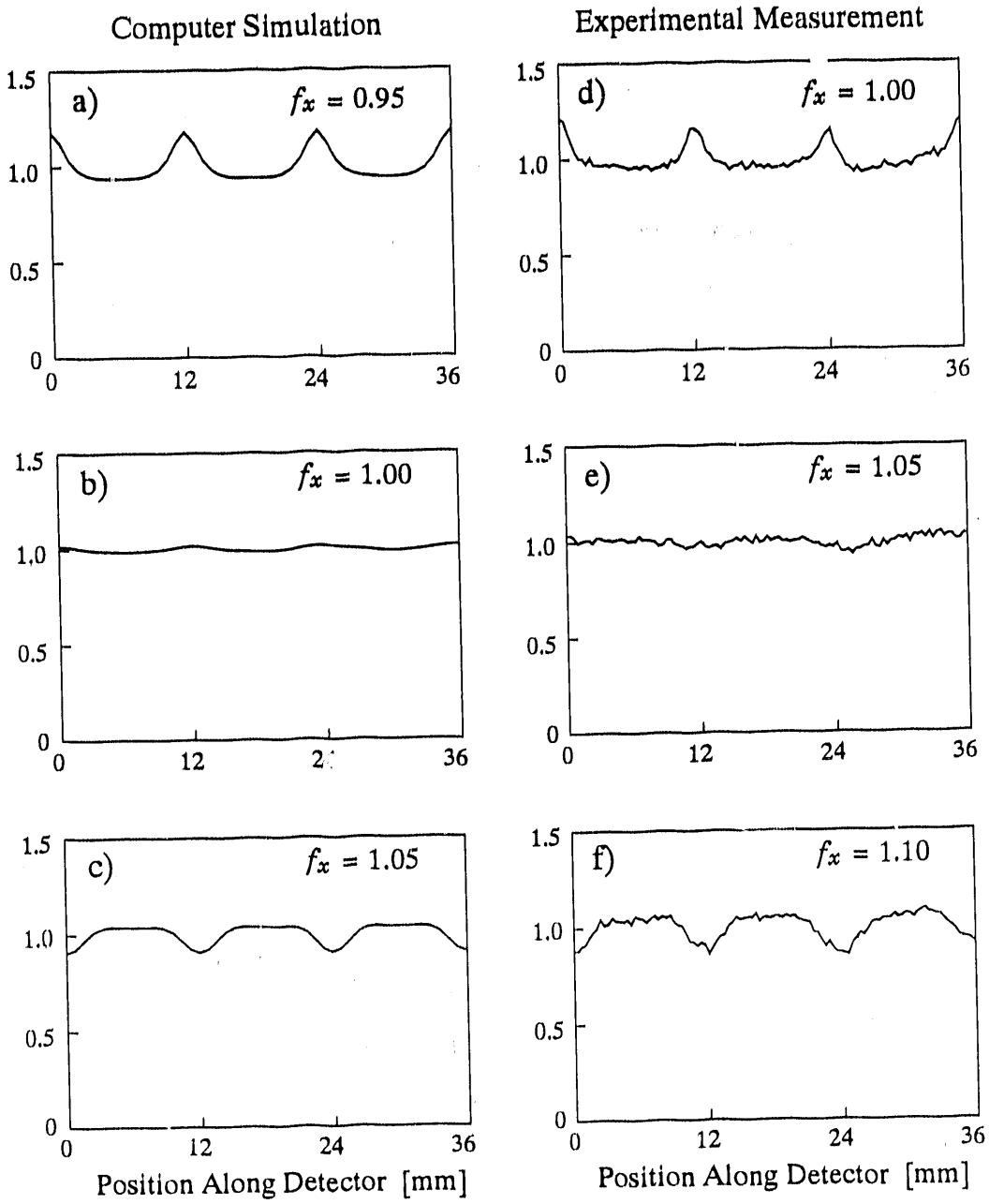

Figure 5.3.5: Uniform irradiation response of the displaced one & a half chevron pattern. (a)-(c) are theoretical predictions, (d)-(f) are experimental results.

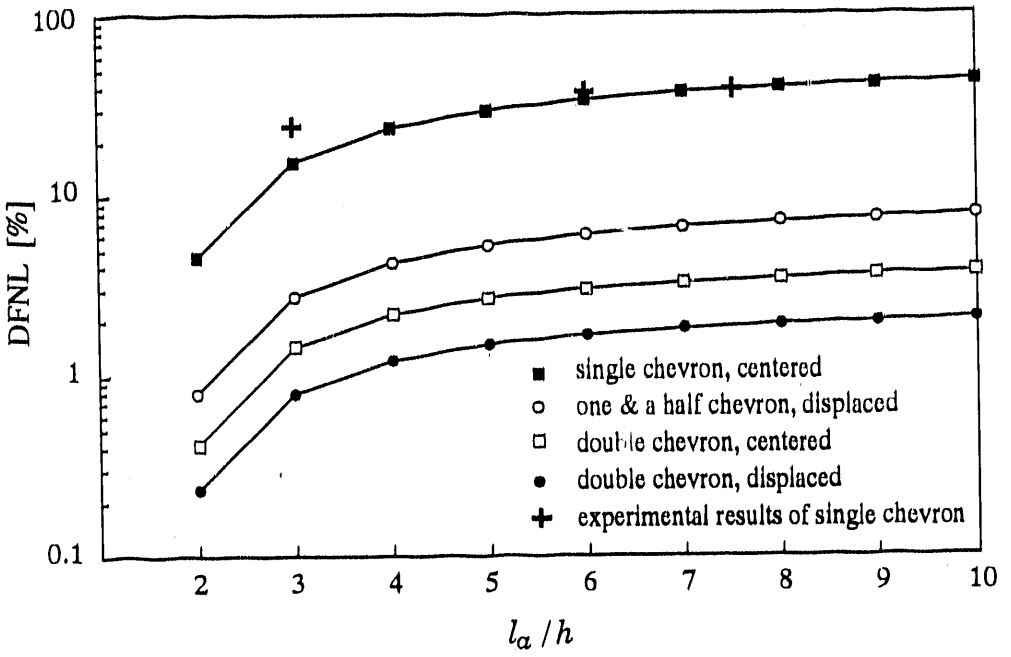

Figure 5.3.6: Computer simulated DFNL as a function of l_a for four different chevron geometries. The anode-cathode spacing h is normalized to unity. The widths of the chevron pads are $1.5h$ as in the test detectors. $f_x = 1.0$ was used for all simulations. Experimental data were from single chevron patterns with $f_x = 1.1$.

and "window-side" events, respectively. The third are due to x-rays absorbed between the anode wire and its neighboring left side field wire, say, and the fourth are due to x-rays absorbed between the anode and its neighboring right side field wire (viewed along the anode wire direction with pad cathode at the bottom). All four types of event have their signatures in the position response of a chevron pad chamber.

A. Pad-side and Window-side Events

In contrast to resistive charge division systems, any position encoding scheme which relies upon geometric charge division will have an increase in non-linearity of the encoded position as the footprint of sampled charge becomes smaller. In particular, x-ray pad-side events have a narrower induced charge distribution than the window-side events. This is because the majority of positive ions created by the avalanche of a pad-side event are moving towards the pads. The opposite is true for window-side events. As a consequence, window-side events are analyzed more linearly than

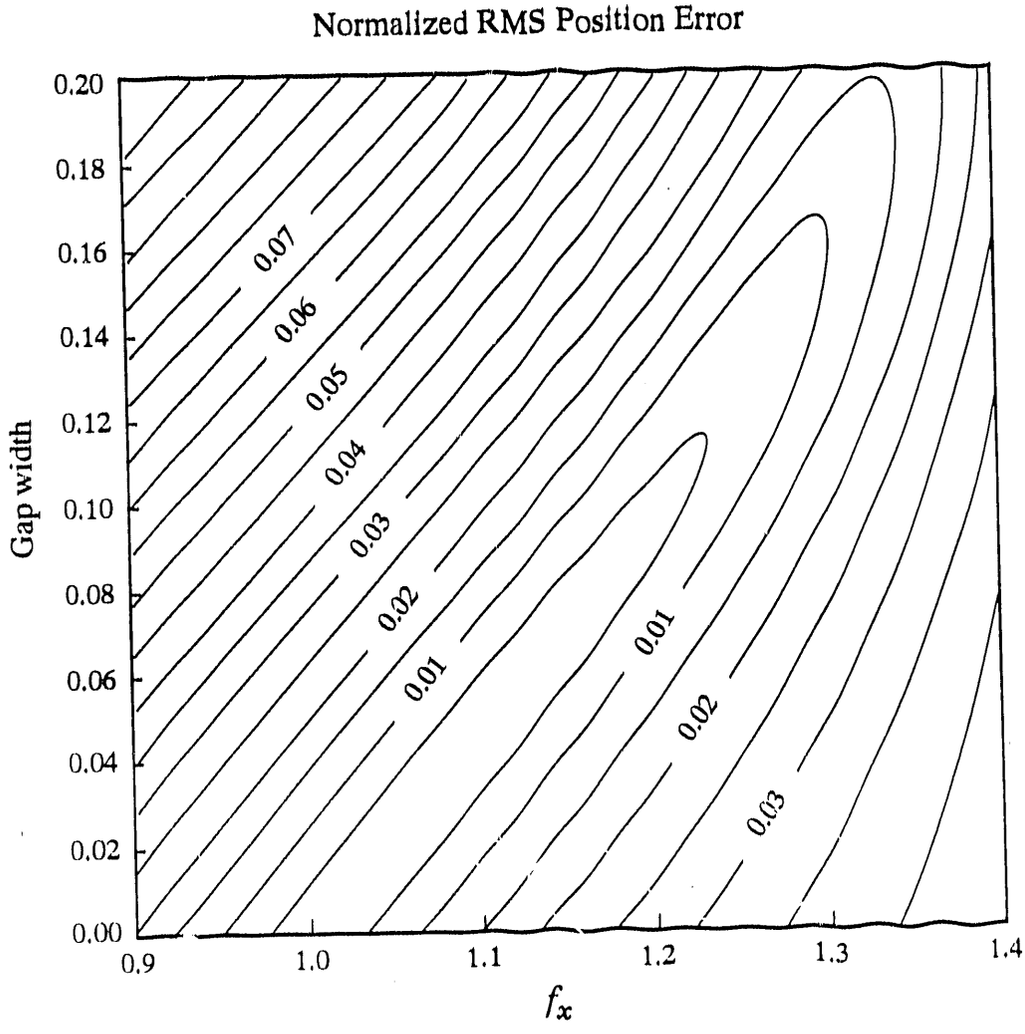

Figure 5.3.7: Contour plot of normalized rms position error as a function of gap width and f_x. Displaced one & a half chevron pattern is used. The anode-cathode spacing h is normalized to 1. $l_a = 5$, $w = 1$. The gap width is normalized with respect to h.

pad-side events, and this effect can cause a serious degradation in position resolution. Fig. 5.3.8 demonstrates the significance of this effect.

Certain characteristics of cathode signal shapes allow a determination to be made on which side of the anode plane an x-ray was absorbed [51–52]. The signal induced on the window, which is complementary to the signal on the cathode, has two distinct pulse heights for the two types of events. Window side events are about 50% larger for a 1 μs shaping time. In addition, if the window signal is fed to a shaping amplifier with a bipolar response, the zero crossing time of the two types of events are different—window-side events have a later zero crossing time. With a long shaping time, one can cleanly separate the two types of events by discriminating either the amplitude or the zero crossing time. This electronic selection technique was used to measure, separately, the position linearity of pad-side and window-side events.

Fig. 5.3.9 shows the absolute position error for the three chevron types used in this investigation, using the f_x values which gave minimum differential non-linearity. For the single chevron there is a maximum position error of about $\pm 600\,\mu$m but, perhaps more seriously, there is a separation in position between pad-side and window-side events which reaches a maximum of about $300\,\mu$m. For both the one & a half and double chevron patterns the maximum position error is less than $\pm 100\,\mu$m, and there is virtually no separation between two types of event.

Since the position resolution of a pad chamber is primarily determined by the signal to noise ratio, the larger signal size of pad side events gives a better position resolution. However, due to its smaller footprint in induced charge distribution, pad-side events generally exhibit larger differential non-linearity than window-side events.

B. Centroid shift due to avalanche angular localization

The "left side" and "right side" events cause the centroid of the induced charge distribution to shift in the y direction. The amount of shift depends on the shaping time of the readout electronics. Fig. 5.3.10 shows the y coordinates of the centroid of induced charge as a function of x-ray beam positions in y direction. The setup is the following: A displaced double chevron cathode with guard strips was used. Three adjacent pads in the middle of the detector were connected together as a single

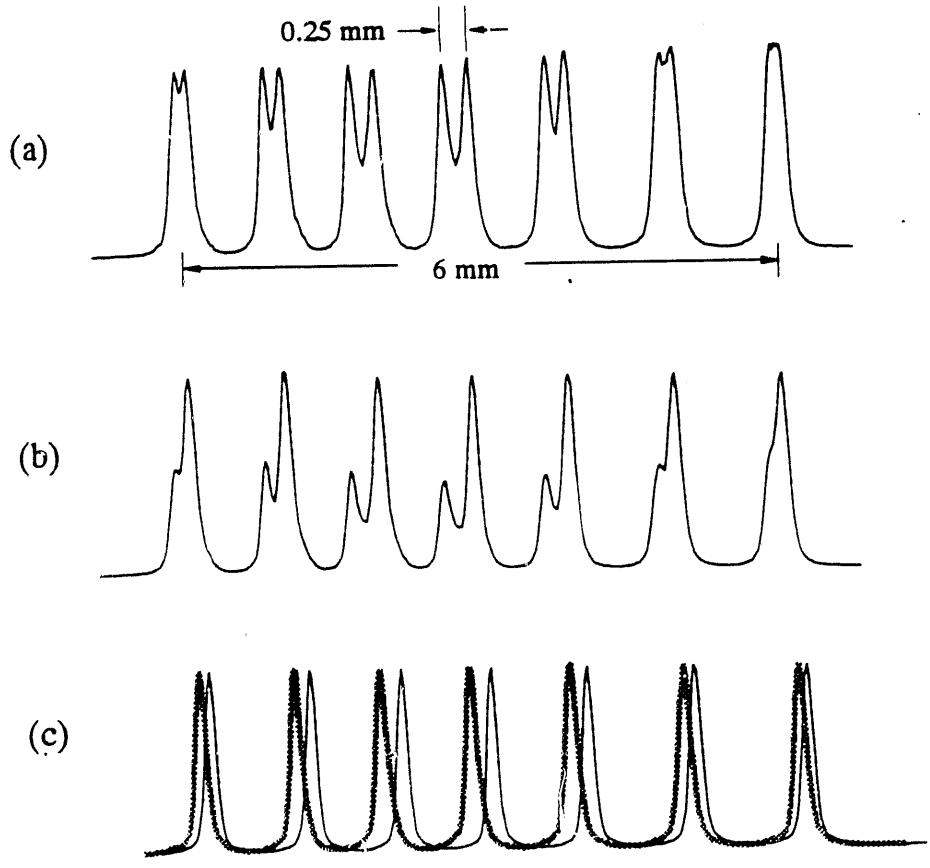

Figure 5.3.8: Effect of avalanche angular localization on the position response of a single chevron pattern (l_a=6 mm). Each of the three spectra is the reconstructed position distribution at several locations in the detector. A collimated x-ray beam was stepped at 1 mm intervals along the wire. The leftmost and the rightmost positions are "over a node", where one readout node receives the maximum charge and its two adjacent nodes receive equal and minimum amount of charge. The readout spacing in this case was 6 mm. (a) Results of the chamber with symmetrical cell, i.e. 2 mm between anode and cathode pad plane as well as 2 mm between the window and anode wire plane. (b) Results of the chamber with asymmetrical cell, i.e. 4 mm between anode plane and window. Due to the 100% increase in the anode-window spacing, the proportion of window-side events is doubled. (c) Using an event filtering technique, single position peaks were obtained for both types of events.

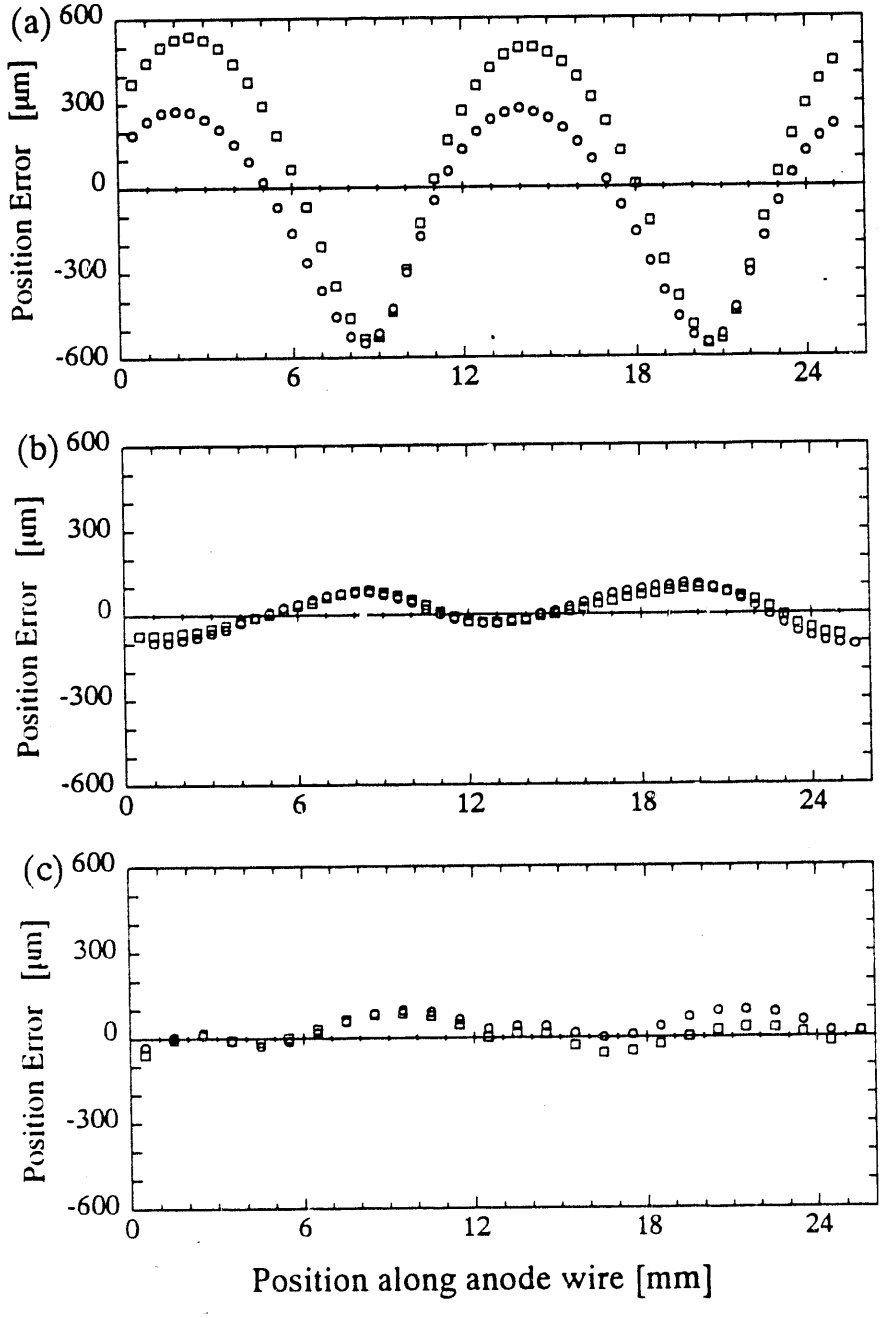

Figure 5.3.9: Position error of pad-side (squares) and window-side (circles) events vs. position along anode wire. (a) centered single chevron, $f_x = 1.05$ (b) displaced one & a half chevron, $f_x = 1.05$ (c) centered double chevron, $f_x = 1.05$. Integration time $\approx 1.4\,\mu$s.

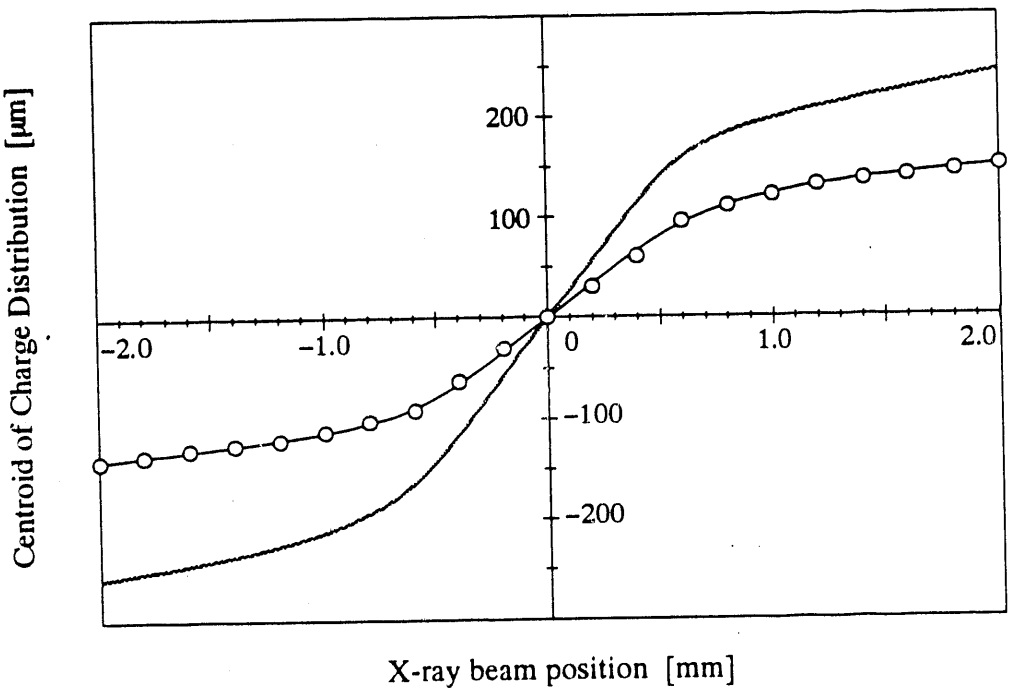

Figure 5.3.10: Centroid of the induced charge distribution in y direction as a function of the x-ray beam position in y. The hollow circles represent results directly calculated from the centroid finding formula. The shaded line represents result of the calculated centroid positions with correction of the non-linearity. Integration time $\approx 1.4\,\mu$s.

channel. Three such channels from three pad rows were connected to the analog centroid finding system. The centroid from the three channels represents the centroid position of the induced charge in y direction.

The shift in the centroid of induced charge distribution in y direction is normally of little concern, because it is not in the direction of great interest. Nevertheless, the information can be used to improve the position resolution of a chamber in y direction, beyond the limit of anode wire spacing. However, for some geometrical charge division methods such as chevrons, it can cause a position encoding error in the x direction, in other words, centroid shift in x. This can be easily understood by the illustration in Fig. 5.3.11.

An absolute measurement of centroid shift was made by scanning a pencil beam of photons in 200 μm steps in the y direction, across one cell of the detector, i.e. from directly over one field wire to directly over the next field wire, while keeping

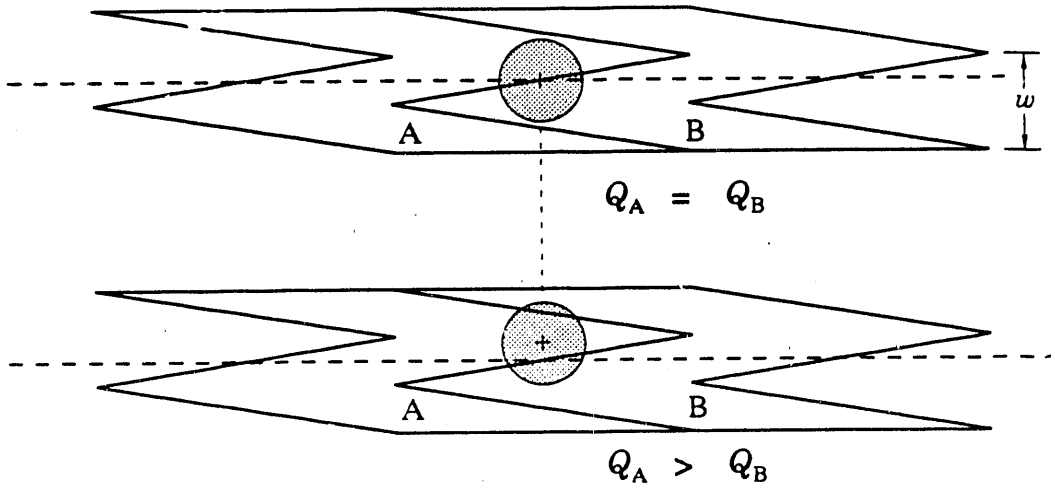

Figure 5.3.11: Effect of shift of induced charge distribution on its encoded x position. The shaded circle represents the spread of induced charge over two one & a half chevron pads. If the centroid of induced charge is centered over the anode wire, equal amount of charge is induced on both pads. If the centroid of induced charge moves in the y direction away from the wire, different amount of charge will be induced on the pads, which will give a different reconstructed position in x. Nevertheless, if the width of the chevron pattern w is narrower than the spread of the induced charge, the shift in encoded x position can be largely eliminated. Shown here is the "between nodes" position.

the x coordinate fixed. The results for the displaced one & a half chevron are shown in Fig. 5.3.12. The scan in Fig. 5.3.12(a) was taken over the node position of the chevron pattern (very close to the chevron apices) and that in Fig. 5.3.12(b) was taken midway between nodes. The centroid shift is the worst when the x-ray beam is located between nodes, representing movements of about $\pm 120\,\mu$m at $1.4\,\mu$sec. However, the magnitude decreases as the time constant is reduced, because the positive ion cloud from the avalanche has moved a smaller distance away from the side of the anode wire. At 100 nsec, the centroid shift is reduced to about $\pm 30\,\mu$m.

Over a node, the centroid shift is of the order $\pm 30\,\mu$m or less, and is not really a serious problem at any of the time constants. The centroid shift for the displaced single chevron was about a factor of five larger than the data shown in Fig. 5.3.12. Thus, although the displaced single chevron exhibits differential non-linearity only marginally worse than the one & a half chevron, its significant centroid shift represents a major disadvantage. The centroid shift for the displaced double chevron was very similar to that for the displaced one & a half chevron.

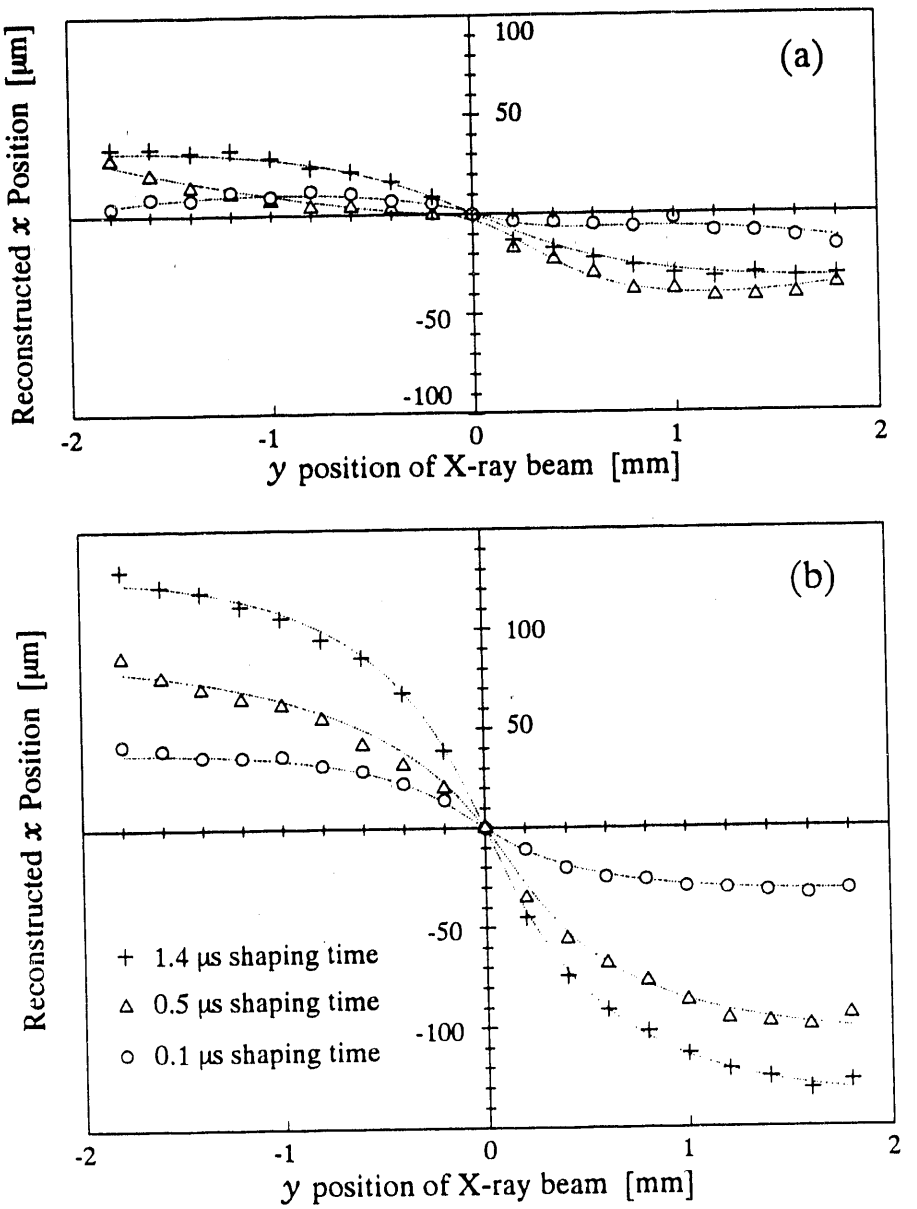

Figure 5.3.12: (a) Centroid shift for displaced one & a half chevron, $f_x = 1.05$, over a node. (+ 1.4 μsec, △ 500 ns, ○ 100 ns) (b) Same for between nodes

It should be noted that Fig. 5.3.12 illustrates a centroid shift which is an odd function of y position of the x-ray beam; this is because the chevron pattern is anti-symmetric about the anode wire. Centered chevron patterns, on the other hand, exhibit an even function of centroid shift because the chevron pattern is a mirror image about the anode wire (see Figs.5.1.1(a),(c) and (e)).

5.3.6 Effect of Anode Wire Position

Due to the special geometry of the chevron cathode, the interpolated centroid position in x is dependent on the location of the anode wire. For the same reason, zigzag strip cathodes are also sensitive to the wire position [42].

Because of the lack of information on the exact field and charge distributions near the gap between the chevron cathodes, a simplified model is used in a computer simulation. It is assumed that the gap width is zero. Therefore no charge is lost and there is no distortion in the partition of charge. The results are discussed below.

A. DFNL and Anode Wire Position

It has been mentioned that for a given chevron (or zigzag) geometry, a displaced anode wire position gives the best DFNL. Fig. 5.3.13 shows some computer simulated results for a centered single chevron pattern. The DFNL *decreases* as the anode wires are displaced from their nominal positions. It reaches its minimum when the wire displacement is 25% of w, which is the wire position of a displaced chevron pattern. On the contrary, displaced chevron patterns have an increase in DFNL when their wire positions are displaced from their nominal positions.

B. Offset in Reconstructed Position

For a centered single chevron geometry, the reconstructed position of any event has a constant offset in addition to the modulation due to the non-linearity discussed earlier, even if the anode wire is accurately placed at its nominal position. Of course the absolute shift depends on where the reference position point is defined on the chevron pad. If the point at which the edge of the chevron pad intercepts the anode wire is defined as the reference point (i.e. integer of l_a), the amount of offset is about

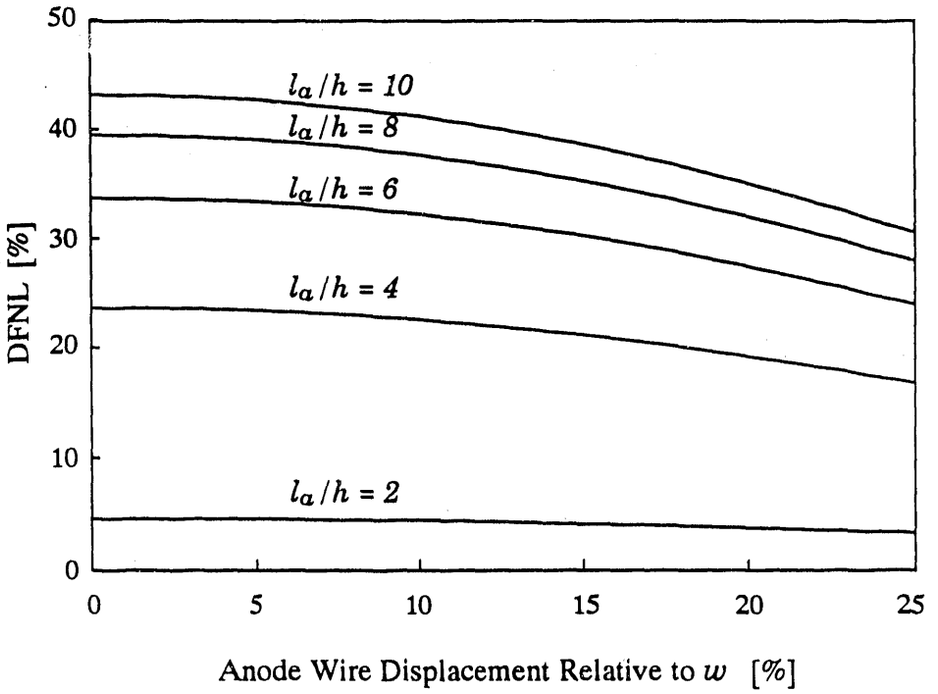

Figure 5.3.13: DFNL vs. anode wire displacement from their nominal position. Centered single chevron pattern was used. $w = 1.5h$.

5% of l_a for a centered single chevron pattern (assuming $w = 1.5h$). There is also a slight offset in the centered double chevron pattern, which is about 0.9% of l_a (assuming $w = 0.75h$). Note that there is no such offset to the displaced version of chevron patterns due to their anti-symmetric patterns.

When the anode wire is not located at its nominal position, there will be a different amount of offset in the reconstructed position for all chevron geometries, as well as the zigzag strips. Offsets for a "displaced" zigzag pattern as a function of the anode wire displacement is shown in Fig. 5.3.14. Note that the centroid shifts are even functions of wire displacement for centered versions and odd functions for the displaced version.

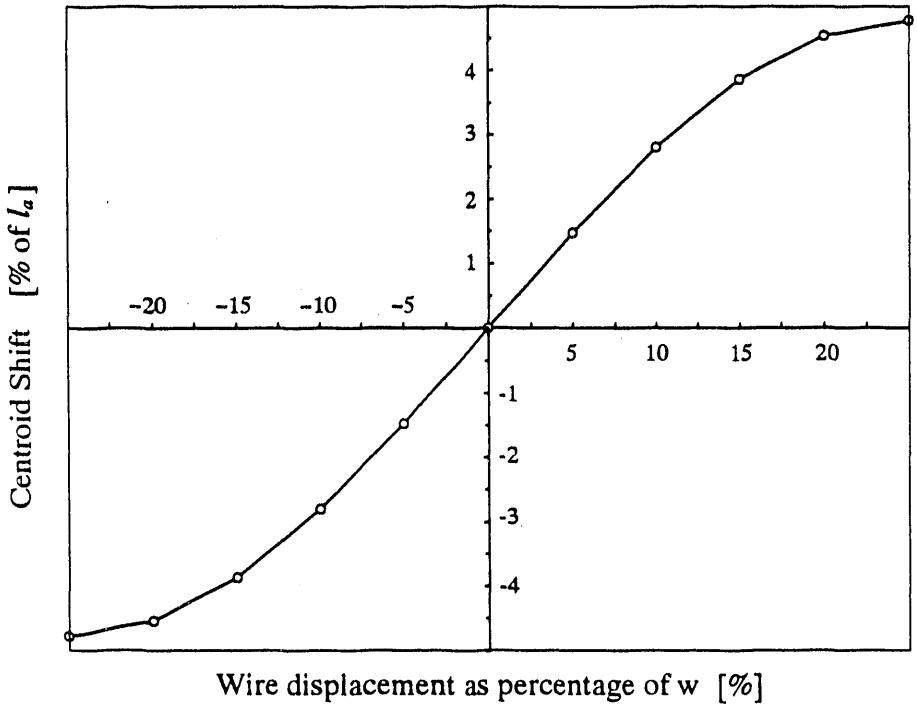

Figure 5.3.14: Offset of reconstructed position as a function of the anode wire position in a zigzag cathode. The anode to cathode spacing h is normalized to unity. $w = 2$, $l_a = 2$.

5.4. Choice of Chevron Patterns

Nearly 30 chevron pad cathodes have been tested to study their performances. Some of the findings in the design of a chevron pattern are summarized below:

a) The displaced versions of the three main chevron types (single, one & a half, and double chevron) exhibit significantly less differential non-linearity than the centered version (see Fig. 5.3.3).

b) For x-rays, the angular localization causes a displacement in recorded position for pad-side and window-side events. For the centered single chevron, this displacement has a maximum which is larger than the position resolution (with 1.4 μs shaping time and 2 mm anode-cathode spacing). This will result in severe degradation in the position resolution, if no event filtering is used. In one & a half, and double chevrons, the effect is small compared with the position resolution, and should not be a concern. For events with ionizing particles, the ionization created by the charged particle is randomly distributed along a

track. For particles with near normal incidence, there will be little distinction between window-side and pad-side events. It is believed that measured displacements in particle tracks will not be as great as those of x-rays, but it is to be experimentally confirmed. Note that with shorter shaping time and (or) larger anode-cathode spacing, the amount of displacement will be reduced.

c) The centroid shift is an odd function of the y position of the incident beam for displaced chevrons, and an even function for centered chevrons. For the single chevron, the centroid shift is significant at all time constants. For the one & a half chevron, the centroid shift is significant at 1.4 μs (of order $\pm 100\,\mu$m), but falls to negligible levels at 100 nsec. Therefore, it is not a problem for detectors with short shaping times. Similar to the item b) above, a larger anode-cathode spacing will reduce the amount of centroid shift. Note that the centroid shift exists for both x-ray and charged particle events.

d) In fabricating chevron pads on a printed circuit board, it is essential to keep the gap between adjacent pads as small as possible, because an increase in differential non-linearity will otherwise occur. A ground plane between the cathode pad plane and the readout leads can effectively shield the readout leads from crosstalk. However, it does add significant capacitance to the input of the preamplifiers.

Chapter 6.
Detector Construction

6.1. Construction of the Resistive Pad Chambers

Two chambers with resistive charge division were built in the Instrumentation Division of BNL. The first one is a prototype for testing of the charge division scheme as well as the low mass structure of the detector.

The detectors were designed as tracking chambers used in a fixed target heavy ion experiment (E-814) in the AGS of BNL. In this experiment, particles from the heavy ion beam pass through the active area. Therefore it is very important to maintain as little material as possible in the detector's active area. This led to the development of several detector cathode manufacturing techniques.

6.1.1 Construction of the Cathode Board

One of the challenging parts of this project has been the manufacture of the cathode pad planes. There are two main constraints on this type of cathode plane.

i. The material in the active area must be less than 1% of a radiation length. This is to minimize multiple scattering of the particle as well as to reduce the number of δ electrons generated by the heavy ions.

ii. In order to maintain uniform detection efficiency throughout the detector, and to aid in particle identification through a measurement of ionization density, it was required that the detector gas gain variation throughout the chamber be less than about $\pm 10\%$. This translates into the requirement of keeping the spacing between anode and cathode constant to within about $\pm 2\%$, or $\pm 40 \mu$m [2].

Fig. 6.1.1 is a photograph of the finished prototype chamber. Some basic parameters of this detector are: active area 20 cm $\times$ 10 cm; readout spacing 1 cm; total number of readout channels 525 (21 nodes per anode wire, 25 anode wires); pad size is 0.6 mm in x and 2 mm in y. The detector mother board is 44.5 cm $\times$ 47 cm.

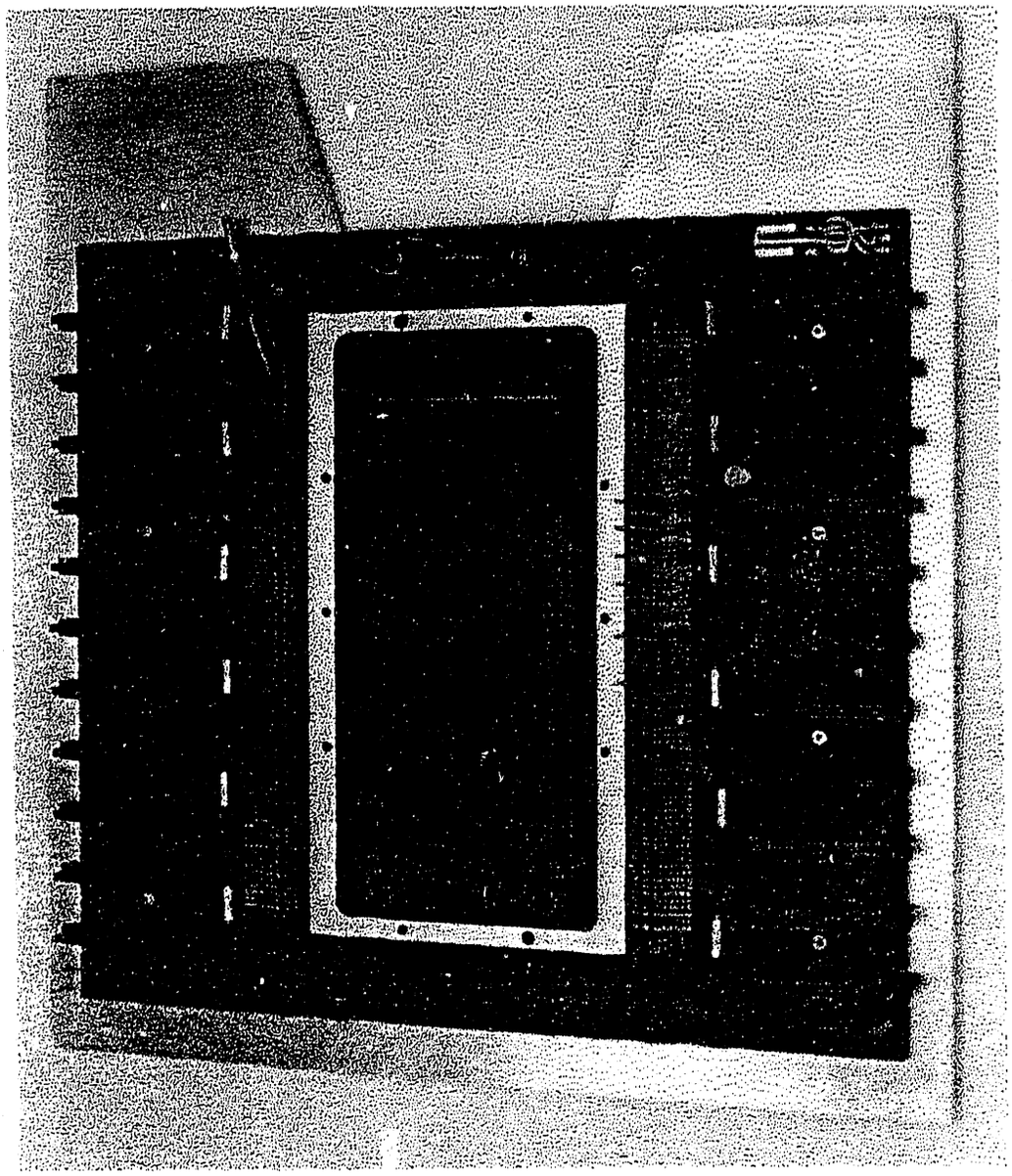

Figure 6.1.1: A photograph of the prototype pad chamber. The detector mother board is mounted on an aluminum plate. The cut-out of one side of the plate is to avoid obstruction to other detectors behind it in the experiment. The active area is in the center, surrounded by an aluminum spacer which defines the spacing between the wire plane and the cathode pad plane. The wire frame and the window frame have been removed for the purpose of this photograph. Several preamplifiers are plugged into their sockets. The circuitry at the upper right corner of the detector is a filter for the preamplifier power input. See text for detailed descriptions.

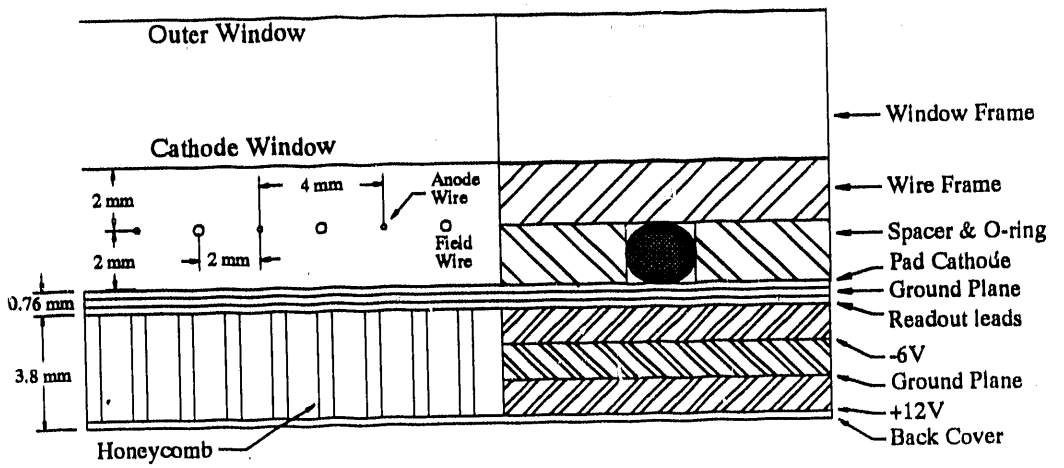

Figure 6.1.2: A partial cross section of the prototype pad chamber showing some dimensions of the detector.

The cathode plane was built using multilayer printed circuit board techniques (Fig. 6.1.2). The first step was to make a three layer board. The pads and guard strips were etched on the first layer. All the readout leads were etched on the third layer and connected to the pads on the first layer by plated-through holes. The second (middle) layer is a ground plane to shield the pads from the readout leads. It also helps to reduce the crosstalk between adjacent leads. To minimize the amount of material, the thickness of the copper on each layer is about 5 μm. The total thickness of this board is about 0.76 mm.

The second step was to make a three layer board with the active area cut out. This board carries the power and ground busses needed by the preamplifiers. The thickness of this board is 3.8 mm. The next step was to fill the cut out area of the second board with a sheet of HEXCELL polyimide honeycomb, and then glue together (under high pressure and temperature) these two boards plus a thin sheet of fiberglass as the back cover. The honeycomb provides the structural rigidity necessary to maintain the required flatness of the cathode plane.

A layer of resistive polymer ink was applied over the pads on the finished cathode pad plane using a silk screening technique. It was found that the resistive ink does not protect the copper pads from oxidizing, which would make the contact resistance to the pad unpredictable. In order to make a good electrical contact with the resistive ink, the cathode pads were plated with a layer of gold 0.25 μm in thickness.

The choice of resistive value between pads is such that the total resistance between readout nodes, R_n, and the cathode pad capacitance per readout node, C_n, satisfies:

$$\tau_n = R_n C_n \approx \tau_F$$

In our case, $\tau_F = 200\,\text{ns}$, $C_n = 2.7\,\text{pF}$; therefore we chose $R_n = 80\,\text{k}\Omega$, which means 8 kΩ between pads.

The resistive strips on each pad row extended beyond the last pads to a copper strip which is grounded. This arrangement was to ensure that the pad electrodes were properly biased, so that the charge collected on the pads could be drained quickly.

The resistive ink was manufactured by Minico/Asahi Chemical of America. The available resistivity of the inks were 20, 100, 1k, 10k, 100k and 1M Ω/square. The resistive ink requires a curing process at 250°C for 30 minutes in a convection type oven or at 250°C for 4 minutes in an infra-red oven. This temperature can be damaging to certain types of printed circuit board materials. The thickness of the cured resistive strip is 15 μm.

Fig. 6.1.3 shows an enlarged view of one of the test pad cathodes. Two rows of pads are shown in the photo. Both resistive strips were printed on the printed circuit board using a silk screening technique. The tolerance in resistive value obtained from this technique is about $\pm 5\%$. The resistive strip on the bottom of the picture was abrasively trimmed to a predefined value. The precision of trimming can be expected to be $\pm 2\%$. Resistor trimming is a standard procedure for hybrid electronics manufacturing. However, the area of trimming is relatively small. None of the pad cathodes used on the detectors was trimmed because their dimensions were too large for the trimming machine.

Fig. 6.1.4 is the art work of the readout layer of the printed circuit board. The readout leads connecting the readout nodes were fanned out to both sides of the active area, where two rows of preamplifier sockets were mounted. The preamplifier used is a three channel charge sensing hybrid type, (BNL–IO–454–4, see Fig. 2.4.1). A copper strip 2.5 mm wide was etched on the second layer of the motherboard (ground plane) across all the readout leads (which are 250 μm below) near the input of the preamplifier. The strips provided a means of calibrating the readout electronics.

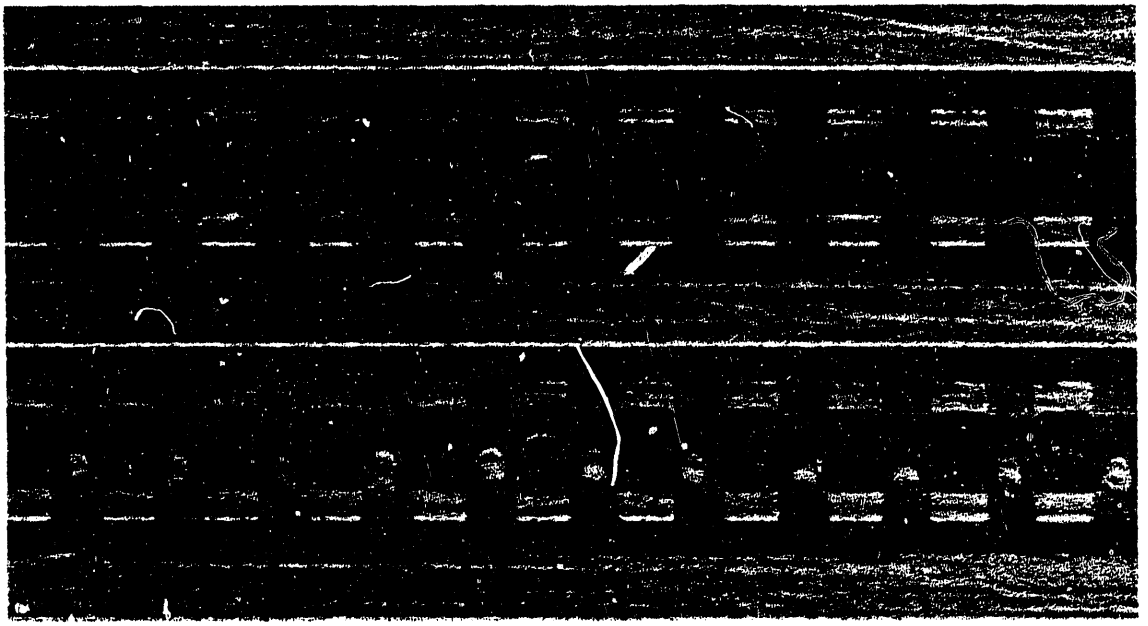

Figure 6.1.3: Enlarged view of one of the test pad cathode. Two rows of rectangular copper pads are shown in the picture with two resistive strips (black colored). The resistive strip on the bottom was abrasively trimmed to achieve a better uniformity. The two plated-through holes connect the pads to readout leads on the back of the cathode board.

The leads connecting the outputs of the preamplifiers were fanned out to two groups of ribbon cable connectors on both ends of the motherboard. Beside each connector, there is a row of resistors for termination of the cable.

The second detector is a full sized chamber. It has a similar cell geometry to the prototype, except that the anode wires to cathode window spacing is 4 mm. The primary ionization for particle tracks therefore increases by 50% due to the increase of the volume. This allows the chamber to operate at a lower gas gain while maintaining the same signal level as in the prototype. There are 40 anode wires and 41 field wires. The cathode pads are 0.9 mm in x and 2 mm in y. The pad pitch is 1.5 mm. This detector has an active area of 26 cm by 16 cm, with a total of 1016 readout channels. Since this detector is designed for use in a fixed target experiment where the track density varies across its active area, different readout densities are used in order to maintain good double track resolution. In the central region where we expect maximum track density, the readout spacing is 6 mm (4 pads per readout). In the outer region, readout separations of 12 mm (8 pads per readout) and 15 mm (10 pads per readout) are used.

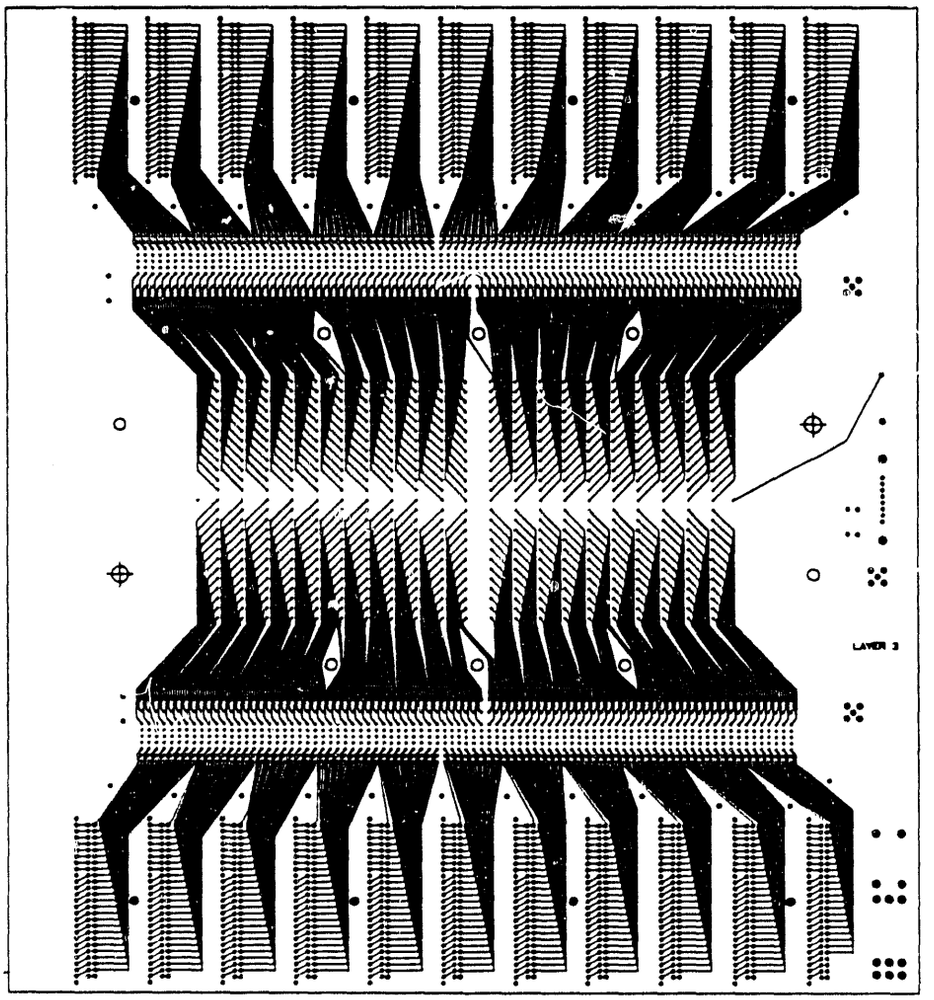

Figure 6.1.4: Art work of the readout layer of the prototype chamber

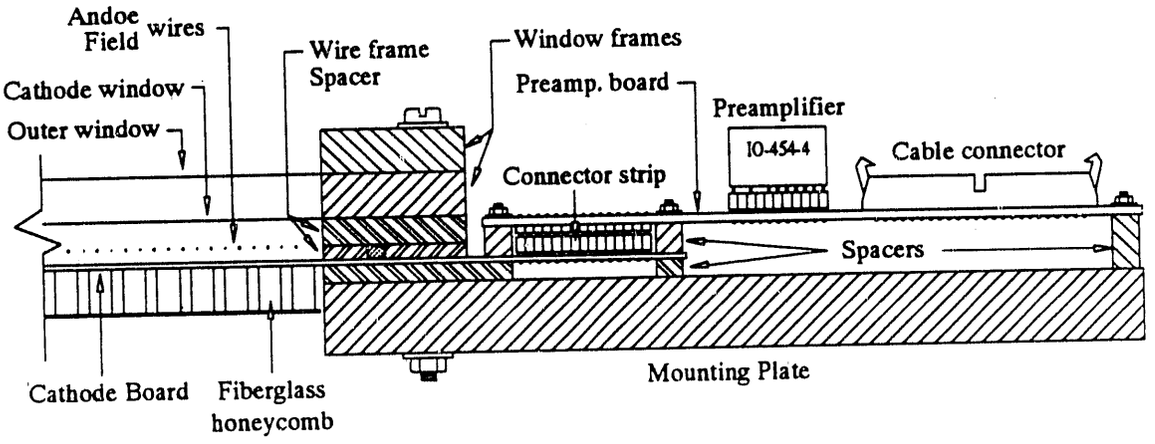

Figure 6.1.5: A partial cross section of the full-size pad chamber

The construction of this chamber is different from the prototype. As mentioned earlier, the resistive ink has to be cured by baking the printed circuit board at a temperature of 250°C for 30 minutes. Under this condition, the bonding between the printed circuit board material and the honeycomb filling becomes unstable. Several test boards fell apart during the baking process. In addition, the readout leads of over 1000 channels have to be fanned out to a much longer distance to match the preamplifier density. Due to the density of the readout, the width of the copper leads has to be narrower than 150 μm. With present technology, it is extremely difficult to make a large printed circuit board which has very narrow traces without there being some open or short circuits.

Therefore, another structure was developed for this detector. Fig. 6.1.5 illustrates a part of its cross section. A set of three printed circuit boards were made instead of a single board. One is the cathode board, the other two are the preamplifier boards. The cathode printed circuit board has three layers, which contain pads, ground and readout leads, respectively. Its thickness is 0.76 mm. The pads were plated with gold, applied with resistive ink and cured under infra-red lights. After the resistive strips had been applied, the cathode board and a thin sheet of fiberglass were glued on to both sides of a sheet of fiberglass honeycomb 6.35 mm thick. This assembly was then held on a flat surface for the epoxy to cure. The flatness variation on the active area was measured to be within $\pm 40\mu$m.

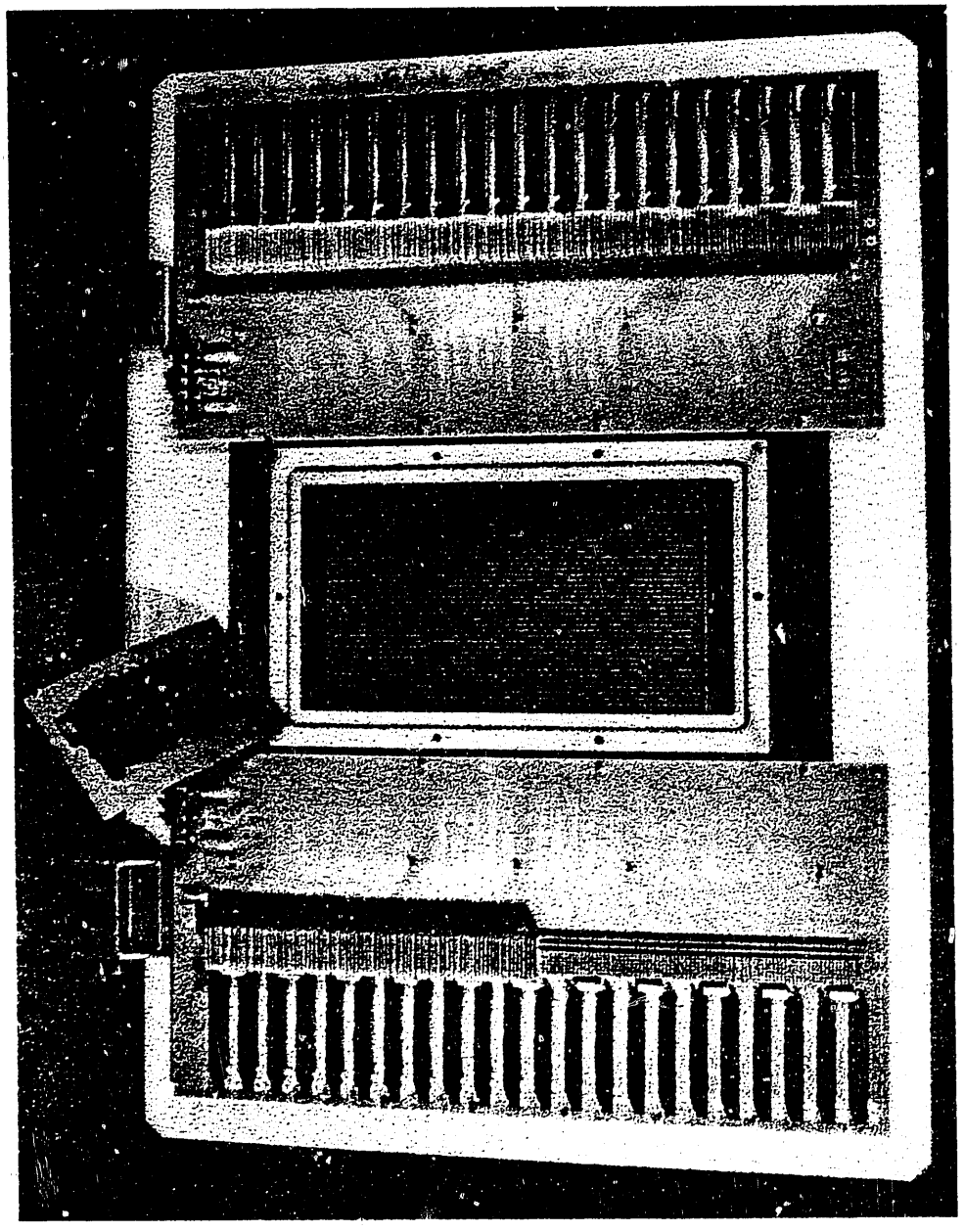

Figure 6.1.6: Photograph of the full-size pad chamber with window and wire frame removed. This photograph was taken with the detector lying sideways, held down by the two vises shown on the left. The active area is in the center, surrounded by two fiberglass spacers, The spacers maintain the correct spacing between the wire plane and the cathode plane, and retain the O-ring for gas seal. Two preamplifier mother board are plugged into the cathode board through rows of connectors. The bank of preamplifier sockets is half filled on the bottom board. A small piece of the fiberglass honeycomb used on the back of the cathode board is shown on the left-hand side of the photograph.

One potential problem associated with this technique is that the cathode board may not be gas tight. The plated-through holes for the readout connection need to be properly handled. They could be plated shut at the time of the through plating process. They could also be sealed by adding a thin film between the honeycomb and the printed circuit board. The method we used was adding an additional layer of epoxy around the perimeter of the honeycomb, since the gas leak was found after the chamber was assembled. There would be some air trapped in the honeycomb cells which requires a longer time to purge.

The readout leads from the active area were fanned out to both sides of the cathode board and connected to rows of sockets. On the preamplifier boards, connectors were mounted at corresponding positions. The readout leads on the preamplifier boards were further fanned out from the connectors to the preamplifiers sockets. The preamplifier boards were plugged into the cathode board and held on by several aluminum bars. The connections through the connector for the readout leads were surprisingly good, even with over 1000 channels. Fig. 6.1.7 shows the layers containing the readout leads of the cathode boards. Fig. 6.1.8 shows the readout leads of one preamplifier mother board.

The total material in the active area is about 0.5% X_0 for the prototype and 0.6% X_0 for the full-size detector, in which X_0 is the radiation length for the material.

It is worth mentioning one of the interesting aspects of this type of readout. If one of the readout channels is disconnected, i.e. one node along the pad row is floating, the position information is not lost. One can still obtain the information from the other two neighboring nodes. Effectively, the section of the chamber has a readout spacing twice as long as the rest of the chamber. Of course one has to modify the centroid finding formula to accommodate the change of the readout spacing for those two nodes. However, if one node is shorted to the ground, the result is much worse—the section of the chamber with a length of twice the readout spacing becomes insensitive. So in practice, if any readout channel is found to be dead, simply disconnecting the readout electronics from the readout pad will maintain the sensitivity of the chamber.

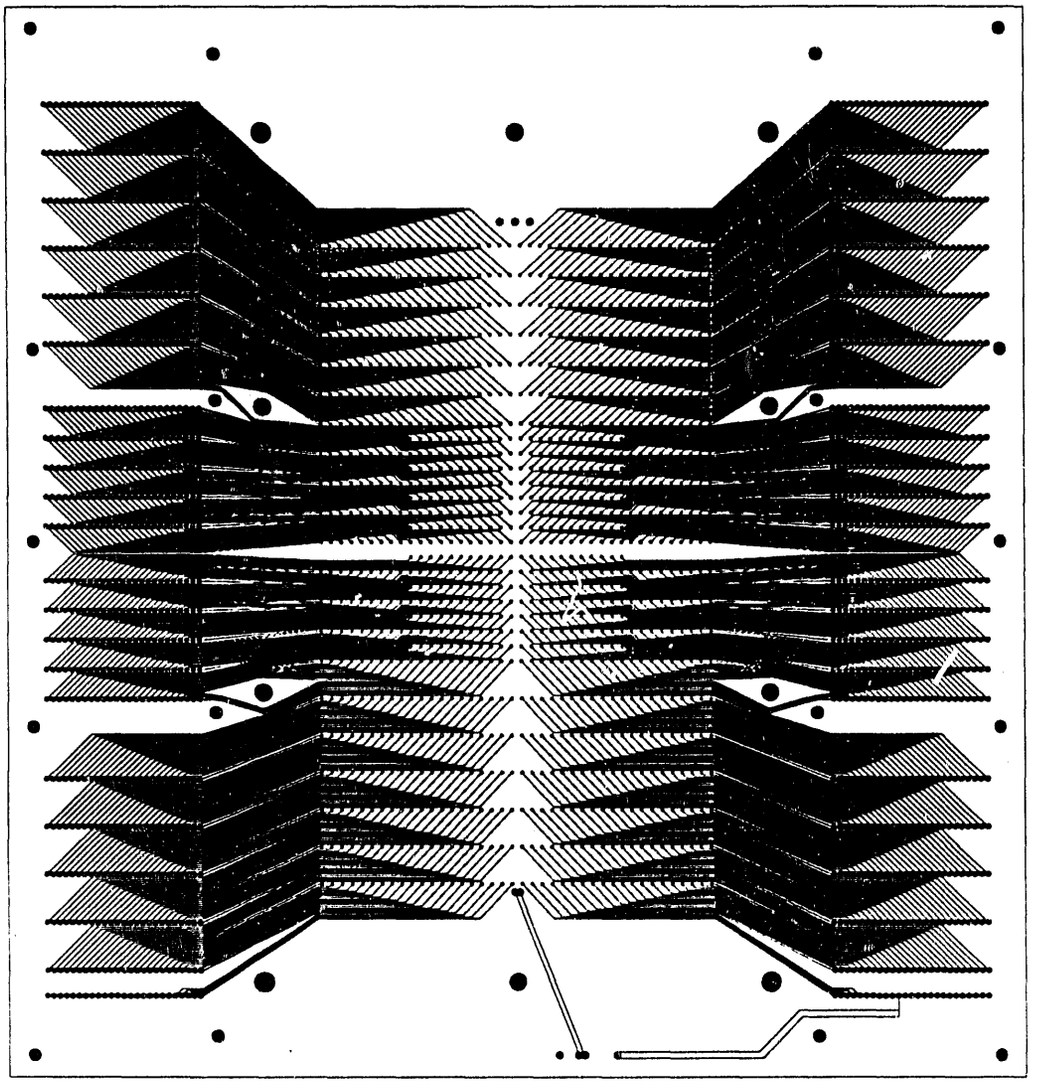

Figure 6.1.7: Readout layer of the pad cathode board.

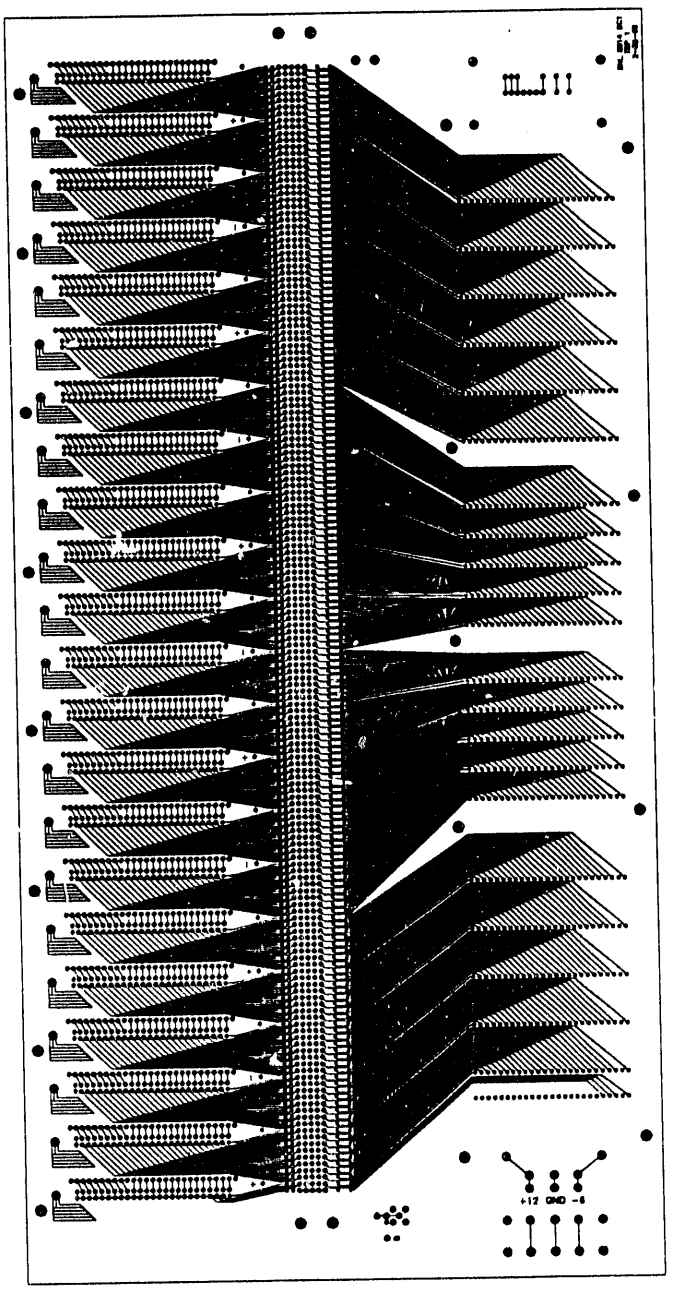

Figure 6.1.8: The readout layer of one of the two preamplifier mother boards

6.1.2 Wire Frame Construction

The anode wires used in both detectors are gold plated tungsten with a diameter of 18 μm. The field wires are 125 μm stainless steel wire. Wires for the prototype were laid down manually on a pitch bar and then glued on a wire frame with epoxy. Wires for the full-size chamber were laid down on a transfer frame by a winding machine and then transferred to the wire frame. The tension of the anode wires was 30 grams and that of field wires 100 grams. Electrical connection to the wires was made by conductive epoxy to pads on the wire frame.

Both wire frames were made of multilayer printed circuit boards. All the field wires were connected together by a bus. The anode wires were interconnected into several groups. Each group can be individually read out or pulsed by an external test pulser. By sending a test pulse signal through the anode wires while monitoring the response of the cathode pads underneath the wire, one can calibrate the complete electronics chain. This is a more realistic measure of the system, since it resembles the mechanism of the induced charge from the anode to the cathode pads. Wires in each group are physically separated by several wires such that the pads under one wire will not be affected by the other wires. This scheme could also offer some estimate of the charge sharing between pads under neighboring wires. Fig. 6.1.10 illustrates the electrical connection for the anode wires.

The prototype chamber uses aluminized mylar as the cathode window. It was placed 2 mm above the wire plane. The window was held at ground potential. A second window was used as the gas barrier to ensure the flatness of the cathode window against pressure differential.

The cathode window for the full-size chamber was placed 4 mm above the wire plane. Because of this asymmetrical cell geometry, however, a negative bias potential has to be applied to the window in order to obtain a near symmetrical field on both sides of the anode wires. The cathode window was made of 13 μm mylar film. It was stretched and glued to an aluminum frame, and then a layer of aluminum was vacuum deposited. A small clearance between the aluminum coating and the edge of the aluminum window frame was maintained.

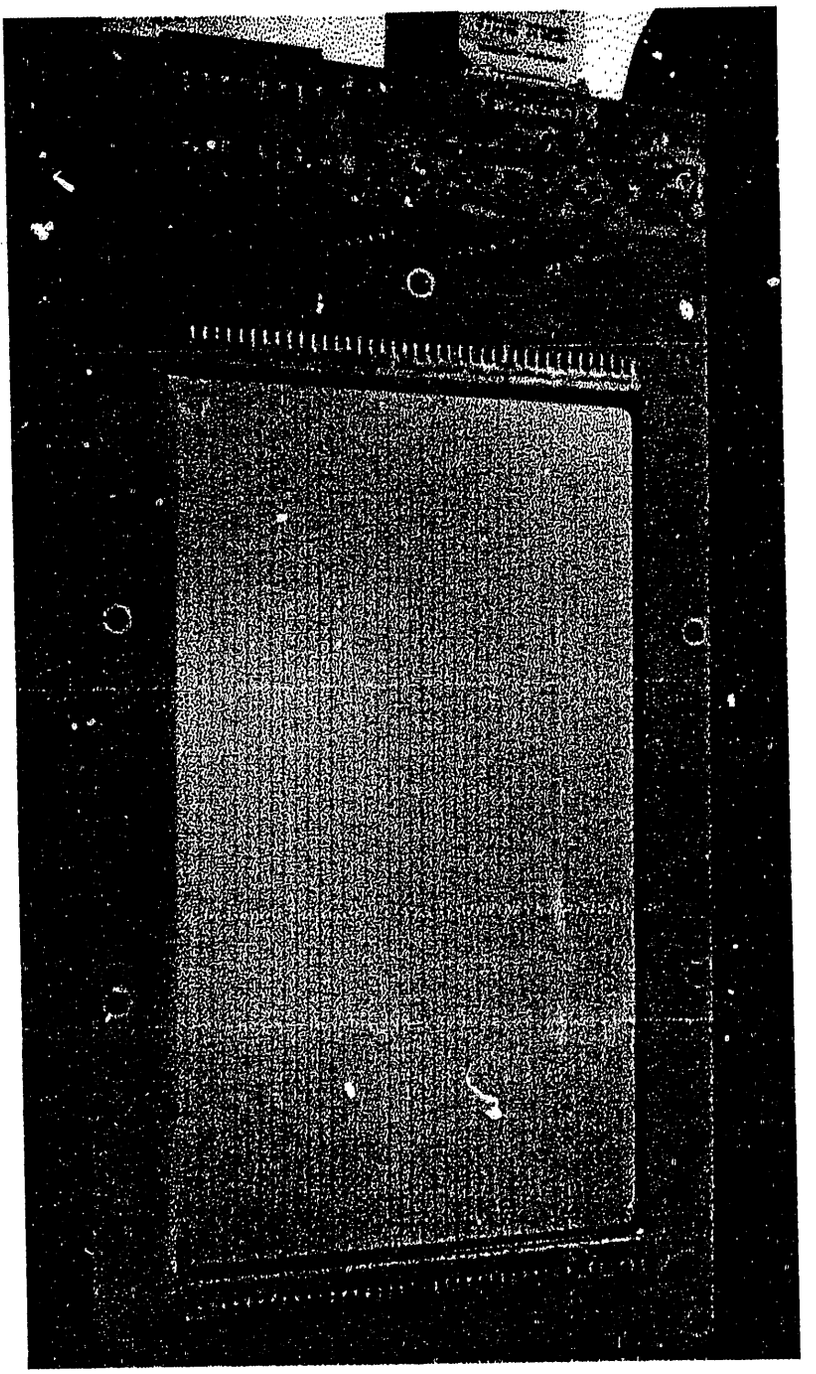

Figure 6.1.9: Photograph of the wire frame of the full-size pad chamber. It has 40 anode wires (18 μm diameter), which are too thin to be see on the photograph, and 41 field wires (125 μm diameter). The two slots on the upper left and lower right corner of the wire frame allows the circulation of gas. The window is a sheet of mylar with a layer of vacuum deposited aluminum. A layer of bee's wax covers the surface of the printed circuit board which is exposed to the air, in order to prevent moisture from seeping through the fiberglass. All the electrical components on the other side of the wire frame are also covered with wax.

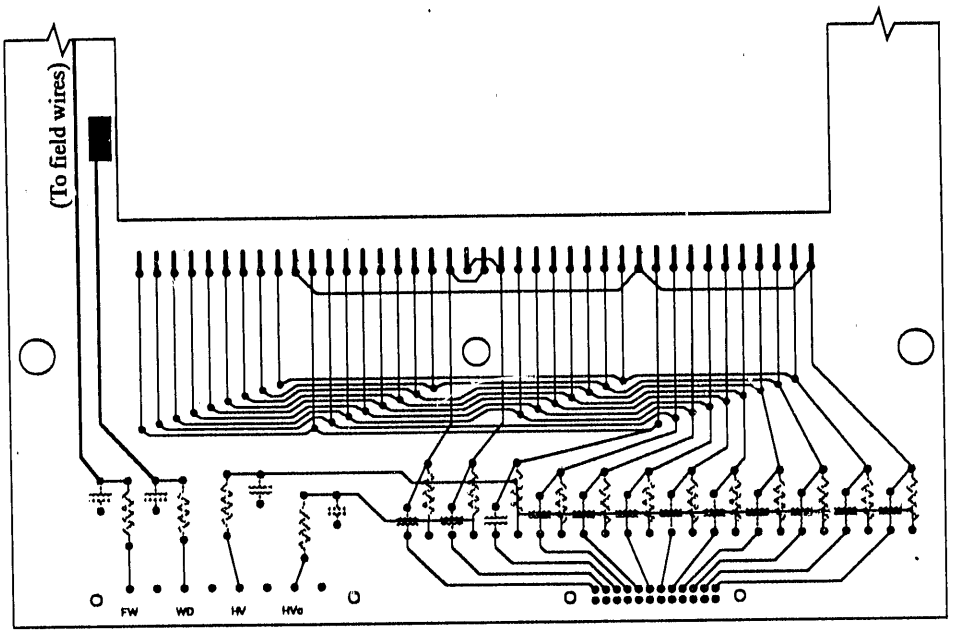

Figure 6.1.10: Electrical connections on the wire frame of the full-size pad chamber. All resistors are 10 MΩ to limit the current to the anode wires. All capacitors are 1000 pF. Note that this is a 4 layer printed circuit board. All the traces shown are on inner layers.

One special feature of this wire frame is the ability to supply different high voltage to four anode wires located in the middle of the active area. During the experiment, the heavy ion particle beam passed through the center of the chamber. In order to be sensitive to the minimum ionizing particles while maintaining a safe anode charge level for heavy ion particles, a lower voltage was supplied to the center four wires.

The voltage settings for the window and the field wires were selected based on the energy resolution of the chamber for x-rays. A series of 5.9 keV x-ray energy spectra were collected by setting the voltages on the anode wires, field wires and the window while maintaining the anode charge at a constant level. Fig. 6.1.11 shows some of the energy spectra of the detector at various voltage settings. A voltage setting with the window biased at about 1/4 of the anode voltage and field wires biased at 0–1/4 of the anode voltage gives fairly good energy resolution.

The gas gain uniformity of both detectors was measured. The prototype detector had 5% peak to peak variation throughout the entire active area. This can

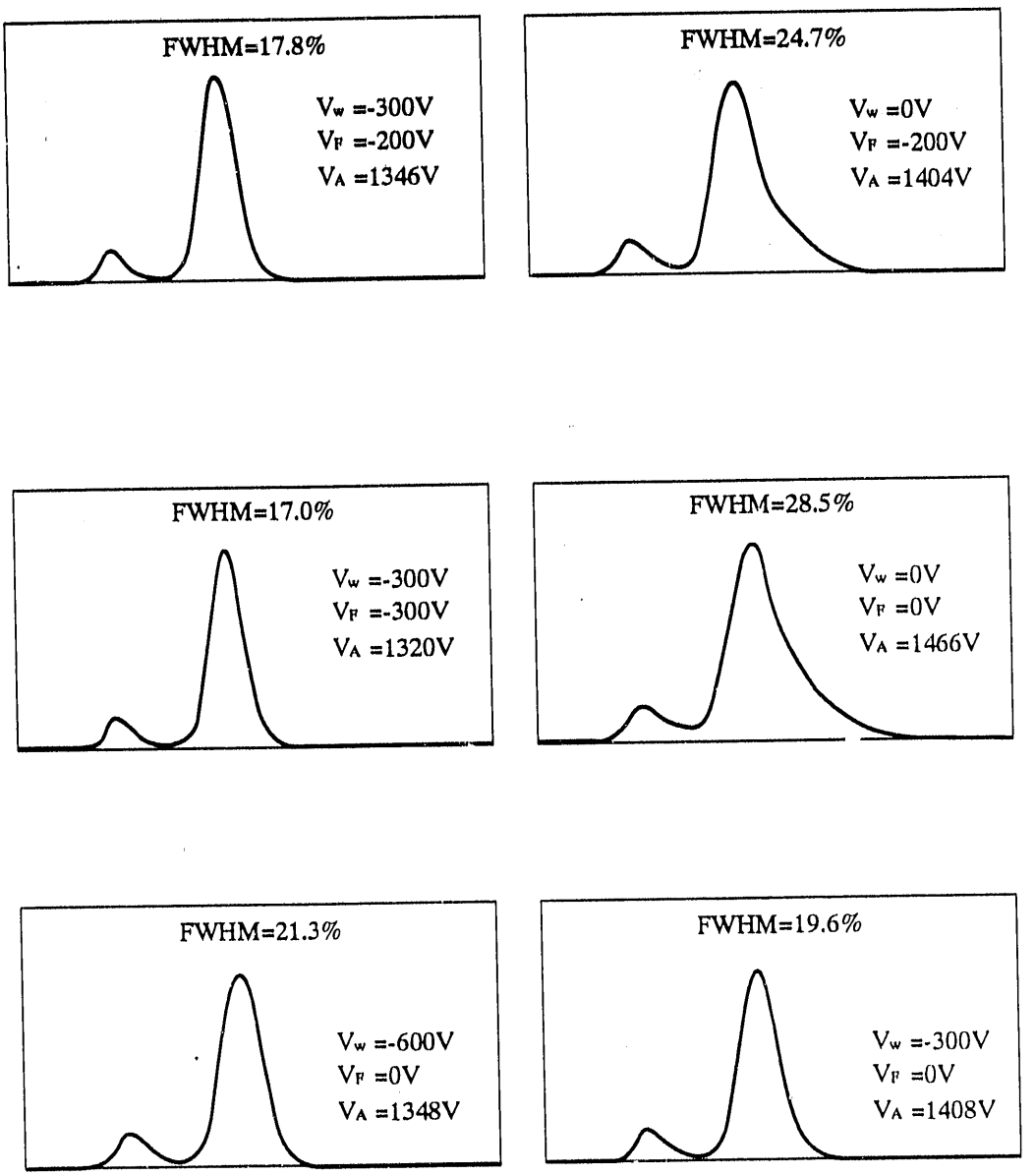

Figure 6.1.11: Energy spectra of the full-size pad chamber for 5.9 keV x-rays in P-10 gas. The anode charge level was maintained at 0.5 pC (200 ns shaping time) at all the voltage settings. The energy resolution for each voltage setting is shown in the graph.

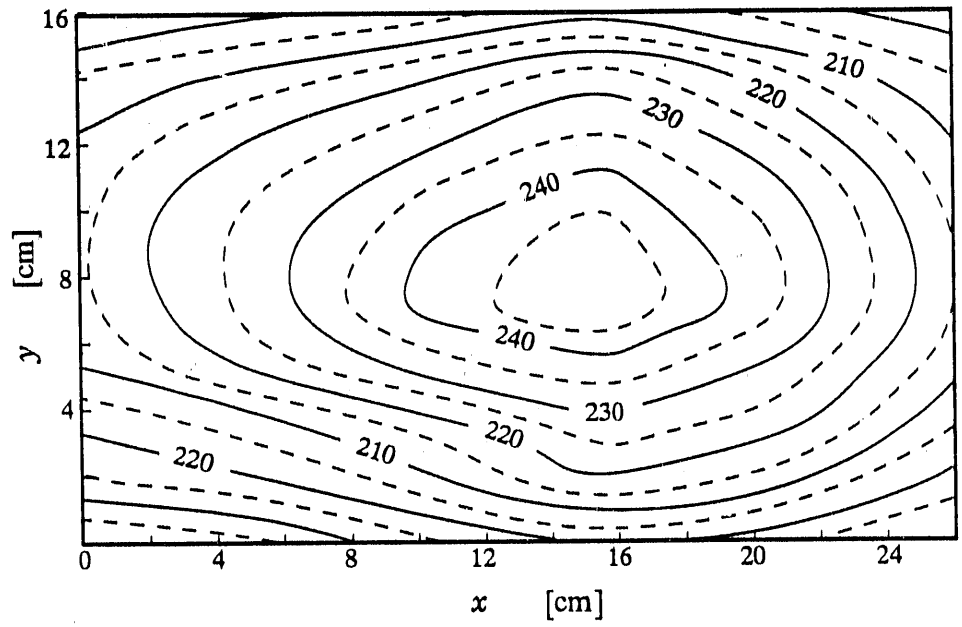

Figure 6.1.12: Gas gain non-uniformity of the full-size chamber. The wire frame with loose wires was used in this measurement. Gas gain was measured with 5.9 keV x-rays at 2.54 cm × 2.54 cm grid points. The gain units are arbitrary.

be attributed to the excellent flatness of the cathode plane. The full-size chamber showed greater variation. Fig. 6.1.12 shows the gas gain versus the position of measurement at 1" (2.54 cm) grid. The absolute variation was about ±15%. This could be due to several factors such as the flatness of the cathode board, the tension of the wires and spacing between wires.

It was found that several anode wires on the original wire frame did not have enough tension to remain straight when high voltage was applied. This was discovered during a calibration of the centroid finding system. A pulser signal was sent to the anode plane, while the preamplifier outputs of a column of pad readouts under several anode wires (one pad per wire) were monitored on an oscilloscope. The electronic gain was adjusted so that the outputs from each pad displayed the same amplitude without high voltage on the anode wires. After putting high voltage on the anode wire plane, the amplitudes of some of the channels increased. This was an indication that the coupling between an anode wire and the pad underneath it had increased. The only explanation is that the anode wire had moved under the electrostatic force, towards the pad plane. The asymmetrical cell structure worsened the problem.

Fig. 6.1.13 is a set of photographs of the pulser response from 15 pads under 15 anode wires. The first picture is the response without high voltage, where the electronics gain of all the channels had been equalized. The second photo is the response of same channels with 1400 V on the anode plane. Higher pulse heights indicated larger capacitive coupling between the anode and the pad. If one assumes a linear function between the anode-pad capacitance and distance as the first order approximation, then the resultant maximum displacement of the anode wire was of the order of 250 μm. The sagging of the wires could be decreased by biasing the window at a negative voltage. The third photo of Fig. 6.1.13 shows the results of applying -500 V to the window. The displacement of the loose wires was greatly reduced. This wire frame was later on replaced by another one with properly tensioned wires.

6.2. Construction of the Chevron Pad Chamber

The major components of the chevron test chamber are shown in Fig. 6.2.1. It consists of a fiberglass back plate, the cathode board, a wire frame, a cathode window frame, and an outer window frame. The 6.35 mm thick back plate has two holes drilled through with an O-ring seal for gas intake and exhaust. On the wire frame, there are five anode wires made of 18 μm gold plated tungsten, and six field wires made of 125 μm stainless steel. All the field wires are connected together to a high voltage supply, and through a capacitor to a preamplifier if so desired. Only three of the five anode wires are sensitive. Any combination of the three can be connected to a preamplifier while the rest are coupled to ground through capacitors. The cathode window is made of double sided aluminized mylar and glued to one side of a 2 mm thick fiberglass frame. Both sides of the aluminum coating were connected to a high voltage power supply. This window frame can be mounted either face up or face down, so that the anode-window spacing can be either 2 mm or 4 mm. Through an isolating high voltage capacitor, one can also read out the signal induced on the window. Another 6.35 mm thick fiberglass frame carries the second windows for the gas seal, so that there is no pressure differential on the cathode window.

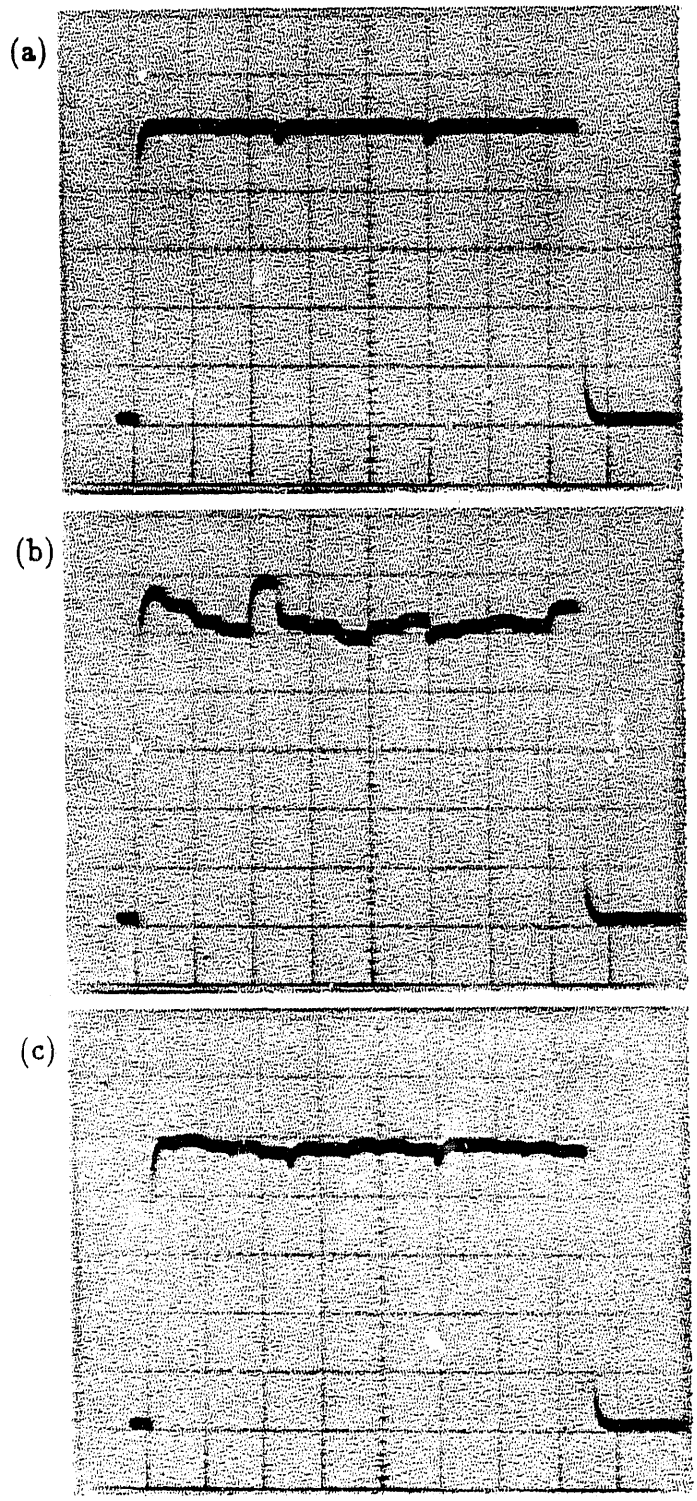

Figure 6.1.13: Photographs of the cathode pad responses while pulsing the anode wires. (a) Signal output from 15 pads under 15 anode wires of the full-size chamber. The electronics gains were equalized before high voltage was applied on the anode wires. (b) Response from the same channels when 1400 V was applied on the anode wires. (c) While maintaining the 1400 V on the anode wires, −500 V was applied on the cathode window. At this bias voltage, the displacements of the anode wires were greatly reduced.

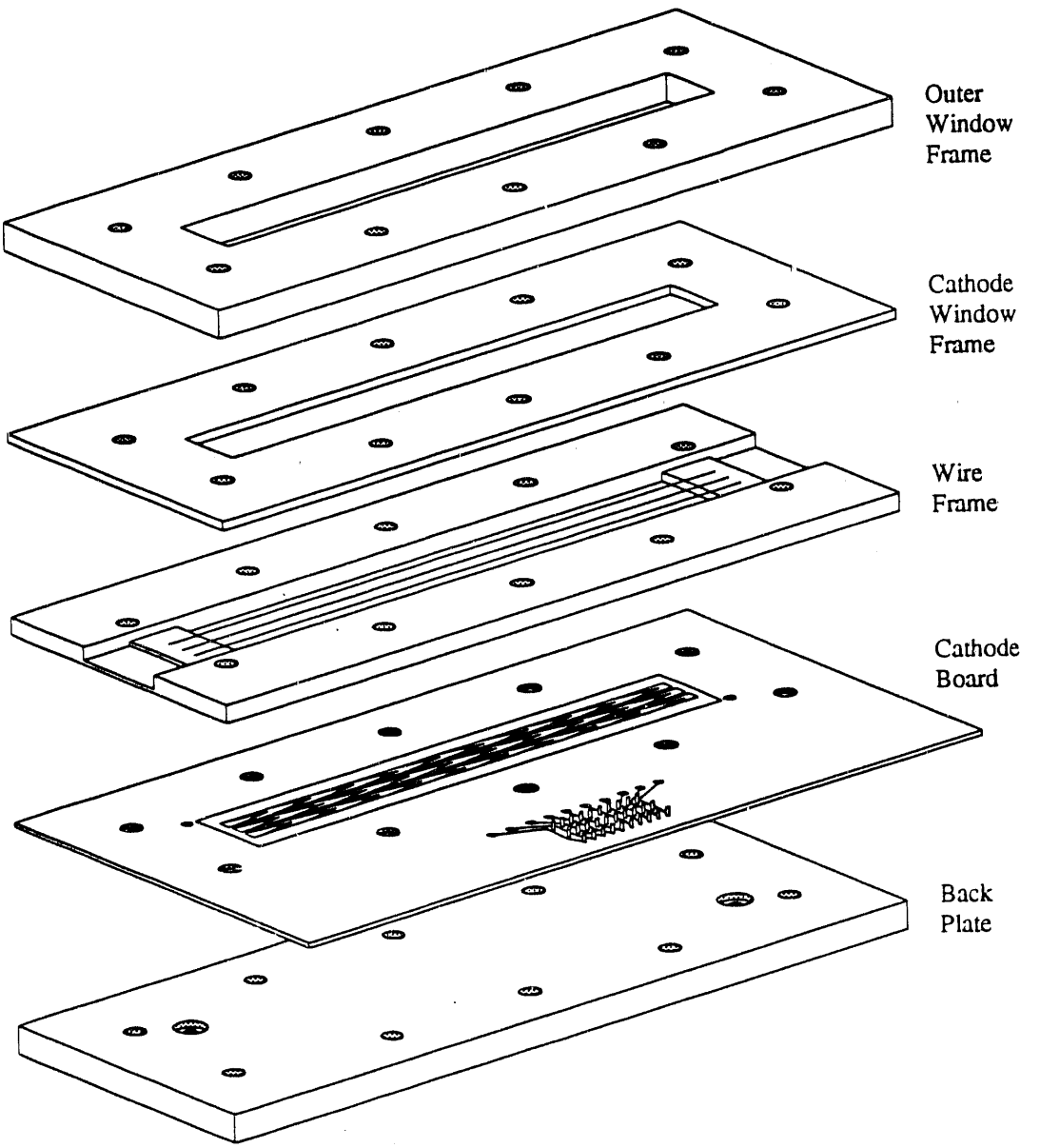

Figure 6.2.1: Components of the chevron test detector

The cathode board is a three layer printed circuit board with a total thickness of 0.8 mm. Fig. 6.2.2 shows the two outside layers of one of the cathode board. Three rows of chevron patterns are etched on the top layer. Normally, all three rows have the same "type" and "version" of chevron pattern, but each row differs in the f_x value (see Fig. 5.1.3). The width of the chevron pads are 3.05 mm (0.120"). The rest of 0.95 mm is taken by a guard strip as shown in Fig. 6.2.2 to separate chevron rows. The primary function of the guard strip is to reduce the quantity of charge induced on the neighboring row. For all the tests in present work, the guard strips are directly connected to ground. The presence of the guard strip is not essential to the operation of the chamber.

The design of this test detector assures that the cathode board can be easily replaced by another with different chevron patterns. Nearly 30 of the readout boards with various readout patterns have been fabricated and tested so far.

Two large wire chambers with chevron pad planes combined with conventional drift layers were constructed at the same time as the the full-size resistive pad chamber. One has an active area of 81 cm × 30 cm (32" × 12"). The other has an active area of 203 cm × 51 cm (80" × 20"). A centered single chevron pattern was used for both cathode planes. The mechanical structures of the cathode plane are similar to that of the full-size resistive pad chamber. The largest chevron pad on the larger chamber has a 25.4 cm readout spacing. The results of their operation were reported in Ref. [4].

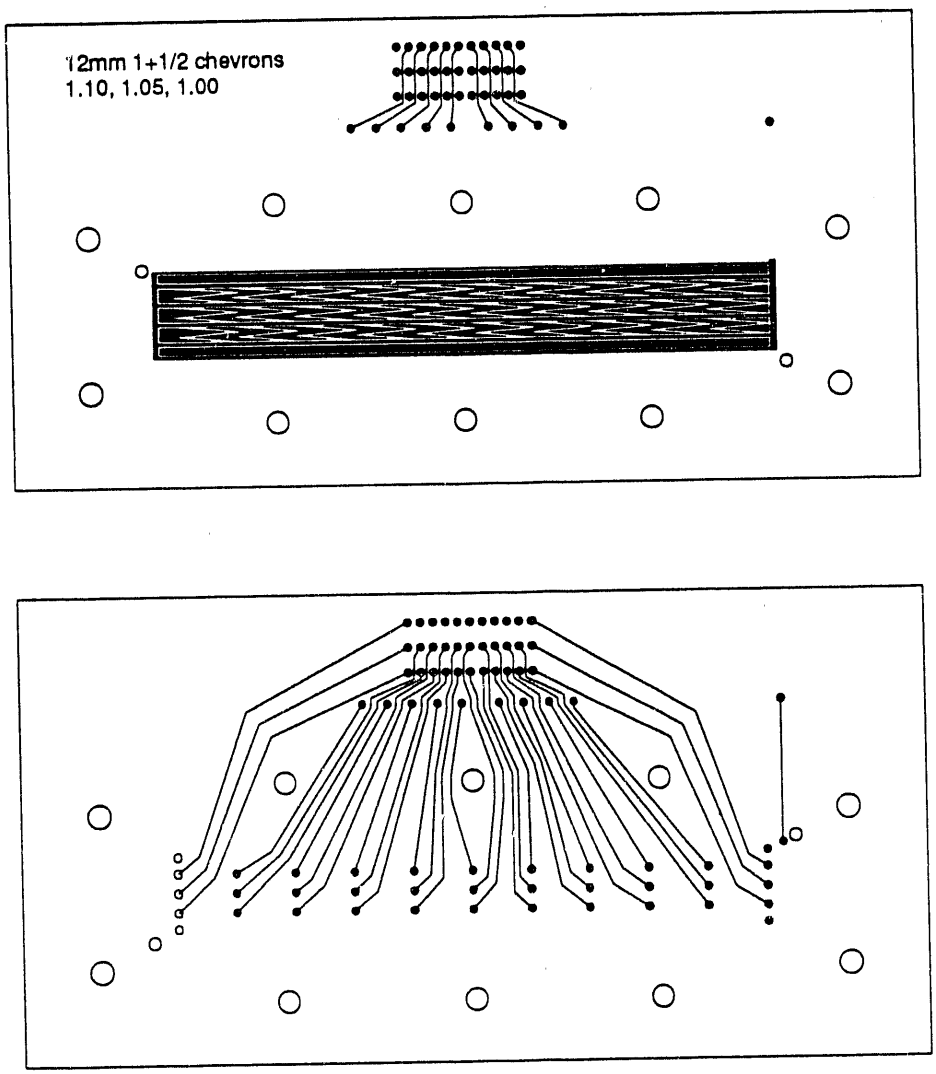

Figure 6.2.2: The art works used to make the printed circuit board for the cathode plane. The top is the first layer, showing three rows of one & a half chevron patterns. The bottom is the third layer, showing the readout leads connecting the chevron pads and rows of connectors.

Chapter 7.
Conclusions and Future Developments

7.1. Conclusions

The two types of position sensitive MWPC can be used in many applications ranging from particle tracking to x-ray imaging. It has been demonstrated in the heavy ion experiment E-814 that both types of chamber can deliver satisfactory results. Their ability to handle high particle multiplicity and provide unambiguous two-dimensional position information affords a very powerful detector technique. The following is a summary of some major features of both types of readout.

Position Resolution

Along the anode wire direction, both types of detector have position resolutions down to about 1% of the readout spacing. The position resolution is mainly determined by the signal to noise ratio of the electronics, and the readout spacing. There will be some degradation in chambers with the single chevron pattern, especially in x-ray measurements.

The position resolutions in the direction perpendicular to the anode wires are mainly determined by the anode-anode spacing ($\sigma_y \sim s/\sqrt{12}$). However, it is possible to make use of the charge sharing across neighboring wires to improve the position resolution between wires. The charge sharing is more pronounced in detectors with small anode-cathode spacing and long shaping time constant.

It is estimated that the double track resolutions of both types of detector are about the same as the readout spacing.

Position Linearity

The position linearity of a detector with resistive pad readout is mainly determined by the uniformity of the resistors. The measured DFNL with untrimmed resistors in this work is about 12%. By using laser or abrasive trimming of resistors, one can expect to reduce the differential non-linearity down to the 2% level. Automated equipment for trimming resistors over a large area has to be developed.

Detectors of a similar type with discrete resistors mounted on the back of the cathode plane have been studied at CERN [53].

The shaping time of the readout electronics may also affect the position linearity. If the shaping time is shorter than the RC time constant of the cathode pads, systematic loss of the signal charge will result in position non-linearity. It is very difficult to correct the non-linearity of the detector without knowing the values of each individual resistors.

In a chevron pad chamber, the position linearity is very sensitive to the cathode pad pattern. The best measured differential non-linearity so far is about 10% on a cathode with one & a half chevron pattern, $fx = 1.05$ and a 60 μm gap between pads. However, the position non-linearity in a particular pad geometry has a highly periodic form, which can be easily corrected.

Detector Dimensions

Due to the complexity in fabricating the cathode plane of a resistive pad chamber, especially in silk screening, curing and trimming of the resistive strips, the resistive pad cathode is perhaps most suited for detectors with small to medium sizes, or large detectors with subdivided smaller cathode modules.

Chevron pad cathode is relatively easy to fabricate. The limitations on its size depend mostly on the printed circuit board techniques. The tolerances in the etching process may prevent the use of very small pad sizes.

The amount of material in the active area in both types of detector is well below 1% of a radiation length with present cathode structures, see Appendix F.

Electronics

In both types of detector, the charge induced on the cathode pads is less than 1/3 of the anode charge, while the centroid finding needs typically 3 readout channels. Low noise, high dynamic range electronics are essential. For a system with ADCs, 8 bit or higher dynamic range is needed, base on results from computer simulations, to achieve a resolution 1% of the readout spacing.

The shaping time of the shaping amplifiers has to match the RC time constant of the resistive pad cathode. This is important in maintain good position resolution

and position linearity [25,19]. So a resistive pad chamber is always optimized for a certain time constant.

Compared with the resistive pad chamber, chevron pad readout does not have the restrictions on the shaping time constant. However, the capacitance for a chevron pad is typically much larger than that of the capacitance per channel of a resistive pad chamber. Matching the input capacitance of the preamplifier therefore is important to achieve low noise performance.

Studies have been carried out in the design of a central tracking detector system to be used in the GEM experiment at the SSC. This design uses a multiple chevron pattern to perform charge division. The required position resolution is 50 μm with a 5 mm readout spacing. Designs using chevron pad readout in a ring imaging Cherekov detector, and in a transition radiation detector, has been proposed for an experiment at the Relativistic Heavy Ion Collider. These two interpolating pad cathodes can also be used in Time Projection Chambers (TPCs), replacing the conventional rectangular pads, to achieve better position linearities.

7.2. Future Developments

7.2.1 Readout Electronics

One major task for applying these two dimensional readout systems in high energy physics experiments is to develop a new type of readout electronics. The current method, as described in Chapter 6, uses hybrid preamplifiers and shaping amplifiers for each readout channel. The presently available density of preamplifiers and readout leads greatly limits the density and dimension of the active detector area. The full-size chamber in this work has probably reached the practical limit in readout area and density using this "conventional" readout scheme.

The R&D work on the next generation of readout system has already been started, which takes advantage of today's VLSI technology. In such a readout system, many channels of readout electronics, such as preamplifier, shaping amplifier etc., are integrated into a single IC chip. These chips will be mounted directly on the back of

the cathode plane of a pad chamber. This scheme is necessary if the readout density and the detector area is very large. However, it may add more material to the cathode plane. Cooling of the electronics is another potential problem.

For a large detector system in which the cathode plane can be subdivided into smaller modules, it may still be possible to mount the readout electronics on the periphery of the chamber. This method will add capacitance of readout leads to the electronics, but nevertheless is simpler to realize.

7.2.2 Variations of the Chevron Patterns

The single chevron is the simplest pattern to use for a large detector with a relaxed position linearity requirement. It is possible to improve its position linearity by using tailored shape—one whose edges are curves instead of straight lines. Preliminary studies have indicated improvements in position linearity in such a design.

Similar to the Graded Density electrode [34] one can also use the "Graded Density Pads" as shown in Fig. 7.2.1 for charge division. The linearity of this electrode can be controlled by adjusting the relative widths and number of the complementary "fingers." The centroid shift of the encoded x position due to the anode avalanche angular localization is expected to be reduced. Like the chevron patterns, this pattern also requires etching of fine lines on the printed circuit board. The disadvantage of this geometry is that the inter-pad capacitance is large due to the longer interface between pads. However, this can be solved by applying the capacitive charge division scheme described in Refs. [41,37]—connecting every other or every third pad to a preamplifier (intermediate pad cathode). The large inter-pad capacitance will enhance the charge division among pads. With this configuration, the inter-node capacitance is reduced. Using this method, readout spacing can be greatly increased while maintaining a good sampling of induced charge. Compared with chevron pad cathode, this intermediate graded density pad cathode is perhaps more reliable with large readout spacings.

The intermediate strip method [41] can also be used on the zigzag strip cathodes. It can reduce the inter-strip capacitance, therefore reducing electronic noise. It can also increase the readout spacing without using zigzag patterns with very sharp

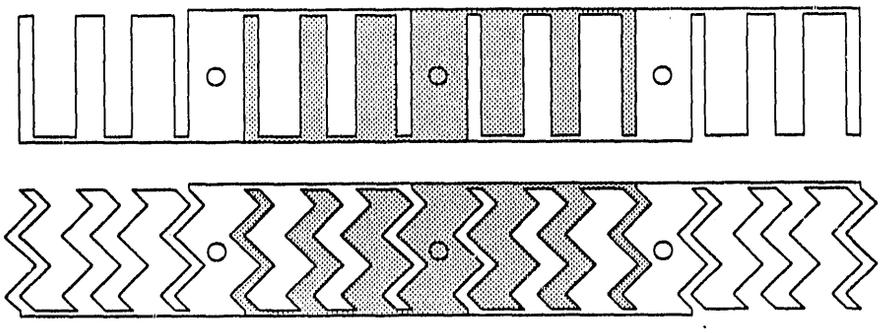

Figure 7.2.1: Two examples of the Graded Density Pad patterns. The circles represent the readout point. One complete pad is shaded in each pattern.

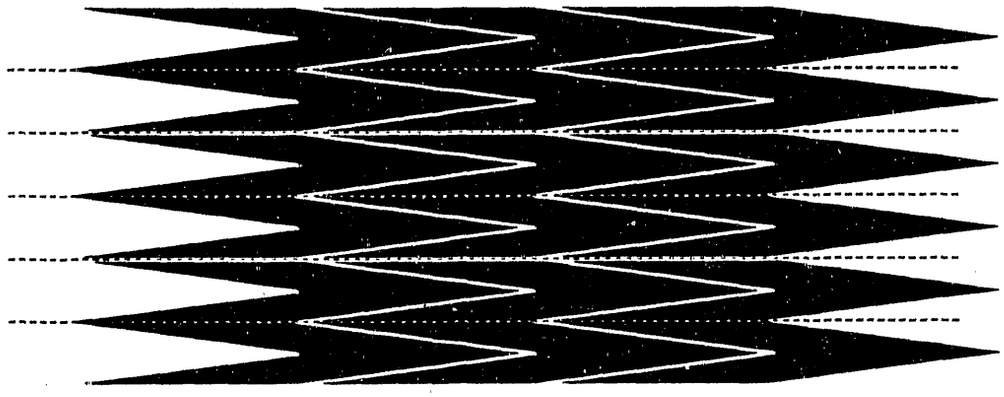

Figure 7.2.2: An arrangement of the chevron cathode pattern to improve position resolution across the anode wire direction. A centered double chevron pattern is shown here. The dashed lines represent the anode wires.

vertices. The position linearity can be optimized with appropriate f_x values of the zigzag pattern.

One disadvantage of the chevron pad readout is that the position resolution across anode wire direction is limited by the anode wire spacing. The arrangement illustrated in Fig. 7.2.2 can effectively half the position resolution across anode wires without adding additional readout electronics. The number of anode wires is doubled in this configuration. An avalanche created near the anode wire between pad rows will induce charge on both rows of pads. Centroid finding can be performed with 4~6 nodes. The major drawback is that the signal to noise ratio is lower, due to the large number of readout nodes used for centroid finding.

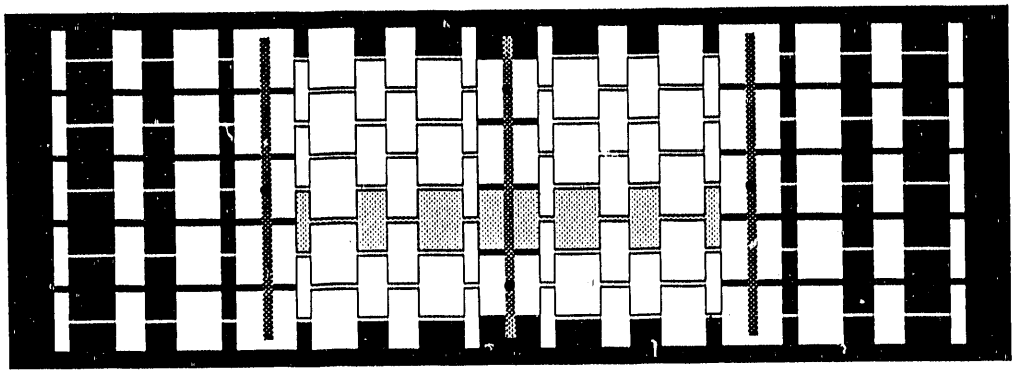

Figure 7.2.3: A cathode pattern using a combination of resistive pads and graded density pads. One of the complete pads is shaded. Resistive strips interconnect columns of pads. Position interpolation along both axes can be realized.

Fig. 7.2.3 illustrates another cathode configuration for position interpolation in both x and y directions. It is a combination of the graded density pads and resistive pads cathode. Charge division along the horizontal direction is performed by geometrical charge division with the graded density pads, while along the vertical direction is done by resistive charge division. Centroid finding is performed with several nodes in a cluster.

7.2.3 Outstanding Problems

One puzzling phenomenon is the disagreement between calculated and measured centroid shift in the one & a half chevron due to the displacement of the positive ions in the y direction (see Fig. 5.3.12). Information of the ion mobility or measured displacement in the centroid of induced charge (see Fig. 5.3.10) indicate that at a 1.4 μs shaping time, the centroid of the cathode induced charge is about 250–300 mum away from the anode wire (in the geometry of the chevron test chamber). However, calculations similar to the one used in the wire displacement study (see Fig. 5.3.14) give results which are less than 1/2 of the experimental measurements. Further investigations are needed to resolve this problem.

Experimental data are needed to confirm or correct the simulated result of the differential non-linearity as a function of f_x and the chevron gap width (see Fig. 5.3.7). Knowledge of their relationship is important in optimizing various chevron geometries.

Finally, a simple and efficient method to calculate the centroids of double hits from 4 to 5 readout nodes is needed for pattern recognition in high multiplicity events. Experimental results are needed to determine the double track resolutions of these interpolating readout systems.

Appendix A. Analog Centroid Finding System

The analog centroid finding system was developed by Radeka et al. [19] at BNL. It has been used throughout the testing of the detectors described in the main text. It has also been used in many detector systems ranging from x-ray imaging to neutron detection.

Its principle of operation is unique in that it applies the centroid finding formula in the time domain, by means of convoluting the input signals with a linear weighting function. It performs the centroid finding using only a few local readout channels which have signal, therefore eliminating the noise contribution from other channels.

Fig. A.1 is a schematic diagram of the centroid finding system [19]. The induced signals on the cathode pads (or strips) are processed by preamplifiers connected to each readout node. Each preamplifier is connected to a Sample & Hold Filter where the signal is shaped at a user selectable shaping time. The shaping time used in most of the measurements is 1.4 μs. The shaped signal is then sampled and sequentially switched to the input of the centroid finding filter. The rate at which each channel is switched is controlled by a clock. The clock frequency used in this work is 4 MHz, or 250 ns per channel. The waveforms of the sequential switch are shown in Fig. 4.2.2. The clock frequency also determines the number of readout nodes being convoluted by the centroid finding filter. The anode signal is processed by a shaping amplifier and synchronized with the clock cycle to generate a timing marker. The centroid finding filter has an impulse response in a shape as shown in Fig. A.1. The output waveform from the filter is also shown in Fig. A.1, which is a convolution of the input waveform and the filter impulse response. The zero crossing time of the filter output is a linear function of the centroid of the avalanche position.

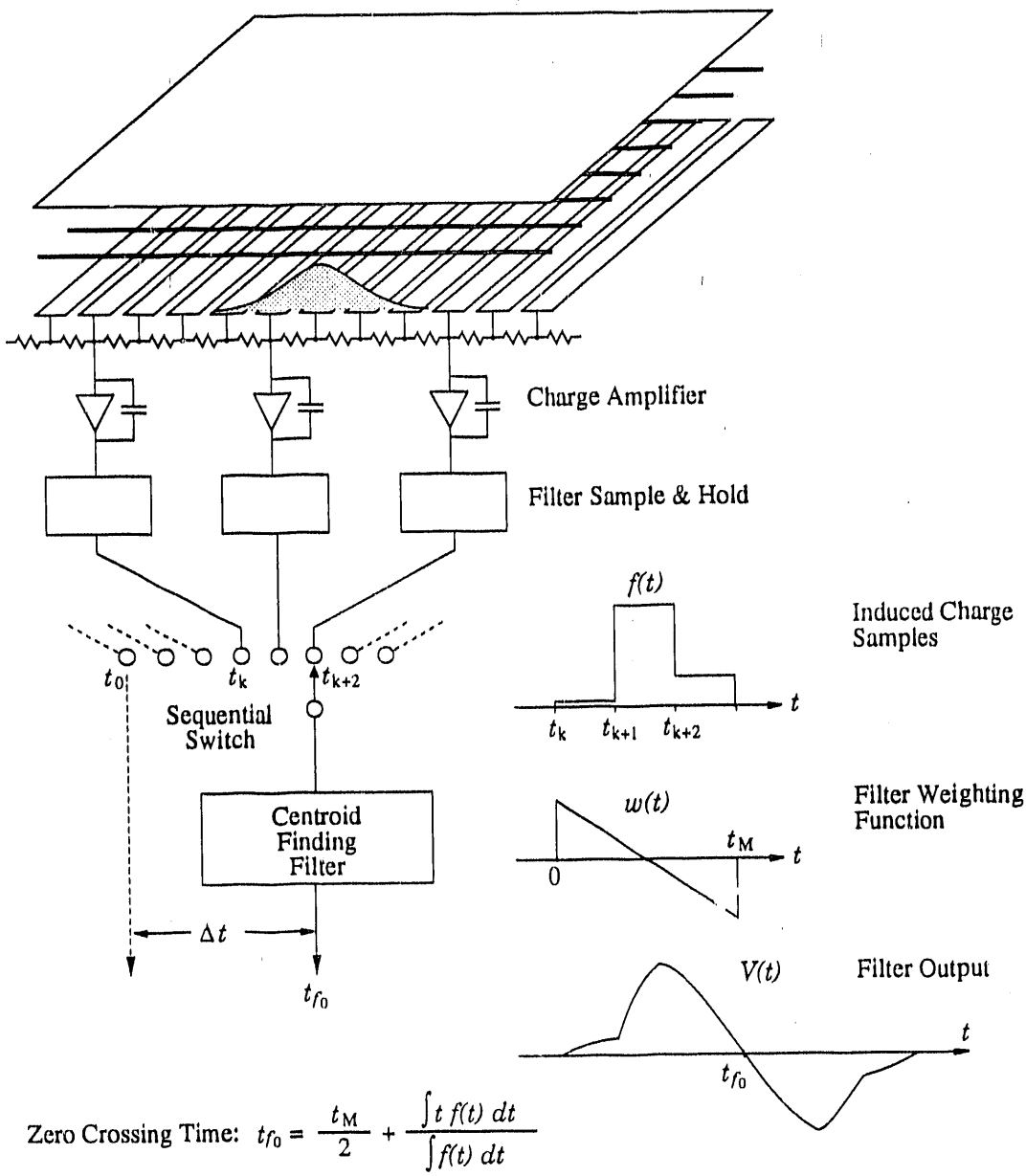

Zero Crossing Time: $t_{f_0} = \frac{t_M}{2} + \frac{\int t\, f(t)\, dt}{\int f(t)\, dt}$

Figure A.1: Analog centroid finding system: Schematic diagram and signal waveforms

Appendix B. Centroid Finding Formula

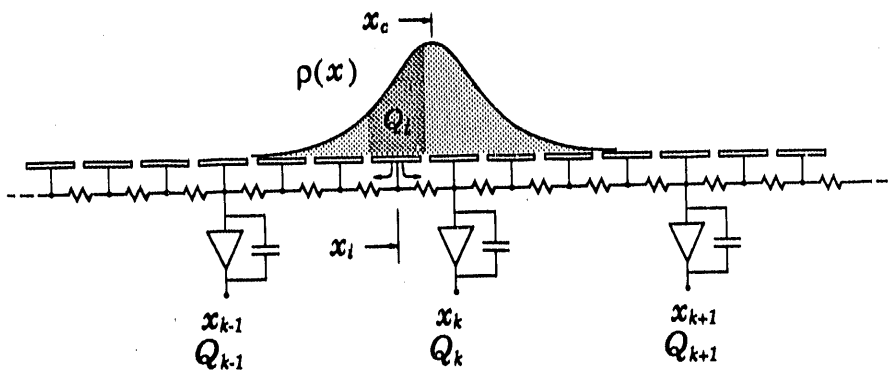

Figure B.1: Resistive charge division in a pad chamber

Fig. B.1 illustrates the principle of charge division on such a cathode. Each pad (at position x_i) under the anode wire is induced an amount of charge (Q_i), which equals the integral of the cathode charge distribution over the area of the pad. These charges are collected by the nearest two preamplifiers at positions x_{k-1} and x_k along the pad row. The amount of charge that goes to either side of the preamplifiers $(Q_{i,k-1}, Q_{i,k})$ is inversely proportional to the resistance values from this pad to the readout pads. So, we have:

$$\frac{Q_{i,k-1}}{Q_{i,k}} = \frac{x_k - x_i}{x_i - x_{k-1}} \qquad \text{for} \quad x_{k-1} \le x_i \le x_k \tag{B.1}$$

$$\frac{Q_{i,k}}{Q_{i,k+1}} = \frac{x_{k+1} - x_i}{x_i - x_k} \qquad \text{for} \quad x_k \le x_i \le x_{k+1} \tag{B.2}$$

where a uniform resistive chain is assumed. Rewriting Eq. (B.1) and Eq. (B.2), one can get:

$$x_i\left(Q_{i,k-1} + Q_{i,k}\right) = x_{k-1}Q_{i,k-1} + x_kQ_{i,k} \qquad \text{for} \quad x_{k-1} \le x_i \le x_k \tag{B.3}$$

$$x_i\left(Q_{i,k} + Q_{i,k+1}\right) = x_kQ_{i,k} + x_{k+1}Q_{i,k+1} \qquad \text{for} \quad x_k \le x_i \le x_{k+1} \tag{B.4}$$

Knowing that

$$Q_{k-1} = \sum_i Q_{i,k-1} \qquad \text{for} \quad x_{k-1} \le x_i \le x_k$$

$$Q_k = \sum_i Q_{i,k} \qquad \text{for} \quad x_{k-1} \le x_i \le x_{k+1}$$

$$Q_{k+1} = \sum_i Q_{i,k+1} \qquad \text{for} \quad x_k \le x_i \le x_{k+1}$$

$$Q_i = Q_{i,k-1} + Q_{i,k} \qquad \text{for} \quad x_{k-1} \le x_i \le x_k$$

$$Q_i = Q_{i,k} + Q_{i,k+1} \qquad \text{for} \quad x_k \le x_i \le x_{k+1}$$

Sum Eq. (B.3) and Eq. (B.4) over all pads between x_{k-1} and x_{k+1}:

$$\sum x_i Q_i = x_{k-1}Q_{k-1} + x_k Q_k + x_{k+1}Q_{k+1}$$

The centroid of the charge distribution is defined as:

$$x_c = \frac{\int_{-\infty}^{\infty} x\rho(x)\,dx}{\int \rho(x)\,dx} \tag{B.5}$$

for discrete pads, it can be approximated as:

$$x_c = \frac{\sum x_i Q_i}{\sum Q_i} \tag{B.6}$$

with an error:

$$\delta x_c = \frac{\sum \int_{x_i-d/2}^{x_i+d/2} (x_i - x)\,\rho(x)\,dx}{\sum Q_i} \tag{B.7}$$

where d is the length of the pads along the wire direction. The error term is determined by the width of the pads d and the distribution of the induced charge. It is independent of the readout spacing l_a. Provided that the charge induced on nodes other then $k-1$, k, $k+1$ is negligible, and the size of the cathode pads is small enough ($d < 0.8h$), the centroid position can be evaluated by:

$$x_c = \frac{x_{k-1}Q_{k-1} + x_k Q_k + x_{k+1}Q_{k+1}}{Q_{k-1} + Q_k + Q_{k+1}} \tag{B.8}$$

Similarly, one can derive that in general

$$x_c = \frac{\sum_k x_k Q_k}{\sum_k Q_k}.$$

Appendix C. Position Resolution as a Function of Position

It was found that the position resolution of the detectors using the centroid finding method displays a periodic variation (see Fig. C.1). In other words, the position resolution depends on the location of the measurement. Detailed discussion on this subject can be found in ref. [25]. A simple model is given here to explain the phenomenon.

Let's start with the general case: signals are collected by three readout nodes at locations x_A, x_B and x_C. Their signal charges are denoted by Q_A, Q_B and Q_C, and they are separated by l_a. Let Q_B be the maximum of the three, and $x_B = 0$ (which implies $-l_a/2 \leq x_c \leq l_a/2$, and $x_A = -l_a$, $x_C = l_a$). Assuming that the noise from all three channels is not correlated. The centroid position is determined as:

$$\begin{aligned} x_c &= \frac{x_A Q_A + x_B Q_B + x_C Q_C}{Q_A + Q_B + Q_C} \\ &= l_a \frac{Q_C - Q_A}{Q_A + Q_B + Q_C} \\ &= l_a \frac{Q_C - Q_A}{Q_T} \end{aligned}$$

where $Q_T = Q_A + Q_B + Q_C$. The position error is then:

$$\begin{aligned} \delta x_c &= \frac{l_a}{Q_T} \left[\delta Q_C - \delta Q_A - x_c \left(\delta Q_A + \delta Q_B + \delta Q_C\right)\right] \\ &= \frac{l_a}{Q_T} \left(\delta Q_C \left(1 - x_c\right) - \delta Q_A \left(1 + x_c\right) - \delta Q_B x_c\right) \end{aligned} \tag{C.1}$$

Assuming $\delta Q_A = \delta Q_B = \delta Q_C = \Delta Q$, then

$$\begin{aligned} \frac{\delta x_c}{l_a} &= \frac{\Delta Q}{Q_T} \sqrt{\left(1 - x_c\right)^2 + {x_c}^2 + \left(1 + x_c\right)^2} \\ &= \frac{\Delta Q}{Q_T} \sqrt{2 + 3{x_c}^2} \end{aligned}$$

It can be seen that the position resolution is determined by the combination of the signal-to-noise ratio and the factor $\sqrt{2 + 3x_c^2}$. The maximum value (~ 1.66) occurs when $x_c = l_a/2$ (midway between two nodes), and the minimum value (~ 1.41) occurs when $x_c = 0$ (over one node).

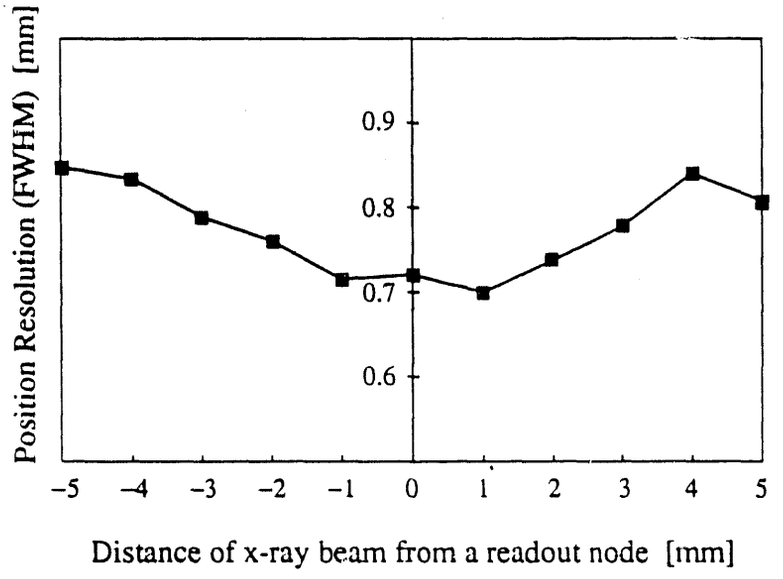

Figure C.1: Experimental measurements of position resolution versus position. The readout spacing is 10 mm.

Using a similar argument, one can find that for the case of centroid finding using two nodes, $\delta x_c/l_a = \frac{\Delta Q}{Q_T}\sqrt{1-2x_c+2x_c^2}$, the minimum value lies midway between the two nodes. For the case of four nodes, $\delta x_c/l_a = \frac{\Delta Q}{Q_T}\sqrt{6-4x_c+4x_c^2}$, and the minimum lies midway between the two inner nodes.

This behavior of the position resolution is intrinsic to the centroid finding formula and it is always true if the noise is uncorrelated and a fixed number of readout nodes are used to perform the centroid calculation.

It should be noted that the variation in position resolution as a function of position is independent of the variation in position sensitivity. In chambers which have locations that display position non-linearity, the local position sensitivity will change. This will give a distorted position resolution measurement. For example, suppose the UIR spectrum of a detector has a spike at certain location. The position sensitivity there will be lower than elsewhere. The position resolution measured from the system will be smaller than the real resolution.

Appendix D. Effect of Inclined Particle Tracks

All the results shown in previous sections are based on particles or photons with normal incidence. However, in a real experiment, particles may have different incident angles. It is important to understand the behavior of the detector system under such conditions.

A. Monochromatic Photons

As described in Chapter 2, a photon deposits its energy in a single transaction. It leaves a point like ionization in the detector gas volume. For a thin detector, where the thickness of the gas volume is smaller than the absorption length of the photon in that gas mixture, the probability of an ionization event in the gas volume is uniformly distributed along the path of the incident photon. Neglecting the variation in deposited energy for each photon, the resolution of the track position is:

$$\sigma = \frac{1}{\sqrt{12}} d \tan\alpha$$

where α is the angle between the z axis and the photon beam projected on the x–z plane.

B. Particle Tracks

It is difficult to describe accurately the position resolution for inclined particle tracks, because of the large variation in energy deposition and distribution. Nevertheless, results of a simplified computer simulation are given here as an estimate.

A number of clusters are generated according to a Poisson distribution. The cluster size is then generated by a distribution given by H. Fischle et al. [54](shown in Fig. D.1b). Each electron within a cluster is drifted (projected) to the anode wire, and multiplied by a gas gain factor with an exponential distribution. The pulse height spectrum is shown in Fig. D.1c. The centroid of all the electrons in a particle track is calculated. The standard deviation of the centroid distribution for a large number of tracks is shown in Fig. D.1a as a function of the incident track angle.

Detectors used in many colliding beam experiments have to operate in magnetic fields. If the magnetic field has a non-zero component in the direction perpendicular to the direction of the anode wire, the electrons created by the ionization of

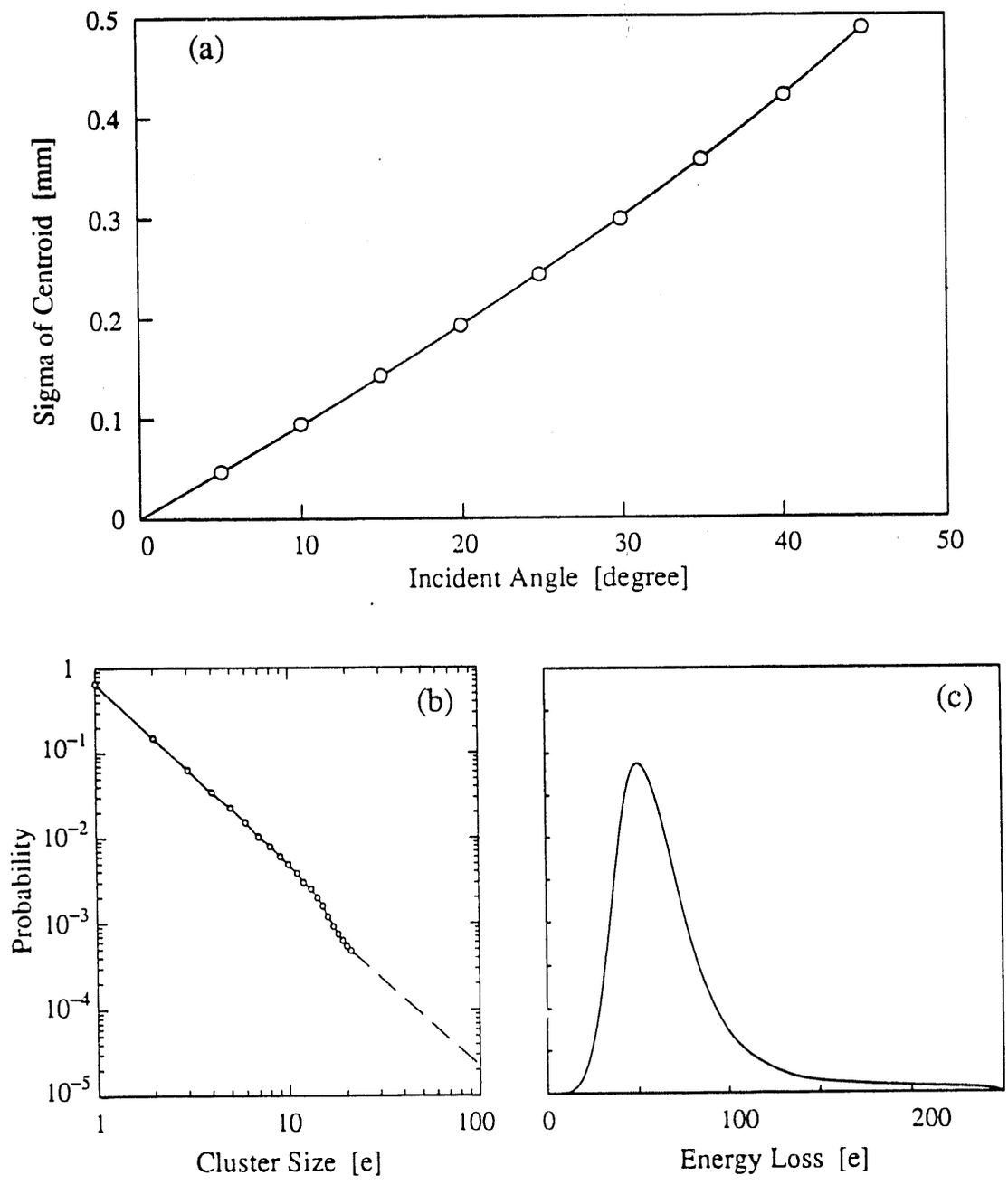

Figure D.1: (a) Computer simulated results of position resolution as a function of track angle. (b) Cluster size distribution used in the simulation. Data was based on Argon gas from [54]. (c) The energy spectrum by convoluting the cluster size distribution and poisson distribution. The depth of the chamber is 5 mm

the particle will drift under the influence of the Lorentz Force. There will be a finite angle (Lorentz Angle) between the drift direction and the electrical field. The net result is to some extent similar to the case of inclined particle tracks. However, a 3-D model is needed to simulate this situation. This effect can be greatly reduced by rotating the chamber at an angle so that the incident particle track is at the Lorentz Angle with respect to the chamber. The electron clusters will then drift towards the anode wire with the Lorentz Angle, that is, along the particle track.

Appendix E. Heavy Ion Detection

The full-size pad chamber has been used in the heavy ion experiment at the AGS. There were several problems discovered during its operation.

A. Sustained high leakage current on the anode wires

The gas used in the detector was originally 50% argon and 50% ethane mixture. It was found that if the anode charge levels exceeded more than 1.5–2 pC, the anode leakage current started to increase dramatically. The current would reach a level around several microamps, and that current would then be maintained even though there was no longer radiation incident on the chamber. A power down was required to eliminate the current. On the anode wire frame, resistors of 10 MΩ were used to limit the current, thereby protecting anode wires from damage in case of a high voltage breakdown. The voltage drop on the anode wire due to the large leakage current could significantly reduce the gas gain.

The problem was solved by flowing gas through alcohol which was maintained at 0°C.

B. Negative pedestal

The complete readout system including ADCs was carefully calibrated before and during the experiment. However, it was found that the average ADC count for heavy ion events was negative. A close look revealed that there was some correlation between the negative background and the positive signal from each event. Fig. E.1 shows these results, where the sum of all positive ADC counts for each event is plotted against the sum of all negative ADC counts.

This correlation is an indication of some sort of crosstalk. It could come from two major sources: one was the readout electronics, the other was the anode wire plane. The electronics system was tested against crosstalk at an early stage of the experiment. It was unlikely that crosstalk of this amplitude could be due to the electronics. It was believed that the large avalanche signal on a few anode wires momentarily changed the bias of the wire frame, and the cathode pads picked up the fluctuation in the anode wire voltage.

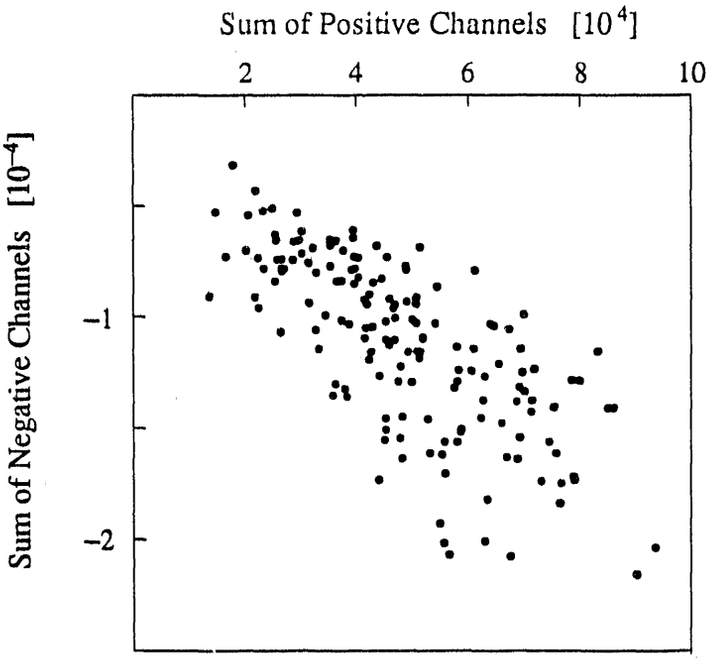

Figure E.1: Sum of all negative channels versus sum of all positive channels

It was also found that a similar problem was more pronounced on some anode wires. This can be see in Fig. E.2, which illustrates an event display from the pad chamber. Pads with positive signal are represented by squares and pads with negative signal are represented by circles. The area of the square or circle is proportional to the amount of charge. Notice that almost all pads under one anode wire had negative signals. It is suspected that there was a poor connection between the anode wire and the isolating capacitor, which provided an AC ground.

C. δ rays inside the chamber

δ rays are known to be associated with heavy ion particles. Their presence is very clear from some of the event displays that captured the trajectory of the δ electrons, see, for example, Fig. E.3. Pattern recognition of minimum ionizing particles was made very difficult by δ rays.

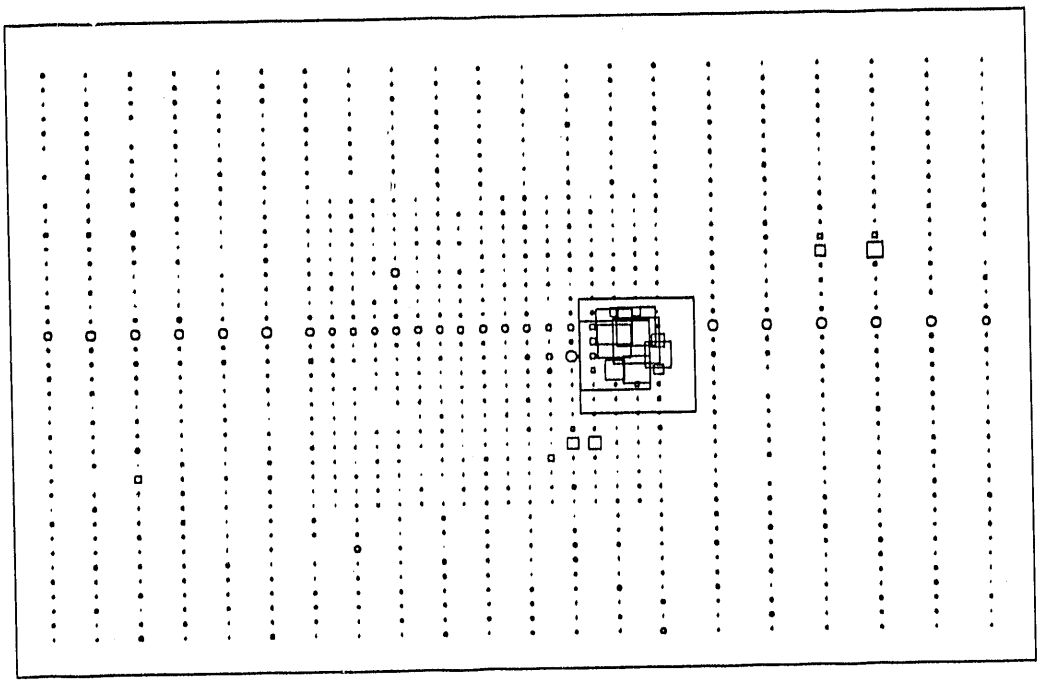

Figure E.2: Event display of the pad chamber showing the negative pedestal under one wire.

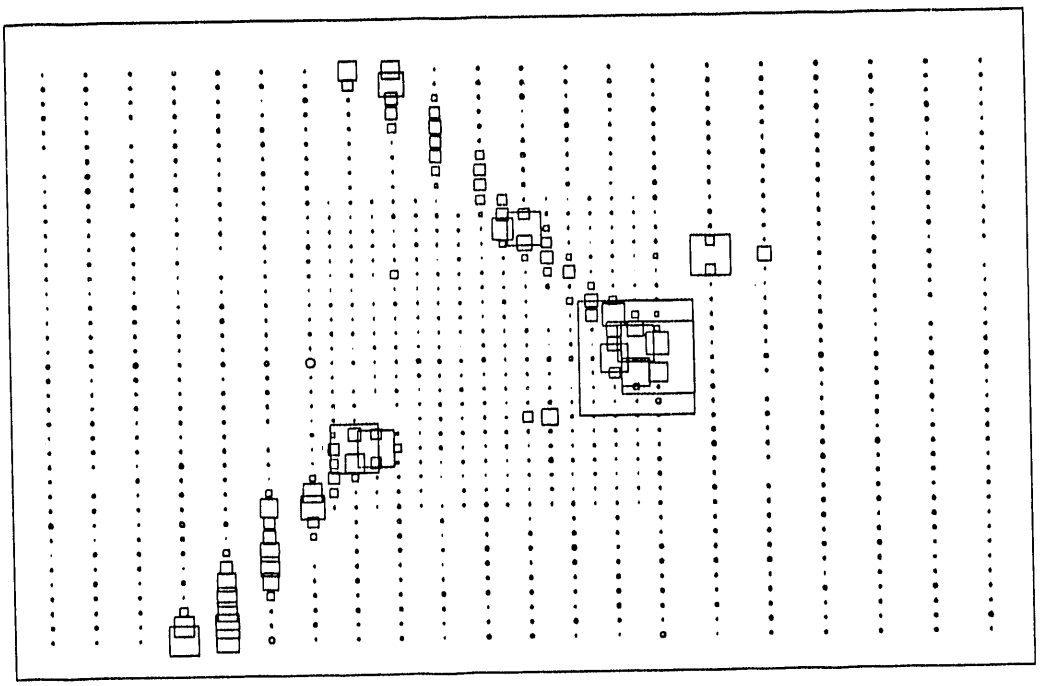

Figure E.3: Two δ electrons originating from the heavy ion beam spot.

Appendix F. Position Resolution and the Dynamic Range of ADCs

In the design of a detector system using ADCs, the most common problem is what dynamic range of the ADC, or the number of bits, is needed to achieve the desired position resolution. Of course the larger the dynamic range, the better the position resolution (provided that the electronic noise is negligible). However, the bandwidth of the data acquisition system, the speed of digitization and, for the case of flash ADCs, the power dissipation and the amount of electronics are just some of the limiting factors restricting the use of high dynamic range ADCs. Optimization of the number of ADC bits, as well as the ADC levels, are needed to achieve the desired position resolution with minimum ADC bits.

It is a well known fact that a MWPC with a 1 bit ADC, which simply gives a "yes" or "no" answer, has a position resolution of $s/\sqrt{12}$, s being the anode wire pitch. It is interesting to note that the position resolution of a detector using a centroid finding scheme and a 1 bit ADC will give a position resolution better than $l_a/\sqrt{12}$ (l_a being the readout spacing). This is due to the fact that more than one readout channel provides the position information. For example, an optimized centroid finding system will use 2 to 3 channels for the centroid calculation. If the signals from one channel exceeds the threshold, the centroid position will be at the node position of that channel. If the signals from two adjacent channels exceed the threshold, the centroid will be in the middle of the two nodes. If the threshold of the discriminator is set at such a level that the probability of an event having two channels that exceed threshold equals the probability of an event having one channel that exceeds threshold, the position resolution can be a factor of two better ($0.5\,l_a/\sqrt{12}$). The factor of two can only be realized if the signal sizes are the same for all events, in other words, the energy spectrum is a δ function. Using more channels for centroid evaluation will not improve the resolution beyond this factor of two.

In applications where position resolution of $0.5\,l_a/\sqrt{12}$ is adequate, the choice of the discriminator threshold can be optimized based on the geometry of the chamber. For example, on a cathode whose readout spacing, l_a, is 3 times the anode-cathode

spacing h, the threshold should be set at around 30% of the total cathode charge level. If $l_a = 5h$, then a level of 25% of the total will give the best position resolution.

Computer simulations were performed to study the dependence of position resolution on the number of ADC bits. Some of the results are shown in Fig. F.1. One set of data is from events with an δ function—just as a reference. One set of data is from events with a gaussian energy spectrum whose σ is 10% of the mean. This is to simulate events for several keV x-rays in a MWPC. One set of data is from events with a Landau type energy spectrum (see Fig. 4.4.2). The ADC levels are assumed to be uniformly spaced.

These simulations also indicated an interesting result that non-linear ADC levels may improve the position resolution slightly. This was studied only with a small number of ADC levels (2 to 4 bits). Fig. F.2 shows three sets of ADC values that give better position resolution than optimized linear settings. To understand this, let's recall the discussion in Appendix 3 on the position resolution as a function of position. We have:

$$\delta x \approx \frac{l_a}{Q_T}\left(\delta Q_C\,(1 - x_c) - \delta Q_A\,(1 + x_c) - \delta Q_B x_c\right) \text{(Eq. (C.1))}$$

It can be seen that the contributions from the three error sources δQ_A, δQ_B and δQ_C have different weights to the position resolution. Fig. F.3 plots their relative weights as a function of the centroid position. Clearly, δQ_A and δQ_C have higher weights than δQ_B. Note that for $-0.5 < x < 0.5$, Q_B is larger than Q_A and Q_C. This means that it is more important to maintain accurate measurements on the smaller signals. Therefore, a set of non-linear ADC levels with "condensed" levels towards the low end will give better position resolution.

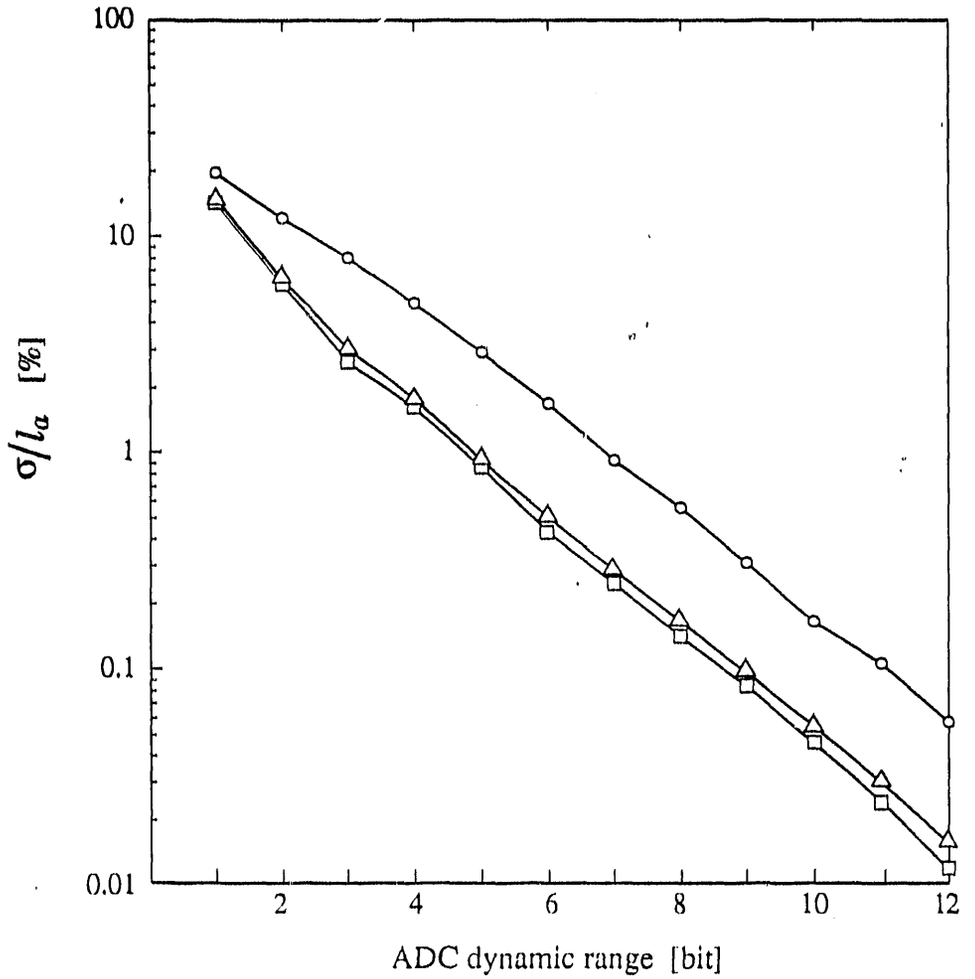

Figure F.1: Relative position resolution as a function of number of ADC bits. All ADC levels are linear. Circles represent results from events with a Landau type energy distribution (see Fig. 4.4.2); Triangles represent results of events with a Gaussian distribution (σ = 10% of mean); Squares represent results of events with a constant signal level. $l_a = 2h$.

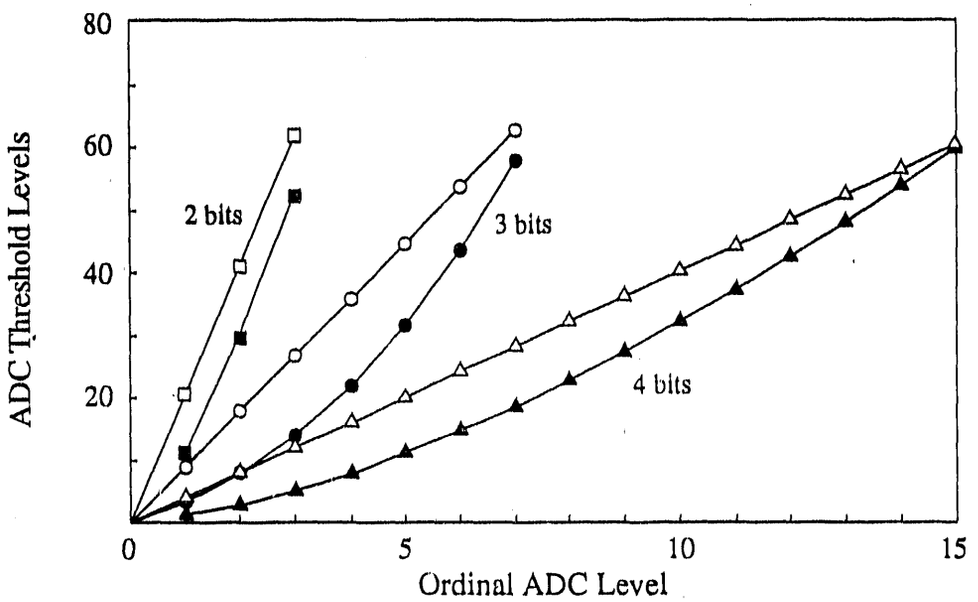

Figure F.2: Examples of non-linear ADC levels (solid symbols) which give better position resolution than the optimized linear levels (hollow symbols) for the case of 2–4 bit ADCs. The improvements on position resolution are 19%, 36% and 15% for 2, 3 and 4 bits, respectively. No variation in avalanche sizes is assumed and the total signal level is set to 100. $l_a = 2h$.

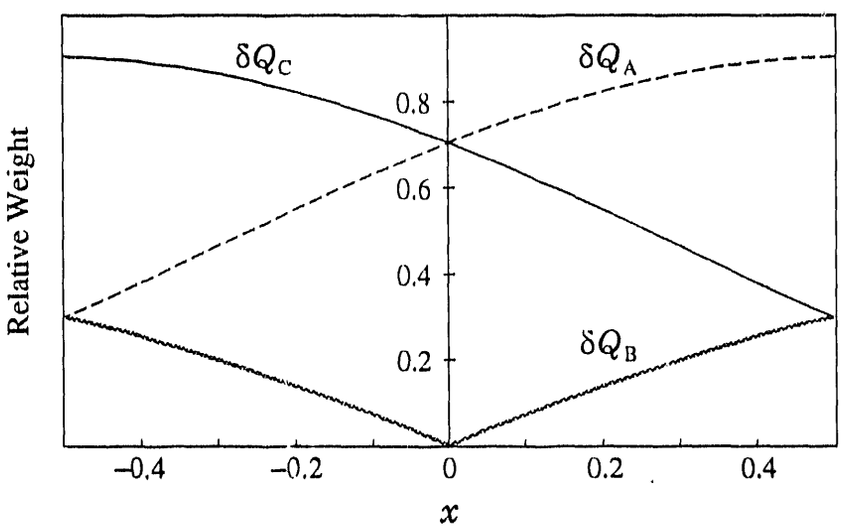

Figure F.3: Relative weights of δQ_A, δQ_B and δQ_C as function ot x. The normalization factor used is $\sqrt{(1+x)^2 + x^2 + (1-x)^2}$.

References

1. S. Miyamoto, "A digitized multi-wire spark chamber for handling many particles," *Nucl. Instr. and Meth.* 30, (1964) 361–362.
2. R. Debbe et al.,"MWPC with highly segmented cathode pad readout," *Nucl. Instr. and Meth.* A283, (1989) 772–777.
3. R. Debbe et al., "Study of wire chambers with highly segmented cathode pad readout for high multiplicity charged particle detector," *IEEE Trans. Nucl. Sci.* NS–37 (1990) 88–94.
4. J. Fischer et al., "A many particle-tracking detector with drift planes and segmented cathode readout," *IEEE Trans. Nucl. Sci.* NS–37 (1990) 82–88.
5. B. Yu, G.C. Smith, V. Radeka and E. Mathieson, "Investigation of chevron cathode pads for position encoding in very high rate, gas proportional chambers," *IEEE Trans. Nucl. Sci.* NS–38 (1991) 454–460.
6. P. Rice-Evans, *Spark, Streamer, Proportional and Drift Chambers*, The Richelieu Press, 1974.
7. O. Blunck and S. Leisegang, *Z. Physik* 128 (1950), 500.
8. W.W.M. Allison and J.H. Cobb, *Ann. Rev. Nucl. Sci.* 30 (1980), 253.
9. R. Veenhof, "Garfield, a drift chamber simulation program," CERN Program Library entry W5050, 1991.
10. E. Mathieson "Induced charge distribution in proportional detectors," to be published.
11. V. Radeka, "Low-noise techniques in detectors," *Ann. Rev. Nucl. Part. Sci.*, 38 (1988), 271–277.
12. H. Okuno, J. Fisher, V. Radeka and H. Walenta, "Azimuthal spread of the avalanche in proportional chambers," *IEEE Trans. Nucl. Sci.* NS–26, (1979) 160–168.
13. E. Gatti, A. Longoni, H. Okuno and P. Semenza, "Optimum geometry for strip cathode or grids in MWPC for avalanche localization along the anode wires," *Nucl. Instr. and Meth.* 163 (1979), 83–92.

14. J.S. Gordon and E. Mathieson, "Cathode Charge Distribution in Multiwire Chambers, I. Measurement and theory," *Nucl. Instr. and Meth.* 227 (1984), 267–276.

15. E. Mathieson and J.S. Gordon, "Cathode Charge Distribution in Multiwire Chambers, II. Approximate and empirical formulae," *Nucl. Instr. and Meth.* 227 (1984), 277–282.

16. J.R. Thompson, J.S. Gordon and E. Mathieson, "Cathode Charge Distribution in Multiwire Chambers, III. Distribution in anode wire direction," *Nucl. Instr. and Meth.* A234 (1985), 505–511.

17. E. Mathieson, "Cathode Charge Distribution in Multiwire Chambers: 4. Empirical formula for small anode-cathode separation," *Nucl. Instr. and Meth.* A270 (1988), 602–603.

18. I. Endo et al., "Systematic shifts of evaluated charge centroid for the Cathode Readout multiwire proportional chamber," *Nucl. Instr. and Meth.* 188 (1981), 51–58.

19. V. Radeka and R.A. Boie, "Centroid finding method for position-sensitive detectors," *Nucl. Instr. and Meth.* 178 (1980), 543–554.

20. G. Charpak, J. Favier and L. Massonnet, "A new method for determining the position of a spark in a spark chamber by measurement of currents," *Nucl. Instr. and Meth.* 24 (1963), 501–502.

21. G.L. Miller, N. Williams, A. Senator, R. Stensgaard and J. Fischer, "A Position Sensitive Detector for a Magnetic Spectrograph," *Nucl. Instr. and Meth.* 91 (1971), 389–396.

22. J. Hough and R.W.P. Drever, "Proportional Counters for the Localisation of Ionizing Radiation," *Nucl. Instr. and Meth.* 103 (1972), 365–372.

23. J. Fischer, J. Fuhrmann, S. Iwata, R. Palmer and V. Radeka, "Large proportional multiwire chambers for transition radiation detection with unambiguous position readout," *Nucl. Instr. and Meth.* 136 (1976), 19–27.

24. C.J. Borkowski and M.K. Kopp, "Design and properties of position-sensitive proportional counters using resistance-capacitance position encoding," *Rev. Sci. Instr.* 46(8) (1975), 951–962.

25. J.L. Alberi and V. Radeka, "Position Sensing by Charge Division," *IEEE Trans. Nucl. Sci.* NS–23 (1976), 251–258.

26. R.A. Boie et al., "Two-dimensional high precision thermal neutron detector," *Nucl. Instr. and Meth.* 200 (1982), 533–545.

27. J. Fischer, V. Radeka and R.A. Boie, "High position resolution and accuracy in ^{3}He two-dimensional thermal neutron detectors," *Proceedings of the Workshop on the Position-Sensitive Detection of Thermal Neutrons*, 1983.

28. J. Fischer, V. Radeka and G.C. Smith, "Position detection of 17-25 keVx-rays in krypton and xenon with a resolution of 18–50 μm (FWHM)," *IEEE Trans. Nucl. Sci.* NS–33 (1986).

29. J. Fischer, V. Radeka and G.C. Smith, "X-ray position detection in the region of 6 *mum* rms with wire proportional chambers," *IEEE Trans. Nucl. Sci.* NS–34 (1987).

30. H.O. Anger, "Survey of radioisotope cameras," *Instr. Soc. Am. Trans.* 5 (1966), 311–334.

31. C. Martin, P. Jelinsky, M. Lampton, R.F. Malina, and H.O. Anger, "Wedge-and-strip anodes for centroid-finding position-sensitive photon and particle detectors," *Rev. Sci. Instr.* 52 (1981), 1067–1074.

32. O.H.W. Siegmund, et al., "Application of the wedge and strip anode to position sensing with microchannel plate and proportional counters," *IEEE Trans. Nucl. Sci.* NS–30 (1983), 503–507.

33. R. Allemand and G. Thomas, "Nouveau detecteur de localisation," *Nucl. Instr. and Meth.* 137 (1976), 141–149.

34. E. Mathieson, G.C. Smith and P.J. Gilvin, "The graded-density cathode," *Nucl. Instr. and Meth.* 174 (1980), 221–225.

35. P.J. Gilvin, E. Mathieson and G.C. Smith, "Subdivision of a graded-density cathode," *Nucl. Instr. and Meth.* 185 (1981), 595–597.

36. P.J. Gilvin, E. Mathieson and G.C. Smith, "Position resolution in a multiwire chamber with graded-density cathodes," *IEEE Trans. Nucl. Sci.* NS–28 (1981), 835–838.

37. J.S. Gordon, E. Mathieson and G.C. Smith, "Improved linearity with tailored CR-GD position-sensitive cathode," *IEEE Trans. Nucl. Sci.* NS–30 (1983), 342–346.

38. D.F. Anderson, H.K. Arvela, A. Breskin and G. Charpak, "A simple 'vernier' method for improving the accuracy of coordinate readout in large wire chambers," *Nucl. Instr. and Meth.* 224 (1984), 315–317.

39. J. Allison et al., "diamond shaped cathode pads for the longitudinal coordinate from a drift chamber," *Nucl. Instr. and Meth.* A236 (1985), 284–288.

40. T. Miki, R. Itoh and T. Kamae, "Zigzag-shaped pads for cathode readout of a time projection chamber," *Nucl. Instr. and Meth.* A236 (1985), 64–68.

41. G.C. Smith, J. Fischer and V. Radeka, "Capacitive charge division in centroid finding cathode readouts in MWPCs," *IEEE Trans. Nucl. Sci.* NS–35 (1988), 409–413.

42. E. Mathieson and G.C. Smith, "Reduction in non-linearity in position-sensitive MWPCs," *IEEE Trans. Nucl. Sci.* NS–36 (1989), 305–310.

43. T. Trippe, "Minimum tension requirements for Charpak chambers' wires," CERN NP Internal Report 69-18, 1969.

44. J. Harder, "Computer-aided design of a high rate position sensitive gas proportional detector system," BNL Internal Memo, (1989).

45. J. Fischer, unpublished results.

46. J. Chiba et al., "Study of position resolution for cathode readout MWPC with measurement of induced charge distribution," *Nucl. Instr. and Meth.* 206 (1983), 451–463.

47. G. Charpak and F. Sauli, "Multiwire proportional chambers and drift chambers," *Nucl. Instr. and Meth.* 162 (1979), 405–428.

48. A.H. Walenta, "Left-right assignment in drift chambers and MWPC's using induced signals," *Nucl. Instr. and Meth.* 151 (1978), 461–472.

49. R. Chase, "Evaluation of the linearity of position measurement with chevron-shaped cathodes by scaled-up simulation," BNL Internal Note (1987).

50. E. Mathieson, G.C. Smith, private communications.

51. C.J. Borkowski and M.K. Kopp, "Electronic discrimination of the effective thickness of proportional counters," *IEEE Trans. Nucl. Sci.* NS–24 (1977), 287–292.

52. G.C. Smith, J. Fischer and V. Radeka, "Photoelectron range limitation to the spatial resolution for x-rays in gas proportional chambers," *IEEE Trans. Nucl. Sci.* NS–31 (1984), 111–114.

53. A.L.S. Angelis et al., "Test results with a novel high-resolution wire chamber with interpolative pad readout," *Nucl. Instr. and Meth.* A283 (1989), 762-766.

54. H. Fischle et al., "Experiential determination of ionization cluster size distributions in counting gases," *Nucl. Instr. and Meth.* A301 (1991), 202–214.

END

DATE FILMED

3/19/92